Article:
Lenton, TM, Daines, SJ and Mills, BJW (2018) COPSE reloaded: an improved model of biogeochemical cycling over Phanerozoic time. Earth-Science Reviews, 178. pp. 1-28. ISSN: 0012-8252

https://doi.org/10.1016/j.earscirev.2017.12.004

COPSE reloaded: An improved model of biogeochemical cycling over Phanerozoic time

Timothy M. Lenton, Stuart J. Daines, Benjamin J.W. Mills

PII: S0012-8252(17)30411-7
DOI: https://doi.org/10.1016/j.earscirev.2017.12.004
Reference: EARTH 2544

To appear in: *Earth-Science Reviews*

Received date: 11 August 2017
Revised date: 8 December 2017
Accepted date: 8 December 2017

Please cite this article as: Timothy M. Lenton, Stuart J. Daines, Benjamin J.W. Mills , COPSE reloaded: An improved model of biogeochemical cycling over Phanerozoic time. The address for the corresponding author was captured as affiliation for all authors. Please check if appropriate. Earth(2017), https://doi.org/10.1016/j.earscirev.2017.12.004

COPSE reloaded: An improved model of biogeochemical cycling over Phanerozoic time

Timothy M. Lenton[a]*, Stuart J. Daines[a], Benjamin J. W. Mills[b]

[a]Earth System Science group, College of Life and Environmental Sciences, University of Exeter, Exeter EX4 4QE, UK

[b]School of Earth and Environment, University of Leeds, Leeds LS2 9TJ, UK

*Corresponding author: Tim Lenton

E-mail address: t.m.lenton@exeter.ac.uk

Full postal address: Earth System Science group, College of Life and Environmental Sciences, University of Exeter, Laver Building (Level 7), North Park Road, Exeter EX4 4QE, UK

Abstract

The 'COPSE' (Carbon, Oxygen, Phosphorus, Sulphur and Evolution) biogeochemical model predicts the coupled histories and controls on atmospheric O_2, CO_2 and ocean composition over Phanerozoic time. The forwards modelling approach utilized in COPSE makes it a useful tool for testing mechanistic hypotheses against geochemical data and it has been extended and altered a number of times since being published in 2004. Here we undertake a wholesale revision of the model, incorporating: (1) elaboration and updating of the external forcing factors; (2) improved representation of existing processes, including plant effects on weathering and ocean anoxia; (3) inclusion of additional processes and tracers, including seafloor weathering, volcanic rock weathering and $^{87}Sr/^{86}Sr$; (4) updating of the present-day baseline fluxes; and (5) a more efficient and robust numerical scheme. A key aim is to explore how sensitive predictions of atmospheric CO_2,

O_2 and ocean composition are to model updates and ongoing uncertainties. The revised model reasonably captures the long-term trends in Phanerozoic geochemical proxies for atmospheric pCO_2, pO_2, ocean [SO_4], carbonate $\delta^{13}C$, sulphate $\delta^{34}S$ and carbonate $^{87}Sr/^{86}Sr$. It predicts a two-phase drawdown of atmospheric CO_2 with the rise of land plants and associated cooling phases in the Late Ordovician and Devonian-early Carboniferous, followed by broad peaks of atmospheric CO_2 and temperature in the Triassic and mid-Cretaceous – although some of the structure in the CO_2 proxy record is missed. The model robustly predicts a mid-Paleozoic oxygenation event due to the earliest land plants, with O_2 rising from ~5% to >17% of the atmosphere and oxygenating the ocean. Thereafter, atmospheric O_2 is effectively regulated with remaining fluctuations being a Carboniferous-Permian O_2 peak ~26% linked to burial of terrestrial organic matter in coal swamps, a Triassic-Jurassic O_2 minimum ~21% linked to low uplift, a Cretaceous O_2 peak ~26% linked to high degassing and weathering fluxes, and a Cenozoic O_2 decline.

Keywords

Phanerozoic; Biogeochemistry; Carbon; Oxygen; Climate; Modelling

1. Introduction

How the composition of the atmosphere and the global biogeochemical cycling of major elements have changed over geologic time is a subject of broad inter-disciplinary interest. In particular atmospheric CO_2 and O_2 are 'master variables' of the Earth system that have been affected by both geological drivers and biological evolution (Lenton and Watson, 2011). Variations in atmospheric CO_2 are in turn a key contributor to long-term climate regulation (Walker et al., 1981), and variations in atmospheric O_2 have been linked to the evolution of aerobic life forms (Sperling et al., 2015a). The Phanerozoic is the best studied Eon with the most data. Yet despite numerous proxies to reconstruct past atmospheric CO_2 levels there are still lingering disagreements among those proxies and important gaps in the record especially before ~420 Ma (Royer, 2014). For past atmospheric O_2

levels there are only indirect constraints during parts of the Phanerozoic (Bergman et al., 2004). The best established constraint on O_2 is a lower limit of 15-17% from combustion experiments combined with the near continuous presence of fossil charcoal over the past ~420 Myr (Belcher and McElwain, 2008; Glasspool et al., 2004; Scott and Glaspool, 2006). A more uncertain upper limit on O_2 of 25-35% has been inferred from the sensitivity of fire frequency to increasing O_2 and the continuous presence of forests over the past ~370 Myr (Glasspool and Scott, 2010; Lenton and Watson, 2000b).

The limitations of the proxy record mean that models, combined with data, have a key role to play in trying to reconstruct past variations in atmospheric CO_2 and O_2. However, model predictions should not be confused with reality. In particular, inferences about the supposed effects of predicted variations in atmospheric O_2 on animal evolution (Berner et al., 2007; Falkowski et al., 2005; Graham et al., 1995; Graham et al., 2016) should be treated with caution, given that there are already several quite different model predictions of Phanerozoic O_2 variations (Mills et al., 2016). Before making such inferential leaps, the focus should be on which (if any) of the features in past O_2 (and CO_2) reconstructions are robust to model and data uncertainty.

The aim of this paper is therefore to try to better understand, mechanistically and quantitatively, the controls on atmospheric CO_2 and O_2 over Phanerozoic time, and to assess how sensitive predictions of these variables are to factors we are scientifically uncertain about. To undertake such an exercise we need to be clear about our scientific method and specifically the role we want a model to play in gaining knowledge (our epistemology). Hence we start by briefly reviewing existing approaches to modelling Phanerozoic biogeochemical cycling.

1.1. Review of existing modelling approaches

All models of biogeochemical cycling over Phanerozoic timescales typically have some representation of sedimentary reservoirs (e.g. of carbon and sulphur in reduced and oxidised forms) coupled to much smaller ocean-atmosphere reservoirs (e.g. of carbon, oxygen and sulphate).

However, there are two very different ways in which the models are used to try and gain knowledge; the inverse (data-driven) and forwards modelling approaches (Fig. 1).

Most previous studies following Garrels and Lerman (1981; 1984), and including the GEOCARB family of models (Berner, 1991, 1994, 2006a; Berner and Kothavala, 2001), have taken the inverse (data-driven) modelling approach (Fig. 1a). Whilst some models are driven by rock abundance data (Berner and Canfield, 1989), most are driven by isotopic data, notably the $\delta^{13}C$ and $\delta^{34}S$ records and a set of associated assumptions about how they are related to key processes (burial of organic carbon and pyrite sulphur, respectively). This leaves the only remaining data to test the model against as the uncertain proxies for CO_2 (Royer, 2014), and the even sparser and more uncertain constraints on O_2. Furthermore it is unclear how strongly reconstructing CO_2 constrains past O_2 variations (or *vice versa*). Such isotope-driven models are sensitive to the chosen $\delta^{13}C$ and $\delta^{34}S$ input data, particularly in their predictions of atmospheric O_2 (Mills et al., 2016), yet these isotope records are imperfectly known with considerable regional variations superimposed on an underlying global signal. Isotope-driven model predictions, particularly of O_2, are also sensitive to assumptions made about the carbon and sulphur isotope mass balances, to the extent that they are unable to produce plausible reconstructions of atmospheric O_2 without assuming sensitivity of C and S isotope fractionation to O_2, which provides stabilising negative feedback (Berner et al., 2000; Lasaga, 1989). Isotope-driven models have also typically had to assume 'rapid recycling' of deposited sediments, whereby sedimentary rock reservoirs are divided into 'young' (rapidly recycled) and 'old' components – with the young sedimentary reservoirs assumed to be comparable in size to the ocean-atmosphere reservoirs of C and S, and the old reservoirs typically assumed to be much larger and constant in size. This introduces another form of negative feedback whereby changes in the burial of reduced or oxidised carbon or sulphur are relatively rapidly counteracted by changes in the size and isotopic composition of the young reservoirs (Berner, 1987).

In designing the original COPSE model a different, forwards modelling approach was taken (Fig. 1b). A key target was to predict $\delta^{13}C$ and $\delta^{34}S$ records for comparison to data – as a means of testing the model's external forcing assumptions and internal mechanistic assumptions (Bergman et al., 2004). This means that COPSE explicitly simulates relevant biogeochemical fluxes such as organic carbon and pyrite sulphur burial (as a function of other variables and forcing parameters) rather than simply driving them with the isotope records. To this end nutrient (P, N) cycling is explicitly represented – a major difference from the GEOCARB family of inverse models – and a range of feedbacks in the coupled C, O, P, S and N cycles are considered. Notably, plausible predictions of atmospheric O_2 variation are achieved by assuming some negative feedback(s) within the surface Earth system between O_2 and its sink and/or source fluxes, and several of these candidate feedbacks are mediated by phosphorus cycling (Lenton and Watson, 2000b). The model does not assume rapid recycling of recently deposited sediments (although this may be a geologically reasonable mechanism). Nor does it assume constant sized ancient sedimentary reservoirs (which are hard to justify over Phanerozoic timescales). Instead, for simplicity, single, variable sedimentary reservoirs are assumed for organic carbon, carbonate carbon, pyrite, and gypsum.

A more elaborate forwards model is MAGic (Arvidson et al., 2006, 2011, 2013, 2014; Guidry et al., 2007), which shares elements in common with both COPSE and GEOCARB and is particularly focused on the inorganic side of the carbon cycle. MAGic tracks atmospheric CO_2 and O_2 and includes a much more detailed approach to ocean composition and the rock cycle than either GEOCARB or COPSE, with a total of 40 state variables. It tracks seven major ions of seawater (using a Pitzer approach to computing activities), plus phosphate as a limiting nutrient, and marine organic matter. It distinguishes a range of crystalline continental rocks (silicates), shelf/continental sediments and sedimentary rocks, sediments buried in deep cratons, seafloor basalt components, pelagic (deep ocean floor) sediments, and clays. MAGic includes feedback on atmospheric CO_2 from silicate weathering and feedback on atmospheric O_2 from redox-dependent phosphorus burial/recycling (Van Cappellen and Ingall, 1996). The model is driven by a range of geological forcing factors taken

from GEOCARB III (Berner and Kothavala, 2001), BLAG (Berner et al., 1983), and rock abundance data (including coal). It is not driven by isotope records, nor are these used as a model prediction target. Instead model predictions are compared to CO_2 proxies and to reconstructions of ocean composition. A key difference from COPSE is that the burial flux of terrestrially-derived organic carbon is assumed to be tiny (Arvidson et al., 2006). Hence there is no predicted secular change in atmospheric oxygen levels with the rise of land plants, although greatly enhanced coal deposition in the Carboniferous-Permian is sufficient to drive a predicted O_2 peak at that time (Arvidson et al., 2013).

Whilst both forwards and inverse modelling approaches have merits, the scope for testing the predictions of inverse modelling against data is limited by design – because much of the available data has gone into the model as drivers. As so many factors concerning the drivers and feedbacks controlling atmospheric CO_2 and O_2 are uncertain, and given that we only have uncertain proxies for CO_2 and a lower bound on O_2 (neither of which extend to the early Paleozoic), we continue to pursue the forwards modelling approach here – because it gives us several more opportunities to test our understanding and hypotheses (as represented by the model) against independent data (proxy records). One of the key aims here is to see to what degree those proxy records constrain the model mechanisms.

Both of the existing modelling approaches have revealed some useful lessons as to how to model the coupled histories of CO_2 and O_2. In particular, there are several good reasons to first understand what controls atmospheric CO_2 and then try to understand what controls O_2. Firstly, ocean-atmosphere carbon has a shorter residence time than oxygen (at least after the early Paleozoic) so CO_2 can be treated as at steady state on a ~1 Myr timescale over which O_2 varies. Secondly, the control exerted by the CO_2 cycle on the O_2 cycle appears to be stronger than *vice versa* (Bergman et al., 2004). Thirdly, our understanding of controls on atmospheric CO_2 is more broadly agreed upon than our understanding of controls on O_2 – notwithstanding some on-running discussion about the

cause(s) of Cenozoic CO_2 change (e.g. Caves et al., 2016; Li and Elderfield, 2013; Mills et al., 2014a; Torres et al., 2014; Willenbring and von Blanckenburg, 2010).

Existing models suggest that long-term atmospheric CO_2 concentration is governed largely by geologic and biologic forcing factors and by the functional dependencies of terrestrial silicate weathering and seafloor weathering on CO_2 and/or temperature, which provide negative feedback. Whilst organic carbon burial is an important sink of CO_2 and provides coupling to the O_2 cycle (where it is the major source of O_2), in current models it only exerts second-order control on CO_2 (Bergman et al., 2004; Berner, 2006a). However, variations in O_2 may significantly affect vegetation and thus silicate weathering and CO_2 (Bergman et al., 2004).

Understanding what controls atmospheric O_2 (and at what resulting levels) remains an outstanding puzzle, with a wider range of feedbacks proposed than for CO_2 (Kump, 1988; Lenton and Watson, 2000b; Van Cappellen and Ingall, 1996), together with biologic and geologic forcing. The coupling from the CO_2 cycle to the O_2 cycle may be of first-order importance, with silicate and carbonate weathering potentially providing a large fraction of the phosphorus supply that can ultimately determine organic carbon burial, which is the dominant source of oxygen (Bergman et al., 2004; Lenton et al., 2014). However, selective weathering of phosphorus by plants could act to decouple silicate weathering and organic carbon burial (Lenton et al., 2012, 2016). Changes in the C/P ratio of buried organic matter, especially a large increase in this ratio with the rise of land plants, also exert first-order control on O_2 (Bergman et al., 2004; Berner, 1989; Kump, 1988; Lenton et al., 2016). Furthermore, it has been argued that erosion rates exert a first-order control on organic carbon burial (Berner, 2006a; Blair and Aller, 2012; Hedges and Keil, 1995), providing a further coupling between the CO_2 and O_2 cycles insofar as physical weathering rates control chemical weathering rates and thereby increases in erosion may decrease CO_2 and increase O_2.

1.2. Motivation and aims

In keeping with the original COPSE study (Bergman et al., 2004), our aim here is to produce a quantitative model that incarnates various mechanistic hypotheses and makes resulting predictions which can be tested against multiple, independent proxy data constraints.

We have several reasons to update the COPSE model. Firstly, some of the model assumptions have been critiqued, suggesting alternative hypotheses to test, including the aforementioned argument that organic carbon burial is controlled more by erosion fluxes than by phosphorus supply (Berner, 2006a). Secondly, although the original COPSE model sought to make the model forcing independent of isotope inversion, the forcing of uplift was ultimately derived from inversion of the strontium isotope record – an inconsistency which we have subsequently addressed for the Mesozoic and Cenozoic by making $^{87}Sr/^{86}Sr$ a predicted variable (Mills et al., 2014a). This modification gives an additional target to test the model against, especially given previously published difficulties in fitting the complete Phanerozoic strontium isotope record (Francois and Walker, 1992). Thirdly, the field of Phanerozoic modelling has advanced. Notably Bob Berner published a combined model of Phanerozoic atmospheric O_2 and CO_2, GEOCARBSULF (Berner, 2006a), which he subsequently updated to distinguish weathering of volcanic rocks (Berner, 2006b), and revised carbon isotope forcing data and fractionation (Berner, 2009). The importance of volcanic rock weathering in CO_2 consumption has been more widely recognised with the emplacement of large igneous provinces (LIPs) linked to both short-term release and long-term drawdown of CO_2 (Schaller et al., 2011), and phosphorus supply from volcanic rock weathering linked to organic carbon burial (Horton, 2015). Partly in response to this we began to extend COPSE to include LIP emplacement and volcanic rock weathering for the Mesozoic-Cenozoic (Mills et al., 2014a). New work on the biogeochemical effects of early plants also motivated other updates to the Paleozoic predictions of COPSE (Lenton et al., 2012, 2016). Finally, in the wider geochemical literature there have also been significant revisions to

estimates of key fluxes in the coupled C, O, P and S cycles, for example silicate weathering (Hartmann et al., 2009; Moon et al., 2014).

In the following we undertake a thorough review, reconsideration and revision (where warranted), of all aspects of the COPSE model, including bringing together developments of the model since the original paper (Lenton, 2013; Lenton et al., 2012, 2016; Mills et al., 2014a). Our central aim is to illustrate for the reader the effects of the many uncertain aspects of the coupled C, O, P, and S cycles on long-term predictions of atmospheric CO_2, O_2, and ocean composition. In keeping with the philosophy behind the model, we use it as a framework to test mechanistic hypotheses, by making quantitative predictions of $\delta^{13}C$, $\delta^{34}S$, $^{87}Sr/^{86}Sr$, alongside CO_2 and O_2, which are tested against available data. This evaluation of input assumptions and different mechanistic hypotheses ultimately leads to an assessment of which predicted features of Phanerozoic variation in atmospheric CO_2, O_2 and ocean composition are robust to current uncertainties, and which critical uncertainties remain that could be targeted by future work. The remainder of the paper is structured as follows: Section 2 describes a comprehensive series of updates to the COPSE model. Section 3 tests their effects by comparing the resulting predictions against multiple proxy records, and arrives at a new baseline model. Section 4 concludes.

2. Model description

A schematic of the revised COPSE model structure is shown in Figure 2. Panel A shows the mass fluxes in the linked C-S-O cycles, which feature in both COPSE and GEOCARBSULF. Panel B shows the feedback-based biosphere component, which is unique to COPSE and is used to calculate the burial fluxes of organic carbon and pyrite sulphur in a forwards manner from other model processes (as opposed to inferring these fluxes through isotope mass balance as in e.g. GEOCARBSULF). All terms in Figure 2 are defined in Tables 1 and 2.

Our revision of the model spans changes to its internal structure, changes to its parameters, and changes to the forcing factors driving it. We start by introducing the model reservoirs, i.e. state variables, and the most fundamental structural changes, i.e. addition of new fluxes. Next we describe changes to the model forcing factors. Then we work through the model processes and corresponding equations, including some further structural changes at the level of changing functional dependencies. Finally we consider changes to the baseline fluxes of the model.

2.1. Reservoirs and new fluxes

The revised COPSE model retains at its core the coupled C, O, P and S cycles, and an oceanic cycle of N. Sr is added as an illustrative tracer cycle (which does not affect the overall dynamics) (Mills et al., 2014a). The oceanic N and P cycles are tightly coupled such that versions of the model that remove the N cycle and relate new production directly to P concentration give comparable results (Lenton et al., 2012), but we retain both cycles here.

In previous updates to the model, some new fluxes have been introduced (Mills et al., 2014a), notably seafloor weathering is included as a sink of CO_2, and terrestrial silicate weathering is subdivided into contributions from volcanic rocks (termed 'basalt') and from all other non-volcanic igneous silicate rocks (termed 'granite'). Here we also add pyrite and gypsum degassing fluxes of sulphur in line with GEOCARBSULF (Berner, 2006a). The original COPSE had a partial, interactive Ca cycle, but as gypsum degassing is a source of volatile S but not of Ca, whereas gypsum burial removes both Ca and S from the ocean, this poses a mass balance problem for Ca. Hence we opt to remove the partial, interactive Ca cycle from COPSE. Only the gypsum burial flux was related to modelled calcium, and we now relate this to a prescribed reconstructed change in ocean [Ca] (Horita et al., 2002). Modelling by others has given a more complete treatment of Ca variation over Phanerozoic time (Arvidson et al., 2013).

The core model includes surface reservoirs of atmosphere-ocean oxygen (***O***) and carbon (***A***), and oceanic nitrogen (***N***), phosphorus (***P***), and sulphur (***S***), with sedimentary rock reservoirs of organic

(reduced) carbon (***G***), carbonate (oxidised) carbon (***C***), pyrite (reduced) sulphur (***PYR***), and gypsum (oxidised) sulphur (***GYP***). These are shown as circles in Figure 2. In our notation, upper case bold italic lettering (e.g. ***A***) indicates reservoir size in moles and lower case bold italic lettering (e.g. ***a***) indicates reservoir size normalised to the present. Differential equations and present-day reservoir sizes are summarised in Table 1. The meaning of different flux terms and their original baseline values are introduced in Table 2. The additional tracer cycle of strontium includes ocean (***OSr***) and sedimentary carbonate (***CSr***) reservoirs. It is introduced briefly below and described in full in Appendix A.

2.2. Forcing factors

The original COPSE model was forced by changing solar insolation (*I*), metamorphic and volcanic degassing (*D*), tectonic uplift (*U*), plant evolution and land colonisation (*E*), plant enhancement of weathering (*W*), apportioning of carbonate burial between shallow and deep seas (*B*), and changing C:P burial ratio of terrestrial plant material (CP_{land}) (Table 3). Changing solar insolation is based on established stellar physics and is implicit in the time-dependent calculation of global temperature hence is not discussed further here. Subsequent work using COPSE has suggested several updates to the original geological and biological forcing factors (Fig. 3), and has introduced volcanic, non-volcanic and carbonate rock area, paleogeography effects on runoff (Mills et al., 2014a) and selective biotic weathering of P (Lenton et al., 2012, 2016) as additional forcing factors. Here we first describe further updates to the original set of forcing factors (Fig. 3) and then describe an expanded and updated list of additional forcing factors (Fig. 4). In developing the model we also explored yet further forcing factors (Table 3) which are not included here (in the interests of simplicity), because they had little effect or generated easily falsified results.

2.2.1. Degassing (*D*)

The controls on metamorphic and volcanic degassing (*D*) – here of sedimentary volatiles – are a subject of ongoing debate. On the longest timescales degassing is expected to be driven by the

Earth's decaying internal heat source, but with the supercontinent cycle and associated changes in plate tectonics causing substantial fluctuations about the long-term trend – including recent suggestions that more CO_2 degassing occurs at continental arcs than oceanic arcs (Lee et al., 2013; McKenzie et al., 2016). The original degassing forcing of COPSE followed GEOCARB II (Berner, 1994) in linking subduction rates to seafloor spreading rates estimated based on direct estimates of subduction for the last 180 Myr (Engebretson et al., 1992) and sea-level change prior to that (Gaffin, 1987). Recent work has linked degassing for the past 230 Myr to inferred subduction zone length from seismic tomographic imaging of subducted slabs (Van Der Meer et al., 2014), and this forcing has been tried in COPSE (Mills et al., 2014a). Other recent work has sought to quantitatively reconstruct plate tectonics through parts of Phanerozoic time, including changes in subduction zone length (Matthews et al., 2016). However, a complete Phanerozoic reconstruction is currently unavailable. Hence here instead we derive degassing using the original sea-level inversion approach (Gaffin, 1987) applied to a more recent Phanerozoic sea-level dataset (Haq, 2014; Haq and Al-Qahtani, 2005; Haq and Schutter, 2008). The original method (Gaffin, 1987) is simplified, with little effect on the results (Mills et al., 2017). The main change from updating the sea-level data is an increase in inferred degassing from the late Permian to the mid Cretaceous (Fig. 3a).

2.2.2. Uplift (U)

Uplift forcing (U) is updated (Mills et al., 2014a), following GEOCARBSULF (Berner, 2006b; Royer et al., 2014), such that it is based on a polynomial fit to sediment accumulation rates over Phanerozoic time (Ronov, 1993) rather than inversion of the strontium isotope record. This produces a smoother forcing that follows the same long-term trend as the original forcing (Fig. 3b). It captures the overall modulation of uplift by the supercontinent cycle, but does not resolve specific orogenic events. In recent versions of GEOCARBSULF (Royer et al., 2014), variation in the uplift/erosion forcing is scaled down by a 2/3 power, but here we use the original smooth fit to the Ronov data, reasoning that this represents the supply of new rock available for chemical weathering. For application of the model to specific events within the Phanerozoic, and for capturing some of the fine-scale structure in the

strontium isotope record, the uplift forcing could be modulated to capture specific orogenic events, but we do not pursue this here.

2.2.3. Plant evolution (*E*)

We retain separate forcing factors for plant evolution (*E*) and plant effects on weathering (*W*) for consistency with earlier work, although they follow similar trajectories and are multiplied together where they appear in the model weathering equations. For plant evolution (*E*; Fig. 3c), we update the rise of the earliest non-vascular plants to capture their higher potential productivity and spatial coverage (Porada et al., 2016) with *E* increasing from 0 to 0.15 over 465 to 445 Ma (Lenton et al., 2016). We also revise the subsequent rise of rooted vascular plants, including forests, with *E* increasing more rapidly from *E*=0.15 at 400 Ma to *E*=1 at 350 Ma, in contrast to a slower rise to *E*=1 at 300 Ma in the original COPSE model, and a later starting rise from 380 Ma to 350 Ma in GEOCARBSULF.

2.2.4. Plant effects on weathering (*W*)

We update the effect of the earliest non-vascular plants on weathering (*W*; Fig. 3d) to capture stronger effects suggested by recent experimental results and ecophysiological modelling studies (Lenton et al., 2012; Porada et al., 2016) with *W* increasing from 0 to 0.75 over 465 to 445 Ma (Lenton et al., 2016). Here we also increase weathering amplification *W* from 0.75 to 1 over 400-350 Ma associated with the evolution of rooted vascular plants, including deep rooted trees. We correspondingly remove the original increase in weathering amplification with the Cretaceous rise of angiosperms (*W* from 0.75 to 1 over 115-100 Ma), which was taken from GEOCARB I and II (Berner, 1991; Berner, 1994), noting that GEOCARB III also explores no effect of angiosperms and opts for *W*=0.875 prior to angiosperms (Berner and Kothavala, 2001). Whilst there is some evidence that angiosperms can increase weathering rates relative to gymnosperms (Moulton et al., 2000), there is other evidence that they can suppress weathering rates (Andrews et al., 2008). Hence the assumption of no increase in weathering rates seems a reasonable baseline. In contrast to our

chosen forcing, GEOCARBSULF assumes that plants only start to affect weathering at 380 Ma with the rise of trees and that a major increase to *W*=0.875 is complete by 350 Ma, with a further increase to *W*=1 associated with the rise of angiosperms over 130 to 80 Ma (Royer et al., 2014).

2.2.5. Plant stoichiometry (CP_{land})

We update the forcing of land plant stoichiometry (CP_{land}; Fig. 3e) to capture a high C/P of earliest non-vascular plants and associated peats. The original model assumed a default C/P = 1000 burial ratio of terrestrially-derived organic matter but increased this to C/P = 2000 over 355-345 Ma then decreased it back to C/P = 1000 over 290-280 Ma in a crude attempt to capture the effect of abundant deposition of coals from swamps in the Carboniferous (and early Permian). Subsequent work noted that non-vascular plant matter has a high C/P ~2000 (Lenton et al., 2016) and that peatland transformation to coaly shales had started by the early Devonian (Kennedy et al., 2013). Hence C/P was increased to 2000 with the rise of the first non-vascular plants, over 465-445 Ma (retaining the decrease to C/P = 1000 over 290-280 Ma). Here we first adopt that forcing, then when we introduce an additional forcing factor of coal basin depositional area (b_{coal}) we change the timing of the decline of C/P to 345-300 Ma, to avoid excessive Carboniferous organic carbon burial as b_{coal} ramps up over this interval.

2.2.6. Pelagic calcification (B)

We update the shape of the shift in the location of carbonate burial from shelves to the deep sea with the rise of pelagic calcifiers (*B*; Fig. 3f), which increases carbonate degassing. The approach originally used in COPSE is from GEOCARB I and involves a sharp rise which then saturates. This can be questioned given that the extra carbonate getting subducted should be an integral of what has previously been deposited on slowly moving ocean plates, hence should not increase abruptly even if the deposition flux increases abruptly. In GEOCARB II, Berner (1994) used a linear rise from 150-0 Ma and experimented with different initial values of 0.5 to 1 as well as the standard 0.75, showing

that this has a substantial effect on CO_2 predictions. Here we adopt the GEOCARBSULF choice of a linear rise from 0.75 to 1 over 150-0 Ma (Royer et al., 2014).

2.2.7. Volcanic silicate rock area (a_{bas})

In recent work (Mills et al., 2014a) we introduced a distinction between volcanic silicate rocks (termed 'basalt') and non-volcanic silicate rocks (termed 'granite'), and a new normalised model forcing representing the exposed area of volcanic rocks (a_{bas}). This forcing captures the combined area of large igneous provinces and volcanic islands (ocean island basalts and island arcs). Here we extend this approach back in time using initial LIP areas from an updated version of the Large Igneous Provinces Commission compilation starting at 720 Ma (Ernst, 2014). The cumulative LIP area forcing was calculated assuming exponential decay with time of each individual LIP from their initial estimated area to their present area. Decay rates for each major LIP were set to retrieve their present day area, and an overall decay rate for other LIPs set to retrieve a cumulative present day area of 4.8×10^6 km^2 (Mills et al., 2014a). We assume volcanic island area scales with subduction-related degassing (D) as the majority of volcanic islands are linked to island arcs driven by crust subduction (Allegre et al., 2010). The resulting forcing shows a ~2.5 fold increase in volcanic rock area over Phanerozoic time (Fig. 4a).

We also estimated an additional contribution to degassing from the emplacement of large igneous provinces (D_{LIP}), but as this is only a small fraction of total degassing, the principal effects of which are on short-term events (Mills et al., 2014a), we do not include it here.

2.2.8. Non-volcanic silicate rock area (a_{gran})

In previous work (Mills et al., 2014a), a normalised forcing of the area of non-volcanic silicate rocks (a_{gran}) was introduced, taken to be the remainder of total continental area (from GEOCARBSULF) minus exposed carbonate area (from GEOCARBSULF) minus volcanic rock area (a_{bas}). Here instead we estimate a kinetically-weighted area forcing of the non-volcanic component of silicate weathering (a_{gran}) based on the Phanerozoic paleogeology reconstructions of Bluth and Kump

(1991). We took the midpoint of geologic intervals from the latest geological timescale (Cohen et al., 2013; updated) and interpolated linearly between them. a_{gran} is assumed to comprise cation contributions from shield rocks (a_{sil}) and from secondary minerals in sedimentary rocks (a_{sed}), which make a large contribution to today's non-volcanic silicate weathering flux (Amiotte-Suchet et al., 2003; Hartmann et al., 2009). 'Shales' have been estimated to contribute ~77% of the non-volcanic silicate weathering CO_2 consumption flux (Amiotte-Suchet et al., 2003), although a more sophisticated treatment of current lithology suggests that all non-carbonate sedimentary rocks contribute ~62% of the non-volcanic silicate weathering flux (or ~52% of total silicate weathering) (Hartmann et al., 2009). Hence we define $a_{gran} = k_{sed} \cdot a_{sed} + (1- k_{sed}) \cdot a_{sil}$, as a kinetic and area weighted forcing factor, and opt for $k_{sed} = 0.6$ as a reasonable estimate. The sedimentary rock types assumed to contribute significantly to silicate weathering are shales, coals, and evaporites. (Sandstone and siliceous chert are neglected because they do not contribute greatly to silicate weathering and COPSE does not keep track of their sedimentary reservoirs.) We sum together the areas of these three rock types to create a normalised forcing (a_{sed}), making one adjustment from the original dataset of Bluth and Kump (1991) in that we neglect an inferred sharp increase in exposed shale area from the Pliocene to the present (taking the Pliocene value as the present value). Exposed shield silicate area (a_{sil}) from Bluth and Kump (1991) shows a large decline over Phanerozoic time and replacement largely by sandstones, which (as they discuss) may be partly an artefact. In a_{gran} it is somewhat counteracted by an increase in the area of shales, coals and evaporites, although a_{gran} still declines by a factor ~2.5 over Phanerozoic time (Fig. 4b).

We also calculated normalised forcing factors for exposed areas of carbonate (a_{carb}), shale (a_{shale}), organics (shale + coal) (a_{org}), and evaporites (a_{evap}), and experimented with using them to force the weathering fluxes of carbonate (a_{carb}), pyrite (a_{shale}), organic carbon (a_{org}), and gypsum (a_{evap}), but leave them out here as they either failed to improve the results or clearly degraded them.

2.2.9. Paleogeography (*PG*)

Following GEOCARBSULF and Mills et al. (2014a), we consider an additional weathering forcing representing the combined effects of changes in paleogeography (*PG*) on global river runoff and on the fraction of land area undergoing chemical weathering (thus excluding dry regions) (Fig. 4c). For this we use GCM-based estimates that exclude the effects of changing CO_2 and solar luminosity (Royer et al., 2014), multiplying together their f_D forcing and a normalised-to-present version of their f_{Aw}/f_A forcing. We do not further scale the resulting forcing by total land area, as is done in GEOCARBSULF (Royer et al., 2014), because exposed areas of relevant rock types are dealt with separately.

2.2.10. Coal deposition (b_{coal})

Coal deposition on land has at times been a significant contributor to global organic carbon burial, controlled by a combination of the occurrence of subsiding low-relief cratons and a moist climate (Nelsen et al., 2016). Following other Phanerozoic modelling studies, e.g. Bartdorff et al. (2008), here we add a coal basin depositional area forcing (b_{coal}, labelled '*b*' for burial to distinguish it from '*a*' for exposed area forcing), which is ultimately derived from data for coal abundance (Ronov, 1993) (and hence comparable to what Bluth and Kump, 1991, find for coal depositional area as that too is based on Ronov's data). b_{coal} is normalised to 1 at present and has a peak of ~12 at the end of the Carboniferous (~300 Ma), but it falls to 0 prior to the Carboniferous, which is at odds with recent discoveries of early Devonian coaly shales (Kennedy et al., 2013) and with the observation that the earliest plants were tied to wetland settings by their physiology, so would be expected to have created peatlands. Hence we set b_{coal} = 1 initially until it starts to increase above that at ~345 Ma. The resulting fluctuations in coal depositional area (Fig. 4d) are only assumed to operate on the small fraction (~0.2; see below) of today's terrestrial organic carbon burial flux that is actually buried in coal basins rather than marine sediments, whereas changes in the C/P ratio of terrestrial organic matter will operate on the whole burial flux, whether burial occurs in terrestrial or marine settings. Hence when introducing b_{coal} we combine it with CP_{land} (rather than replacing it).

2.2.11. Selective biotic weathering of phosphorous (*F*)

An additional forcing factor (*F*) has previously been introduced that represents the selective biotic weathering of P relative to host rock dissolution (Lenton et al., 2012, 2016). This captures the observations that plants and their fungal mycorrhizal symbionts have evolved mechanisms to selectively 'mine' P-rich mineral inclusions in rocks, and experiments show large relative enhancements of P weathering relative to bulk cations (Ca, Mg) by non-vascular plants (Lenton et al., 2012; Quirk et al., 2015). Such selective P weathering represents a mechanism to decouple the inorganic (silicate weathering) and organic (carbon burial) sides of the carbon cycle. It may have been particularly pertinent when early plants were colonising fresh rock surfaces before the establishment of rooting systems, deeper soils and effective P recycling systems. Hence it has been used as a means of forcing mid-Paleozoic increases of organic carbon burial in COPSE (Lenton et al., 2012, 2016). Here we explore an increase from *F*=1 to *F*=1.5 over 465-445 Ma followed by a decrease from *F*=1.5 to *F*=1 over 410-400 Ma (Lenton et al., 2016) (Fig. 4e).

2.2.12. Calcium concentration (c_{cal})

In place of the original interactive marine Ca reservoir we explore forcing gypsum burial with a prescribed variation in normalised marine [Ca^{2+}] (c_{cal}, where 'c' is for concentration) following the fit to the data in Figure 8 of Horita et al. (2002) (Fig. 4f). We also considered forcing gypsum burial with a changing evaporite depositional area (b_{evap}) derived from Bluth and Kump (1991), but this yielded readily falsifiable results so we do not include it here.

2.3. Variables

Changes to the model functions that are incorporated in the new baseline model are summarised in Table 4, and further alternative functions explored in the hypothesis testing are described in this section. Changes to the model non-flux parameters are summarised in Table 5 (changes to flux parameters are in Table 2). In the following we use a prime to indicate a normalised variable.

2.3.1. Atmospheric CO_2

Whereas the original model had a constant atmospheric fraction of the total ocean-atmosphere CO_2 reservoir, here atmospheric CO_2 (in PAL, i.e. normalised) is made proportional to the square of the total amount of carbon in the ocean and atmosphere (normalised variable $\boldsymbol{a}$) following Kump and Arthur (1999):

$$CO_2 = \boldsymbol{a}^2 \tag{1}$$

This makes minimal difference to steady state CO_2 predictions, but variations in the total ocean-atmosphere carbon reservoir ($\boldsymbol{A}$) are much reduced, allowing greater transient variations in CO_2 in studies of short-term events, including e.g. the early rise of plants. Present atmospheric CO_2 (1 PAL) is taken to correspond to a pre-industrial pCO_2 = 280 ppm, i.e. $pCO_2 = 280 \cdot CO_2$ (ppm).

2.3.2. Global temperature

In the interests of simplicity, model comparability, and ability to explore variations in climate sensitivity, we switch from the original global surface temperature (T) function of Caldeira and Kasting (1992) to the GEOCARB III temperature function (Berner and Kothavala, 2001) (which has a slightly different implicit variation in solar luminosity with time):

$$\Delta T = k_c \cdot \ln CO_2 - k_l \cdot t/570 \tag{2}$$

Where k_c = 4.328°C corresponds to a climate sensitivity of 3°C for a doubling of CO_2 and k_l = 7.4°C represents the sensitivity to changing solar luminosity, for time, t, in Myr ago. Present global temperature is taken to be 15°C hence $T = 15 + \Delta T$ (°C).

2.3.3. Net primary productivity

The dependence of global vegetation net primary productivity, V_{npp}, on temperature, T (°C), pCO_2 (ppm) and O_2 (PAL) retains the original 'OCT' formulation:

$$V_{npp} = k_{npp} \cdot E \cdot (1.5 - 0.5 \cdot \boldsymbol{o}) \cdot \left(1 - \left(\frac{T-25}{25}\right)^2\right) \cdot \left(\frac{pCO_2 - P_{min}}{P_{1/2} + pCO_2 - P_{min}}\right) \tag{3}$$

Where P_{min} = 10 ppm, $P_{1/2}$ = 183.6 ppm, and k_{npp} = 2 is a normalising constant for present T = 15°C and pCO_2 = 280 ppm. This represents a slightly weaker CO_2 fertilisation effect than the GEOCARB choices of k_{CO2}=2, P_{min} = 0 ppm, $P_{1/2}$ = 280 ppm (but this has little effect on the results).

2.3.4. Fire effects on vegetation

We adjust the fire function following Lenton (2013) to be based on a fit to experimental results for fuel of 10% moisture content (rather than 20% moisture content in the original model):

$$ignit = min(max(48 \cdot mO_2 - 9.08, 0), 5) \quad (4)$$

where mO_2 (0.21 at present) is the volumetric mixing ratio of O_2 (mol/mol) assuming a constant remainder of the atmosphere dominated by N_2:

$$mO_2 = \frac{\boldsymbol{o}}{\boldsymbol{o}+k_{16}} \quad (5)$$

with k_{16} = 3.762 (as before). The resulting equation for vegetation biomass is as before:

$$V = V_{npp} \cdot \frac{k_{fire}}{k_{fire} - 1 + ignit} \quad (6)$$

but we adopt k_{fire} = 3 following Bond et al. (2005) and Lenton (2013), which equates to a 50% suppression of vegetation biomass by fires at present (relative to the case with no fires; mO_2 <0.19). Together this results in a fire feedback that lies intermediate in strength between the original weak (default) and strong formulations for increases in O_2, and provides stronger feedback against decreases in O_2 as fires have a limiting effect on vegetation down to mO_2 ~0.19, consistent with combustion experiments and spatial modelling of fire propagation (Belcher et al., 2010).

2.3.5. Degassing of carbon and sulphur

Carbonate degassing (*ccdeg*) and organic carbon degassing (*ocdeg*) retain their original functional forms (but the default fluxes are adjusted; see below):

$$ccdeg = k_{12} \cdot D \cdot B \cdot \boldsymbol{c} \quad (7)$$

$$ocdeg = k_{13} \cdot D \cdot \boldsymbol{g} \quad (8)$$

The revised model allows for the possibility of degassing fluxes of gypsum and pyrite:

$$gypdeg = k_{gypdeg} \cdot D \cdot \boldsymbol{gyp} \quad (9)$$

$$pyrdeg = k_{pyrdeg} \cdot D \cdot \boldsymbol{pyr} \quad (10)$$

Initially the sulphur degassing fluxes (k_{gypdeg}, k_{pyrdeg}) are set to zero consistent with the original model.

2.3.6. Seafloor weathering

The revised model includes a seafloor weathering sink of CO_2 which is assumed to scale with degassing (i.e. the rate of oceanic crust production). However, rather than have it depend on CO_2 (Mills et al., 2014a), a direct kinetic temperature dependence is applied:

$$sfw = k_{sfw} \cdot D \cdot e^{k_T^{sfw} \cdot \Delta T} \quad (11)$$

This assumes deep ocean temperature changes in proportion to global average temperature on long timescales. k_T^{sfw} = 0.0608 corresponds to an activation energy (42 kJ mol^{-1}) appropriate for terrestrial basalt weathering, which we take as a default. However recent work suggest a much higher apparent activation energy for seafloor weathering 92±7 kJ mol^{-1} (k_T^{sfw} = 0.1332) implying stronger negative feedback (Coogan and Dosso, 2015), which we explore as an option below. (Seafloor basalt oxidation is also a sink of O_2 ~1x10^{12} molO_2 yr^{-1} (Sleep, 2005) but this term in the oxygen balance is neglected here because it is assumed to scale with *D* in a similar way to organic carbon degassing.)

2.3.7. Plant effects on terrestrial weathering

The effects of plants on weathering are simplified from the original model, which multiplicatively applied the effect of plants on weathering term *V*·*W* leading to a mixing of abiotic and biotic responses. This could erroneously exceed (by up to ~56%) either end-member for intermediate values of *V*·*W* between 0 (abiotic) and 1 (biotic), making the effects of intermediate plant cover excessively strong. The original function also multiplied a Michaelis-Menten function of CO_2 for plant

productivity within *V* by another Michaelis-Menten function of CO_2 (f_{plant}) from GEOCARB, which was also originally intended to capture the CO_2 fertilisation effect on plant productivity. Here we include just one Michaelis-Menten CO_2 dependence within the variable *V*, which also encapsulates the plant evolution forcing factor *E*. Our simplified effect of biota (or lack of it) on weathering is:

$$f_{biota} = \left[(1 - \min(V \cdot W, 1)) \cdot k_{15} \cdot {CO_2}^{0.5} + V \cdot W\right] \quad (12)$$

Where the first term dependent on ${CO_2}^{0.5}$ represents abiotic weathering (following GEOCARB) and the second term represents biotic weathering, which is assumed to scale directly with vegetation biomass (*V*). We retain the original model assumption of k_{15} = 0.15 (i.e. a roughly 7-fold acceleration of weathering by plants) as a baseline. As options later we explore the use of k_{15} = 0.25 (4-fold amplification of weathering by plants) as in GEOCARB III, and k_{15} = 0.1 (10-fold amplification). We also consider the possibility that weathering is controlled by vegetation NPP rather than biomass (using V_{npp} in place of *V* in the above), which removes any effect of fires on weathering.

2.3.8. Temperature effects on weathering

The effects of temperature on weathering rates (directly and via runoff) are separate from the effect of plants. The general form for the direct kinetic effect of temperature on weathering is:

$$f_T^i = e^{k_T^i \Delta T} \quad (13)$$

The original model used an activation energy of 62 kJ mol^{-1} for silicate weathering (k_T = 0.09). Here following Mills et al. (2014a) we use activation energies of 50 kJ mol^{-1} for 'granite' (k_T^{gran} = 0.0724) and 42 kJ mol^{-1} for 'basalt' (k_T^{bas} = 0.0608).

We retain the original dependencies of silicate (*f*) and carbonate (*g*) weathering on runoff:

$$f_{runoff} = [1 + 0.038\Delta T]^{0.65} \quad (14)$$

$$g_{runoff} = 1 + 0.087\Delta T \quad (15)$$

2.3.9. Silicate weathering

The total silicate weathering flux at present (k_{silw}) is divided into a volcanic rock ('basalt') fraction ($k_{basfrac}$) and a non-volcanic rock ('granite') fraction (1-$k_{basfrac}$):

$$k_{granw} = \left(1 - k_{basfrac}\right) \cdot k_{silw}, \qquad k_{basw} = k_{basfrac} \cdot k_{silw} \tag{16}$$

The equations for 'granite' (non-volcanic) weathering (*granw*) and 'basalt' (volcanic) weathering (*basw*) include additional forcing factors capturing changes in exposed areas (a_{gran}, a_{bas}) and paleogeographic effects on runoff (*PG*). In the original model all silicate weathering depended on tectonic uplift, but here whilst weathering of ancient granitic cratons is assumed to depend on uplift by default, the more rapid weathering of relative young volcanic rocks is assumed independent of uplift following Mills et al. (2014a):

$$granw = k_{granw} \cdot U \cdot PG \cdot a_{gran} \cdot f_{Tgran} \cdot f_{runoff} \cdot f_{biota} \tag{17}$$

$$basw = k_{basw} \cdot PG \cdot a_{bas} \cdot f_{Tbas} \cdot f_{runoff} \cdot f_{biota} \tag{18}$$

$$silw = granw + basw \tag{19}$$

Of course mantle plumes themselves may generate some uplift and volcanic islands are often steep and rapidly eroding terrains, but these effects are distinct from uplift of continental crust driven by plate collisions and are assumed to be enfolded in $k_{basfrac}$, which captures the disproportionate contribution of the relatively small area of volcanic rocks to the total silicate weathering flux. As an option we consider introducing an uplift dependence of basalt weathering, to help recover the original model structure. Supply limitation of silicate weathering is not considered here for the Phanerozoic, although it may have been an important factor in the aftermath of Neoproterozoic glaciations (Mills et al., 2011).

2.3.10. Carbonate weathering

Carbonate weathering now includes additional dependencies on crustal carbonate reservoir size and paleogeographic forcing (*PG*):

$$carbw = k_{14} \cdot \boldsymbol{C} \cdot U \cdot PG \cdot g_{runoff} \cdot f_{biota} \quad (20)$$

The dependence on the crustal carbonate reservoir size has minimal effect on the results, because it varies very little, but we include it for consistency with the other weathering fluxes.

2.3.11. Gypsum weathering

Gypsum weathering was originally assumed proportional to carbonate weathering and to the normalised size of the gypsum sedimentary reservoir (***gyp***). Here we make the functional dependencies explicit:

$$gypw = k_{22} \cdot \boldsymbol{gyp} \cdot U \cdot PG \cdot g_{runoff} \cdot f_{biota} \quad (21)$$

2.3.12. Oxidative weathering (kerogen)

Despite critique (Berner, 2006a), the revised baseline model retains the assumption that oxidative weathering of organic carbon (kerogen) has some sensitivity to variations in atmospheric O_2 at the present high O_2 concentrations. This is defended based on abundant evidence for incomplete oxidation of ancient organic carbon in rapidly uplifting/eroding terrains (Galy et al., 2015). Furthermore, the results of more detailed modelling of oxidative weathering across the observed range of erosion rates (Daines et al., 2017) show a dependence on O_2 that is reasonably approximated by the original square root dependence used in COPSE:

$$oxidw = k_{17} \cdot U \cdot \boldsymbol{g} \cdot \boldsymbol{o}^{0.5} \quad (22)$$

Later we test the effects of removing the O_2 dependence following Berner (2006a).

2.3.13. Pyrite weathering

Pyrite oxidation has much faster kinetics than kerogen oxidation hence it goes to completion at present high O_2 concentrations. Indeed detrital pyrite preservation essentially stopped after the Great Oxidation Event at ~2.4 Ga (Johnson et al., 2014). Hence we agree with the critique of (Berner, 2006a) and remove any dependence on O_2 in the revised model:

$$pyrw = k_{21} \cdot U \cdot \boldsymbol{pyr} \tag{23}$$

2.3.14. Phosphorus weathering

The revised model allows the apportioning of the phosphorus weathering flux between different rock types (k_{Psilw}, k_{Pcarbw}, k_{Poxidw}) to be varied and introduces an additional forcing factor (*F*) representing selective P weathering by plants:

$$phosw = k_{10} \cdot F \cdot (k_{Psilw} \cdot silw/k_{silw} + k_{Pcarbw} \cdot carbw/k_{14} + k_{Poxidw} \cdot oxidw/k_{17}) \tag{24}$$

The phosphorus weathering flux from silicates is therefore subdivided into contributions from 'granite' (non-volcanic) and 'basalt' (volcanic) rocks, following equations (17)-(19). We considered making apatite dissolution activation energy distinct from the host rock, but found it did not greatly alter the results. We also considered whether the P content relative to bulk cations (Ca + Mg, associated with the alkalinity flux) should differ between volcanic and non-volcanic silicate rocks, but decided against this as this ratio is highly variable within these rock categories, and because no such adjustment is broadly consistent with a detailed breakdown of phosphorus weathering (Hartmann et al., 2014).

2.3.15. Phosphorus distribution and terrestrial organic matter burial

The fraction of the weathered phosphorus flux that is ultimately buried with land plant derived organic matter (either on land or in the ocean) retains its original linear dependence on terrestrial vegetation biomass (*V*). The burial flux of terrestrially-derived organic phosphorus and associated carbon is taken to encompass both burial on land in peatlands (resulting in e.g. coal deposits) and

burial after erosion and transport in aquatic settings, including freshwaters, estuaries, coastal deltas, and marine sediments (Burdige, 2005; Regnier et al., 2013). Here we distinguish these two burial pathways and explore as options: (i) forcing the fraction of terrestrially-derived organic matter that is buried in peatlands by the changing area of coal basin depositional settings (b_{coal}); (ii) a dependence of aquatic burial of terrestrially-derived material on uplift (U), to capture the observation that increased erosion transfers more terrestrially-derived organic matter to the ocean, where in general it is more efficiently preserved than on land (Blair and Aller, 2012). These alternations are captured by altering the burial flux of P with land plant matter (*pland*) in order to maintain conservation of phosphorus:

$$pland = k_{11} \cdot V \cdot phosw \cdot \left(k_{aq} \cdot f_P(U) + \left(1 - k_{aq}\right) \cdot b_{coal}\right) \quad (25)$$

We set $f_P(U) = 1$ but allow b_{coal} to vary as the default (Table 4). Here k_{aq} is the fraction of terrestrial organic matter burial occurring in aquatic settings today, which we estimate at $k_{aq} = 0.8$ (and is potentially higher than this) (Burdige, 2005), consistent with only a small component of burial due to coals at present. The original function for *pland* is recovered by setting $k_{aq} = 1$ and $f_P(U) = 1$.

The corresponding burial of terrestrially-derived organic carbon also depends on its C/P burial ratio, which is a normalised forcing factor (CP_{land}) as in the original model:

$$locb = \left(\frac{C}{P}\right)_{land} \cdot pland = k_5 \cdot CP_{land} \cdot pland' \quad (26)$$

The transfer of the remaining available reactive phosphorus to the ocean where it can fuel marine productivity is simply given by:

$$psea = phosw - pland \quad (27)$$

2.3.16. Marine new production

New production is controlled by the proximate limiting nutrient as before:

$$newp = r_{C:P} \cdot min\left(30.9 \cdot \frac{\boldsymbol{n}}{r_{N:P}}, 2.2 \cdot \boldsymbol{p}\right) = newp0 \cdot newp' \quad (28)$$

Where the values 30.9 and 2.2 are the present average concentrations of nitrate and phosphate in the ocean (in μmol kg^{-1}), $r_{C:P}$=117 and $r_{N:P}$=16 are the Redfield ratios, and therefore N is proximately limiting at present giving $newp_0$ = 225.96 as a normalising constant.

2.3.17. Anoxia

COPSE followed earlier work (Lenton and Watson, 2000a; Van Cappellen and Ingall, 1994; Van Cappellen and Ingall, 1996) in assigning an anoxic fraction of the ocean (*anox*) that depended on the ratio of oxygen supply and demand, with a present value of 0.14 (broadly intended to represent the fractional surface area of ocean below which there is anoxia at some depth). Anoxic fraction decreased linearly with oxygen from 1 at O_2 = 0 to 0 at O_2 = 1.16 PAL (for present nutrients), and increased in a saturating way with new production (for present O_2) from 0 at *newp'* = 0.86 toward 1. On reflection this is a poor quantitative representation of ocean anoxia, and given growing interest in past intervals of ocean anoxia and their relationship to O_2 and nutrient levels, we redefine the anoxia function here. First we note that only 0.2-0.3% of the seafloor is overlain by anoxic bottom waters (Helly and Levin, 2004). Given the importance of anoxic bottom waters for P cycling (and also several redox sensitive trace metals) we redefine *anox* as the anoxic fraction of the seafloor, and assume that this scales with the volume of anoxic waters.

Oxygen levels in deeper waters separated from the ocean surface by e.g. thermal stratification are controlled by the balance of oxygen supply – via transport of surface waters equilibrated with the atmosphere – and oxygen demand – governed by upwelling transport of deep ocean limiting nutrient concentration and its uptake efficiency, creating a sinking flux of organic matter. COPSE does not consider changes in ocean transport hence the oxygenation state of the deeper ocean depends on the balance of atmospheric oxygen and deep ocean nutrient concentrations. However, some adjustment is required for the incomplete utilisation of nutrients in the high-latitude upwelling regions which play a key role in governing the deep ocean oxygenation state today. Based on the

results of multi-box models (Canfield, 1998), 1-D box-diffusion models (Ozaki and Tajika, 2013; Ozaki et al., 2011), and 3-D ocean models (Lenton and Daines, 2017; Monteiro et al., 2012) we define the control variable for deep ocean anoxia as:

$$k_u \cdot newp' - \boldsymbol{o} \tag{29}$$

Where $k_u < 1$ captures the (in)efficiency of nutrient uptake in the (high-latitude) surface waters ventilating the deep ocean, and also (implicitly) the Redfield ratio of remineralisation -O_2:C~170:117. In today's ocean k_u~0.5, given the values discussed by Canfield (1998), implying a considerable global excess of oxygen supply over demand, and further implying that a halving of atmospheric O_2 or a doubling of ocean nutrients would put the deep ocean on the edge of anoxia. This agrees reasonably with 3D model results where a ratio of normalised O_2:limiting nutrient ~0.4 (rather than 0.5) makes half of the ocean volume anoxic (Lenton and Daines, 2017), or under Cretaceous boundary conditions an approximate doubling of limiting nutrient tips anoxia (Monteiro et al., 2012). Similarly 1-D box-diffusion model results suggest a halving of O_2 tips anoxia (Ozaki and Tajika, 2013) (their figure 5 with fixed nutrient). Clearly some waters are anoxic today and some will remain oxygenated even when the deep ocean is tipped anoxic. To account for such spatial redox heterogeneity we use a logistic functional form:

$$anox = \frac{1}{1+e^{-k_{anox}(k_u \cdot newp' - \boldsymbol{o})}} \tag{30}$$

where k_{anox} controls the sharpness of the transition between oxia and anoxia and (together with k_u) sets the extent of anoxia at present. For k_u = 0.5, k_{anox} = 12 gives *anox* = 0.0025 today, consistent with 0.2-0.3% of the seafloor being overlain by anoxic bottom waters (Helly and Levin, 2004) and giving a fairly sharp transition of *anox* from 0.23 to 0.77 as $\boldsymbol{o}$ (normalised O_2) drops from 0.6 to 0.4 PAL (for fixed nutrient), consistent with other models (Lenton and Daines, 2017; Ozaki and Tajika, 2013). The oxic fraction of the ocean k_1 = 0.997527 is redefined accordingly.

2.3.18. Nitrogen cycling

The redefining of anoxia and the oxic fraction of the ocean means there is huge potential for water-column denitrification to increase as anoxia increases. To prevent denitrification completely draining the ocean of nitrate we introduce a default dependence on nitrate concentration (which was anyway used as an optional 'crash preventer' in the original code at low $\boldsymbol{n} \leq 0.1$):

$$denit = k_4 \left(1 + \frac{anox}{1-k_1}\right) \cdot \boldsymbol{n} \tag{31}$$

Here half of the initial denitrification is assumed to occur under anoxic conditions at depth in sediments and therefore be insensitive to water column and sediment surface redox state.

The function for nitrogen fixation (with $r_{N:P}$=16) is unaltered:

$$nfix = k_3 \left(\frac{\boldsymbol{P}-\boldsymbol{N}/r_{N:P}}{P_0-N_0/r_{N:P}}\right)^2 \text{ for } \frac{\boldsymbol{N}}{r_{N:P}} < \boldsymbol{P}, \text{ else } 0 \tag{32}$$

where P_0 and N_0 are the present day reservoir sizes (Table 1).

Marine organic nitrogen burial is a small term dependent on marine organic carbon burial and a fixed C:N burial ratio = 37.5:

$$monb = mocb/CN_{sea} \tag{33}$$

2.3.19. Marine organic carbon burial

To address a previous critique (Berner, 2006a) we include the option to have erosional (uplift) control of marine organic carbon burial, and we also include an optional dependence on O_2:

$$mocb = k_2 \cdot f(U) \cdot (newp')^2 \cdot f(O_2) \tag{34}$$

We set $f(U)$=1, $f(O_2)$=1 as the default (as in the original model). For the optional oxygen dependence we follow Betts and Holland (1991) as explored by Lenton and Watson (2000b):

$$f(O_2) = 2.1276 \cdot e^{-0.755 \cdot \boldsymbol{o}} \tag{35}$$

although we recognise that seafloor [O_2] can be decoupled from the atmosphere.

2.3.20. Phosphorus burial

Organic phosphorus burial is calculated from marine organic carbon burial and the $(C/P)_{organic}$ burial ratio (CP_{sea}):

$$mopb = mocb/CP_{sea} \tag{36}$$

We retain a fixed burial ratio (CP_{sea} = 250) as the default (as in the original model). However, we also explore the option to make this burial ratio dependent on anoxia, following Van Cappellen and Ingall (1994, 1996):

$$CP_{sea} = \frac{k_{oxic} \cdot k_{anoxic}}{(1-anox) \cdot k_{anoxic} + anox \cdot k_{oxic}} \tag{37}$$

Given the update to the *anox* function we adopt k_{oxic} = 250 and k_{anoxic} = 4000, as originally suggested (Van Cappellen and Ingall, 1994; Van Cappellen and Ingall, 1996), although subsequent work has used as an upper limit k_{anoxic} ~1000 (Slomp and Van Cappellen, 2007).

Iron-sorbed phosphorus (Fe-P) burial retains an inverse dependence on anoxia by default. The redefining of anoxia means there is little scope for Fe-P burial to increase above the present level. We introduce a dependence on phosphate concentration (which was also used as an optional 'crash preventer' in the original code at low $\boldsymbol{p} \leq 0.1$):

$$fepb = \frac{k_6}{k_1} \cdot (1 - anox) \cdot \boldsymbol{p} \tag{38}$$

Predominantly authigenic calcium-bound phosphorus (Ca-P) burial retains a dependence on the supply of organic carbon to the sediments and we also include an optional dependence on anoxia:

$$capb = k_7 \cdot newp'^2 \cdot f(anox) \tag{39}$$

We set *f*(*anox*)=1 as the default (Table 4). For the option to have seafloor anoxia suppress the retention of Ca-P in sediments we follow (Slomp and Van Cappellen, 2007):

$$f(anox) = 0.5 + 0.5\frac{(1-anox)}{k_1} \quad (40)$$

2.3.21. Pyrite burial

Pyrite burial is taken to depend on sulphate concentration and inversely on oxygen concentration. Its dependence on marine organic carbon burial means that it includes an optional dependence on erosion (uplift) as suggested by (Berner, 2006a):

$$mpsb = k_{mpsb} \cdot \frac{\boldsymbol{s}}{\boldsymbol{o}} \cdot mocb' \quad (41)$$

We considered an anoxia rather than O_2 dependence, which would amount to considering anoxic water-column precipitation and preservation of pyrite, but we reason that sedimentary formation of pyrite has been the dominant mechanism over the Phanerozoic.

2.3.22. Gypsum burial

Gypsum burial was originally dependent on ocean sulphate concentration and variable calcium concentration. The calcium variable is replaced here with a forcing factor (c_{cal}):

$$mgsb = k_{mgsb} \cdot \boldsymbol{s} \cdot c_{cal} \quad (42)$$

2.3.23. Carbonate burial

Oceanic carbonate is assumed to be in steady state with marine carbonate carbon burial balancing carbonate input from silicate and carbonate weathering (as in the original model):

$$mccb = silw + carbw \quad (43)$$

We also experimented with a more complex formulation where marine carbonate burial is assumed to maintain an alkalinity balance of the ocean that is affected by the sulphur cycle (Mills et al., 2014a; Torres et al., 2014), with pyrite burial a source of alkalinity, and pyrite weathering, pyrite degassing and gypsum degassing all sinks of alkalinity (sources of sulphuric acid). To maintain a present day steady state this requires upward adjustment of the silicate weathering flux constant

(k_{silw}) such that it balances total volcanic acid input, i.e. both sulphur and carbon degassing. With that adjustment, the effect on the results is small, so for simplicity we leave it out.

2.3.24. Carbon and sulphur isotope systems

COPSE tracks the isotopic composition of all the carbon and sulphur reservoirs. The functional dependencies of carbon and sulphur isotope fractionation are kept the same as in the original model (Bergman et al., 2004). This includes temperature-dependent atmosphere-ocean fractionation of carbon, temperature-dependent fractionation of marine carbonate deposition (assuming calcite throughout), marine organic carbon fractionation (relative to carbonate) dependent on CO_2 and O_2, land organic carbon fractionation (relative to atmosphere) dependent on O_2, and a fixed sulphur fractionation of pyrite burial relative to gypsum burial – as an O_2-dependence was previously found to considerably degrade the $\delta^{34}S$ predictions (Bergman et al., 2004).

2.3.25. Strontium tracer cycle

A strontium cycle and its isotopes are implemented following Francois and Walker (1992) and Vollstaedt et al. (2014) with some improvements to the formulation described in Mills et al. (2014a). A full description is given in Appendix A. Ocean and sedimentary (carbonate) reservoirs of strontium are considered. Ocean Sr sources are the weathering of old igneous rocks (granites), new igneous rocks (basalts), sedimentary carbonates, and mantle input. Ocean Sr sinks are the incorporation of strontium in (carbonate) sediments and seafloor weathering. The sedimentary Sr pool has input from carbonate burial, and outputs from carbonate weathering and metamorphism. The $^{87}Sr/^{86}Sr$ values of mantle input and continental silicates have prescribed present day values (mantle 0.703, 'basalts' 0.705, 'granites' 0.715) but are assumed to have increased over time due to Rb decay. The $^{87}Sr/^{86}Sr$ of sedimentary carbonates varies depending on inputs/outputs and is initialised at 0.708 (a reasonable value for the Late Neoproterozoic). The overall approach is not expected to precisely reproduce the ocean $^{87}Sr/^{86}Sr$ record, because of heterogeneity in the ages of rocks being weathered, but it may be possible to capture large-scale features of the record.

2.4. Baseline fluxes

The C, O, P, S and N cycles are assumed to have been in approximate steady-state in pre-industrial time (referred to as the 'present') at least for the purpose of assigning a set of balanced baseline fluxes in the model. The slow variables in the model do not necessarily reach this steady state at present. The original model baseline fluxes are listed in Table 2, along with the changes made by Mills et al. (2014a), and some alternative proposals discussed here and tested in the Results section.

2.4.1. Sulphur cycle

The original COPSE and the updated version of Mills et al. (2014a) have no pyrite or gypsum degassing, pyrite weathering/burial of 0.53×10^{12} molS yr^{-1} and gypsum weathering/burial of 1.0×10^{12} molS yr^{-1}. We retain these fluxes initially and refer to them as 'low S' fluxes. Then in exploring a new set of baseline fluxes we introduce pyrite degassing (0.25×10^{12} molS yr^{-1}) and gypsum degassing (0.5×10^{12} molS yr^{-1}) and adjust pyrite weathering to 0.45×10^{12} molS yr^{-1} and gypsum weathering to 2.0×10^{12} molS yr^{-1}, to give the GEOCARBSULF set of fluxes (Royer et al., 2014), which we refer to as 'high S' fluxes. Burial of pyrite or gypsum is assumed to match the total of degassing and weathering in this case. Recent constraints on the pyrite burial fraction of total sulphur burial suggest it is 20-35% today (Tostevin et al., 2014), and our low and high sets of S fluxes sit at the upper and lower ends of this range respectively. Other work reconstructing sulphate evaporite burial fluxes on Laurentia has argued for a much larger pyrite burial fraction and associated pyrite oxidative weathering over much of Phanerozoic time (Halevy et al., 2012). However, this is at odds with sulphur isotope constraints, which suggest that pyrite burial only dominated in the early Paleozoic (Canfield, 2013).

2.4.2. Inorganic carbon cycle

Seafloor weathering was previously included at 1.75×10^{12} molC yr^{-1} (Mills et al., 2014a; Mills et al., 2014b) based on the midpoint of Cenozoic-Cretaceous estimates ~$0.5\text{-}3 \times 10^{12}$ molC yr^{-1} from deep sea drilling cores and estimated crust production rates. However, depending on assumptions about

the incorporation of sedimentary carbonates, seafloor weathering might range up to 4.1-5.7x10^{12} molC yr^{-1} (Alt and Teagle, 1999; Gillis and Coogan, 2011; Staudigel et al., 1989). Seafloor weathering was previously assumed (Mills et al., 2014a) to imply a reduction in terrestrial silicate weathering to 4.9x10^{12} molC yr^{-1} (from a baseline carbonate degassing of 6.65x10^{12} molC yr^{-1} from GEOCARB). However, the silicate weathering flux was already low compared to recent estimates, whereas the carbonate weathering flux (13.35x10^{12} molC yr^{-1} from GEOCARB) is high. The estimated total global CO_2 consumption flux by carbonate plus silicate weathering is ~20x10^{12} molC yr^{-1} (Amiotte-Suchet et al., 2003; Gaillardet et al., 1999; Hartmann et al., 2009; Munhoven, 2002) in good agreement with COPSE, but the apportioning is very different with ~60% silicate weathering (~12x10^{12} molC yr^{-1}) and ~40% carbonate weathering (~8x10^{12} molC yr^{-1}) (Hartmann et al., 2009). Furthermore, the contribution of volcanic rocks to silicate weathering is estimated to be ~17-25% (i.e. 2-3x10^{12} molC yr^{-1}) (Hartmann et al., 2009), significantly less than the ~30-35% or ~4.1x10^{12} molC yr^{-1} estimated previously (Dessert et al., 2003), with 35% (of 4.9x10^{12} molC yr^{-1}, i.e. 1.715x10^{12} molC yr^{-1}) having been used in the interim version of COPSE (Mills et al., 2014a). The implication that non-volcanic rocks contribute ~9-10x10^{12} molC yr^{-1} to silicate weathering is at the upper end of another recent estimate carefully accounting for uncertainties ~7.85 (5.78-9.93)x10^{12} molC yr^{-1} (Moon et al., 2014).

Given these considerations we view the inorganic carbon cycle fluxes used by Mills et al. (2014a) as a 'low' set of estimates. As a new set of 'high' inorganic C cycle fluxes we take 9x10^{12} molC yr^{-1} for non-volcanic weathering, 3x10^{12} molC yr^{-1} for volcanic weathering (i.e. 25% of silicate weathering; $k_{basfrac}$ = 0.25), 8x10^{12} molC yr^{-1} for carbonate weathering, and 3x10^{12} molC yr^{-1} for seafloor weathering, which we add to silicate weathering to give a total carbonate degassing 15x10^{12} molC yr^{-1} (more than a doubling of carbonate degassing relative to the original model).

2.4.3. Organic carbon cycle

The total organic carbon burial flux in the original COPSE of 9x10^{12} molC yr^{-1}, comprising marine-derived 4.5x10^{12} molC yr^{-1} and terrestrially-derived 4.5x10^{12} molC yr^{-1} components, is considerably

larger than in GEOCARB (~$5x10^{12}$ molC yr^{-1}) and in an earlier model based on organic carbon content of sediments (~$5x10^{12}$ molC yr^{-1}) (Berner and Canfield, 1989). However, it is comparable to other models (Slomp and Van Cappellen, 2007) and less than some estimates ≥$1x10^{13}$ molC yr^{-1} (Hedges and Keil, 1995; Holland, 1978). Total organic carbon burial is counterbalanced by oxidative weathering of organic carbon ($7.75x10^{12}$ molC yr^{-1}) and organic carbon degassing ($1.25x10^{12}$ molC yr^{-1}). A potential problem with high estimates of organic carbon burial is that the corresponding oxidative weathering flux is right at the upper limit ($7.78x10^{12}$ molC yr^{-1}) of estimates for the supply of organic carbon to weathering environments based on erosional rock flux and 0.4-0.6 wt% content of sediments (Daines et al., 2017), allowing no scope for incomplete oxidative weathering (which is widely recognised to occur and is assumed in COPSE). The discrepancy might be explained by a larger metamorphic flux of organic carbon degassing and/or by relatively rapid recycling of sedimentary organic carbon as thermogenic methane (Daines et al., 2017).

Terrestrial organic carbon burial is large in COPSE, but within the range of estimates for the terrestrial contribution to organic carbon burial in marine (mostly deltaic) settings today of ~$3.8±1.1x10^{12}$ molC yr^{-1}, which we base on ~80% (Galy et al., 2015) of ~$4.8±1.4 x10^{12}$ molC yr^{-1} (Burdige, 2005) being recent plant matter (the remaining ~20% being recycled ancient organic matter, i.e. kerogen). With the revision to the pyrite burial flux suggested above, the C/S ratio by mass of marine shales would be ~2.4 (assuming no terrestrial matter contributing), which is in the range of Cenozoic-Quaternary values (Raiswell and Berner 1986), but this would be higher assuming a (low S) terrestrial contribution to marine shales.

Given these considerations we view the original organic carbon burial and oxidative weathering fluxes in COPSE as a 'high' set of estimates. As an alternative 'low' set of fluxes we follow Daines et al. (2017) and consider $5x10^{12}$ molC yr^{-1} total organic carbon burial, split $2.5x10^{12}$ molC yr^{-1} marine and $2.5x10^{12}$ molC yr^{-1} terrestrially-derived, retaining $1.25x10^{12}$ molC yr^{-1} organic carbon degassing and therefore $3.75x10^{12}$ molC yr^{-1} oxidative weathering.

(Note that when the marine and/or terrestrially-derived organic carbon burial fluxes are adjusted the corresponding baseline marine organic phosphorus burial and/or phosphorus burial with terrestrial matter, and phosphorus weathering fluxes are adjusted to retain steady state. Also the baseline nitrogen fixation flux is adjusted to counterbalance any change in organic nitrogen burial.)

2.4.4. Phosphorus cycle

The total phosphorus weathering flux in the original COPSE of 43.5×10^9 molP yr^{-1} (of which 39×10^9 molP yr^{-1} went in reactive form to the ocean and 4.5×10^9 molP yr^{-1} was buried with terrestrial matter) is in the range of estimates for reactive P flux to the ocean of $23\text{-}155 \times 10^9$ molP yr^{-1} (Compton et al., 2000) and in good agreement with a recent estimate of P weathering of 37×10^9 molP yr^{-1} (1144×10^9 gP yr^{-1}) (Hartmann et al., 2014). That estimate may be low given it assumes stoichiometric release of P with SiO_2 and cations, whereas there is evidence for preferential release of P by biotic weathering (Lenton et al., 2012; Quirk et al., 2015).

The apportioning of the phosphorus weathering flux in the original model of k_{Psilw} = 2/12, k_{Pcarbw} = 5/12, k_{Poxidw} = 5/12 was based on an association with the relative size of Fe-P, Ca-P and Org-P burial fluxes. On reflection, this overestimates the contributions of carbonate and especially oxidative weathering and underestimates the contribution of silicate weathering, which inputs P from the mantle (via volcanic rocks) and from the crust (via non-volcanic silicates). Recent detailed estimates suggest P weathering input comes 29% from volcanic rocks, 16% from plutonic and metamorphic rocks, 14% from carbonates, and 41% from non-carbonate sediments (which also contribute ~50% to total silicate weathering) (Hartmann et al., 2014). An upper limit on the contribution of oxidative weathering to reactive P flux to the ocean based on shale stoichiometry and complete P release is ~8-13% (Compton et al., 2000), however analysis of weathered shale sequences suggests sedimentary organic P is more resistant to release than organic C (Kolowith and Berner, 2002), meaning this percentage should be lower. Given these considerations we suggest k_{Psilw} = 0.8, k_{Pcarbw} = 0.14, k_{Poxidw} = 0.06 as an improved apportioning. Applying $k_{basfrac}$ = 0.35 or 0.25 then gives a volcanic

weathering contribution of 28% or 20% to the P weathering flux, in reasonable agreement with the 29% inferred by (Hartmann et al., 2014).

The phosphorus burial fluxes in original COPSE of $18x10^9$ molP yr^{-1} as organic P (Org-P), $6x10^9$ molP yr^{-1} as Fe-adsorbed P (Fe-P), and $15x10^9$ molP yr^{-1} as calcium-bound P (Ca-P) (i.e. a 46%:15%:39% split of $39x10^9$ molP yr^{-1}), are relatively low compared to more recent estimates and models (Slomp and Van Cappellen, 2007), and the apportioning of P between sinks is questionable. More recent modelling suggests Org-P $20x10^9$ molP yr^{-1}, Fe-P $20x10^9$ molP yr^{-1}, and Ca-P $40x10^9$ molP yr^{-1}, i.e. a 25%:25%:50% split of $80x10^9$ molP yr^{-1} (Slomp and Van Cappellen, 2007). However, this represents a considerable increase in P weathering flux relative to current estimates (Hartmann et al., 2014). A smaller fraction of total P burial in organic form can help reconcile a larger total P burial flux with measured $(C:P)_{org}$ burial ratios ~200-250, which for Org-P ~$20x10^9$ molP yr^{-1} imply marine organic C burial ~$4\text{-}5x10^{12}$ molC yr^{-1}. However, a marine organic C burial flux of ~$2.5x10^{12}$ molC yr^{-1} (noting the discussion above) is hard to reconcile with an organic P burial flux of ~$20x10^9$ molP yr^{-1} as this implies a burial ratio $(C:P)_{org}$ of ~125 close to the Redfield ratio. Given these considerations we view the original P burial fluxes in COPSE as a plausible set of estimates. As an alternative apportioning of P burial fluxes we consider: Org-P $10x10^9$ molP yr^{-1} (for Org-C $2.5x10^{12}$ molC yr^{-1}), Fe-P $10x10^9$ molP yr^{-1}, and Ca-P $20x10^9$ molP yr^{-1}, with a corresponding adjustment of the P weathering flux.

2.5. Model implementation, initialisation and integration

The model is now coded in Matlab and the 'stiff' system of coupled ODEs is efficiently computed using a variable order ODE solver (Shampine and Reichelt, 1997). The model is initialised with the reservoir sizes in Table 1 but spun up from 1000 Ma to 550 Ma to give the sedimentary reservoir sizes time to adjust to the initial boundary conditions, in particular the differing Earth surface redox balance prior to plants. In the original study only a 50 Myr spin-up was used, meaning that the sedimentary (and to some degree sulphate) reservoirs were still adjusting during the early Paleozoic. For the original model configuration, by 550 Ma, the longer spin-up leads to a ~$0.9x10^{20}$ mol S or

~1.8x10^{20} mol O_2 eq. (~50%) increase in the pyrite reservoir (***PYR***), and a ~2x10^{20} mol C (~16%) decrease in the organic carbon reservoir (***G***), with a ~0.5x10^{20} mol S (~25%) or ~1x10^{20} mol O_2 eq. decrease in the gypsum (***GYP***) reservoir and ~1.6x10^{20} mol C (~3%) growth in the carbonate carbon reservoir (***C***). Thus the pyrite reservoir is predicted to have been roughly twice the size of the gypsum reservoir at the onset of the Phanerozoic, which seems reasonable given predominantly anoxic Precambrian oceans dominated by pyrite deposition, but some intervals of gypsum deposition in the Paleoproterozoic and Neoproterozoic (Lenton and Daines, 2017).

2.6. Comparison to data

We compare the predictions of the various model versions to six proxy data compilation targets for: CO_2, O_2, SO_4, $\delta^{13}C$, $\delta^{34}S$, and $^{87}Sr/^{86}Sr$, summarised in Table 6. The CO_2 proxy compilation (Royer, 2014) is derived from at least six different sources and although disagreement amongst the different methods has been reduced in recent studies, there are still some notable discrepancies, only partially captured by the +/- 1 s.d. uncertainty range used here. There is also a lack of proxy data prior to 420 Ma. The atmospheric O_2 mixing ratio reconstruction is based on the charcoal content of coals (Glasspool and Scott, 2010) scaled by the assumption of a lower limit on O_2 consistent with combustion of 15% and an uncertain upper limit consistent with continuous forests of 25-35%. Here we extend the 15% lower limit back to 420 Ma based on the presence of earlier charcoal reviewed in Lenton et al. (2016). Other studies would put the lower limit for self-sustaining combustion a little higher at 16-17% (Belcher and McElwain, 2008). More fundamentally, the underlying assumption of the method that more oxygen leads to more charcoal can be questioned, because charcoal is the product of pyrolysis, hence more oxygen fuelling combustion could conceivably reduce charcoal production. The other proxy data targets are more established. For SO_4 we consider only fluid inclusion data (avoiding reconstructions based on sulphur isotopes). The carbonate $\delta^{13}C$ compilation spans different organisms and depths which may generate some shifts in the record that do not reflect a truly global signature (Saltzman and Thomas, 2012). For $\delta^{34}S$ we only consider carbonate

associated sulphate (CAS). The $^{87}Sr/^{86}Sr$ record is from conodont apatite, extending LOWESS V5 (McArthur et al., 2012) prior to 503 Ma with data from Cox et al. (2016).

3. Results and Discussion

The above considerations represent a potentially bewildering set of multiple changes to the COPSE model. To clarify the effects of different changes we consider a series of cumulative changes to the model. First we revisit the original model predictions in the light of new proxy compilations. Then we look at the effect of updating the original forcing factors with the original model structure. Then we consider the effects of changing the structure and some key functions of the model (that we consider to be clear mechanistic improvements). Next we examine the effects of changing the baseline fluxes. Then we explore the effect of optional additional forcing factors. From this we arrive at an improved model with which we test some further mechanistic hypotheses for changes in the model functions.

3.1. Original model results in the light of new proxy compilations

First we revisit the original model predictions (black dashed line in Fig. 5) in the light of updated proxy records. Proxies for pCO_2 have generally been adjusted downwards since the original COPSE study hence the original model predictions of pCO_2 now appear too high for much of the mid-late Paleozoic (420-300 Ma), they are generally in the range of proxy uncertainty in the Mesozoic-Cenozoic, but miss a Triassic peak around 240-200 Ma. The original model predictions of O_2 are too low in the mid-Paleozoic (420-330 Ma), given the charcoal record at this time, reasonable from then until 60 Ma, but too high for the rest of the Cenozoic (50-0 Ma including at present). The original model predictions of SO_4 are reasonable for the Paleozoic but miss the Mesozoic-Cenozoic dip, because the interactive partial calcium cycle misses a Mesozoic-Cenozoic [Ca] peak. Predicted $\delta^{13}C$ captures the early Paleozoic mean ~0 ‰ (although none of its extreme variability), but it misses the persistent rise to ~+2 ‰ that occurs in the Late Ordovician, and the (imposed) peak ~350-280 Ma

does not match the observed structure well, although from ~200 Ma onwards the fit to the record is better. Predicted $\delta^{34}S$ fits the data reasonably well, indicating that this proxy does not constrain SO_4 well. We do not expect the original model to capture $^{87}Sr/^{86}Sr$ variability, because e.g. it has no distinction in the functional responses of volcanic and non-volcanic silicate rocks. It shows an overall rise in $^{87}Sr/^{86}Sr$ driven by Rb decay, and captures some of the structure of variability e.g. at ~350 Ma, because the original uplift forcing is derived from $^{87}Sr/^{86}Sr$ (but otherwise surprisingly little of it). Major deficiencies are a failure to capture the high early Paleozoic $^{87}Sr/^{86}Sr$ and the Mesozoic low followed by Cenozoic rise of $^{87}Sr/^{86}Sr$.

3.2. Updating the original forcing factors

Next we consider how the predictions of the original model are affected by updates to the original forcing factors (Fig. 3) with the results in Figure 5. This mirrors the approach of some of the intervening studies with COPSE (Lenton et al., 2012, 2016).

We show the combined effects of updating the degassing (*D*) and carbonate burial (*B*) forcing (blue in Fig. 5), because they both operate on degassing. The updated degassing (*D*) is responsible for increased CO_2 and O_2 250-130 Ma accompanied by slight increases in SO_4 and $\delta^{13}C$. The fit to CO_2 proxies 230-200 Ma and O_2 proxies 220-200 Ma is improved, but CO_2 is too high 160-140 Ma. The updated carbonate burial (*B*) forcing tends to counteract the updated degassing forcing (*D*) during 150-0 Ma. Together they slightly lower CO_2 and O_2 during 120-90 Ma and 60-30 Ma somewhat improving the fit to proxies. The updated uplift (*U*) forcing (red in Fig. 5) smooths out some of the variability in model predictions and leads to higher Mesozoic-early Cenozoic CO_2 and O_2 predictions. This generally improves the fit to CO_2 and O_2 proxies until ~130 Ma but degrades it ~120-50 Ma.

Combining the updated evolution (*E*), weathering (*W*) and CP_{land} forcing (green in Fig. 5) leads to an earlier drawdown of CO_2 and earlier rise of O_2, with a corresponding increase in $\delta^{13}C$ and SO_4 and decrease in $\delta^{34}S$. The Late Ordovician drawdown of CO_2 to ~8.5 PAL is close to the threshold for triggering Late Ordovician glaciations (Lenton et al., 2012; Pohl et al., 2014) and the fit to CO_2 proxies

410-370 Ma is much improved. The fit to O_2 proxies prior to 330 Ma is much improved, although O_2 ~12% in the Silurian is still too low to explain the first charcoal 420-400 Ma. The corresponding increase in $\delta^{13}C$ to ~1 ‰ is less than the observed rise to ~2 ‰, which also requires some selective enhancement of P weathering by early plants (Lenton et al., 2016), explored below. The corresponding decline in $\delta^{34}S$ is at the lower end of the data range.

Combining all the preceding forcing updates (black in Fig. 5) retains the improvement in mid Paleozoic CO_2 and O_2 predictions associated with the rise of plants. It increases predicted CO_2 310-270 Ma and 250-60 Ma and predicted O_2 prior to 50 Ma. Increased CO_2 310-270 Ma degrades the predictions, they are improved 240-200 Ma, but are too high again 180-140 Ma and 100-60 Ma. Increased O_2 is too high 90-60 Ma and at scattered times beforehand e.g. at 300 Ma.

In the following we take forward these updates to the *D*, *U*, *E*, *W*, *B* and CP_{land} forcings. Later we return to reconsider the CP_{land} forcing alongside the coal depositional area forcing, as well as adding a selective P weathering forcing (*F*).

3.3. Changing the baseline model structure

In developing the model we isolated which structural changes to the model have the most significant effects on CO_2, O_2 and the other predicted variables. Here we summarise the key controls.

3.3.1. Key controls on CO_2

The effect of changes to the controls on weathering, which primarily affect CO_2, are summarised in Figure 6 (contrast the results to the black dashed line). The inclusion of seafloor weathering (blue) makes a large contribution to drawing down CO_2, consistent with it varying in line with degassing (which is generally elevated above present). Making basalt weathering independent of uplift (red) also tends to significantly lower CO_2 when uplift is below present through most of the Phanerozoic (except the early Paleozoic). Distinguishing different activation energies for granite and basalt weathering (cyan) tends to increase CO_2 consistent with a lower overall activation energy and

therefore weaker negative feedback on CO_2 especially in the early-mid Paleozoic when both uplift and degassing are relatively high and therefore weathering flux is high. The new vegetation dependence of weathering (green) generates markedly higher CO_2 from the origin of plants onwards, consistent with the original function overestimating plant effects when *EW*<1. The new temperature function (magenta) noticeably lowers CO_2 in the mid-late Paleozoic and early Mesozoic. Combining all these changes to the weathering response in the model (black) generally leads to markedly lower CO_2 except ~400-350 Ma during the early rise of plants.

Changes to the model that alter CO_2 generally tend to alter O_2 in the same direction regardless of whether they have direct effects on the redox balance, because of the link between weathering and P input, and the link between CO_2, productivity and terrestrial organic carbon burial. The exception is the new temperature function (magenta), which has minimal effect on O_2 and other variables because it simply achieves the same weathering flux at a different CO_2 and temperature. Including seafloor weathering (blue) has the largest individual effect on O_2, lowering it throughout because it does not supply P whereas terrestrial weathering does (Mills et al., 2014b), and lowering it indirectly because lower CO_2 suppresses terrestrial productivity. This makes early-mid Paleozoic O_2 too low but fits the O_2 proxy better thereafter. Making basalt weathering independent of uplift (red) markedly lowers O_2 from the late Paleozoic onwards, because lower CO_2 suppresses vegetation productivity, and this improves the fit to the O_2 proxy. Distinguishing different activation energies for basalt and granite weathering and thus lowering overall activation energy (cyan) increases O_2 when it increases CO_2 (in the early Paleozoic and late Mesozoic-Cenozoic), degrading the fit to the O_2 proxy. The new vegetation dependence of weathering (green) has small effects on O_2 despite consistently increasing CO_2, because it has a counteracting direct effect of suppressing P weathering. Combining these changes (black) leads to markedly lower O_2 throughout, which is too low ~420-380 Ma.

Effects on SO_4, $\delta^{13}C$ and $\delta^{34}S$ are modest and do not help to distinguish between mechanisms, although it is worth noting that including seafloor weathering (blue) lowers SO_4 throughout because

terrestrial weathering fluxes, including gypsum weathering, are reduced, and making basalt weathering independent of uplift (red) lowers SO_4 later in the Phanerozoic because CO_2 is reduced and with it gypsum weathering. Effects on $^{87}Sr/^{86}Sr$ help evaluate these two mechanistic changes. Including seafloor weathering (blue) lowers $^{87}Sr/^{86}Sr$, improving the Mesozoic-Cenozoic fit to the data but degrading the Paleozoic fit. Making basalt weathering independent of uplift (red), leads to lower $^{87}Sr/^{86}Sr$ in the late Paleozoic, Mesozoic and Cenozoic, improving the overall fit to the data. Other changes have minor effects on $^{87}Sr/^{86}Sr$. Combining the changes (black) yields a reasonable fit to the $^{87}Sr/^{86}Sr$ record from ~160 Ma onwards but $^{87}Sr/^{86}Sr$ is too low through almost all of the Paleozoic and at present, consistent with a high initial choice of 0.35 for the volcanic rock fraction of silicate weathering (Table 2), following Mills et al. (2014a).

3.3.2. Key controls on redox balance, O_2, SO_4

Changes that primarily affect the model redox balance, O_2, SO_4 and only secondarily impact CO_2 are included in Figure 7 (again contrast the results to the black dashed line). Replacing the interactive Ca cycle with a prescribed ocean [Ca] (blue) (to broadly match sparse fluid inclusion data) yields a better fit to SO_4 data (as would be expected) and the Mesozoic-Cenozoic dip in SO_4 generates a corresponding small reduction in O_2. The new fire dependence of vegetation (red) has the greatest effect on O_2 increasing it during the early rise of plants and decreasing it once O_2 exceeds PAL, consistent with a stronger overall negative feedback on O_2 than in the original model. Removing the O_2 dependence of pyrite weathering (cyan) slightly lowers early Paleozoic O_2 and slightly increases O_2 after 350 Ma, consistent with the removal of a (weak) negative feedback. The secondary effects of these changes on CO_2 are generally very small, with the exception that revising the fire dependence of vegetation (red) increases the drawdown of CO_2 associated with the rise of early land plants, because the effect of removing fires on vegetation biomass is assumed greater. Effects on other predicted variables are modest. The new fire dependence of vegetation amplifies the initial rise in $\delta^{13}C$ with early plants but damps down changes in $\delta^{13}C$ once O_2 exceeds PAL, consistent with stronger negative feedback on organic carbon burial. It also has modest effects on SO_4 and $\delta^{34}S$.

Removing the O_2 dependence of pyrite weathering (cyan) modestly increases SO_4 and lowers $\delta^{34}S$ in the early Paleozoic.

3.3.3. Combined effects

Combining the changes that affect the redox balance leads to similar results (not shown) to just updating the fire dependence of vegetation (red). Combining the changes affecting the redox balance with those affecting CO_2 (green in Fig. 7) shows that altering the weathering functions has the greatest effects. Other changes to the baseline model (Table 4) include the quadratic dependence of the atmospheric fraction of CO_2, the new anoxia, denitrification and Fe-P burial functions. These have minimal individual effects on our key data targets (not shown). When these additional changes are combined with all of those discussed above, we arrive at the new baseline model structure (black in Fig. 7) which can be compared to the original model structure (black dashed).

Overall, the changes in model structure lead to lower predictions of CO_2 and O_2 throughout the Phanerozoic, with a similar pattern of variation (governed largely by the unchanged forcing factors). With the rise of the earliest plants, CO_2 drops closer to the first proxies at 420 Ma, and is in the range of the proxies 410-340 Ma, but remains too high 330-300 Ma. CO_2 is in the proxy range 290-240 Ma, but is at the lower end of the range or below it 230-100 Ma, when before it was generally too high. From 100-0 Ma the fit to the CO_2 proxies is somewhat improved. Early O_2 is too low, failing to rise to levels supporting combustion until ~380 Ma and not intersecting the proxy estimates until 330 Ma. Peak O_2 ~290 Ma is markedly reduced, but 280-240 Ma O_2 is too low. From 230-0 Ma the proxies are quite variable but predicted O_2 is broadly in the middle of the range with a much less pronounced Late Cretaceous peak, which previously was above the proxies. The Cenozoic O_2 decline reaches the present day value whereas previously it ended at 23% (~1.1 PAL). SO_4 predictions are improved by forcing with reconstructed [Ca] variations, but are a little below proxies 300-250 Ma, consistent with O_2 being too low at this time. $\delta^{13}C$ is lowered somewhat throughout, particularly after the rise of

land plants. $\delta^{34}S$ is relatively insensitive. The fit to the $^{87}Sr/^{86}Sr$ record is considerably improved in the Mesozoic-Cenozoic but degraded in the Paleozoic.

3.4. Changing the baseline fluxes

Here we apply alternative sets of model fluxes (Table 2) to the new baseline model (just described, including the updated *D*, *U*, *E*, *W*, *B* and CP_{land} forcing, and shown as the black dashed line), with the results shown in Figure 8.

Introducing the 'high' set of sulphur fluxes including pyrite and gypsum degassing (blue) decreases atmospheric CO_2 throughout and decreases atmospheric O_2 from the rise of plants onwards. SO_4 is increased from the latest Paleozoic onwards, improving the fit to late Paleozoic data but missing low SO_4 in fluid inclusions at ~100 Ma. $\delta^{34}S$ is not greatly altered consistent with its insensitivity to SO_4. $\delta^{13}C$ is lowered in the early-mid Paleozoic and increased from ~380 Ma onwards. $^{87}Sr/^{86}Sr$ is lowered slightly throughout. The effects on O_2 and CO_2 are predominantly due to the introduction of pyrite degassing, which always tends to decrease O_2 (the introduction of gypsum degassing tends to increase O_2 in the early Paleozoic but otherwise has little effect on CO_2 or O_2).

Adopting the 'high' set of inorganic carbon fluxes (red) increases atmospheric CO_2 and O_2 throughout the Phanerozoic. Atmospheric CO_2 is increased because seafloor weathering now makes up a smaller fraction of total terrestrial plus seafloor silicate weathering, and CO_2 has to adjust more for terrestrial silicate weathering to balance the carbon cycle (recalling that changes in degassing directly cause counterbalancing changes in seafloor weathering as well as there being a temperature-mediated negative feedback on seafloor weathering). Atmospheric O_2 is increased because the shift from seafloor to terrestrial weathering increases P input. Effects on SO_4, $\delta^{13}C$ and $\delta^{34}S$ are modest. There is a striking overall increase in $^{87}Sr/^{86}Sr$ due largely to a decrease in the volcanic rock fraction of silicate weathering from 0.35 to 0.25 (Table 2), which improves the fit to the data, particularly in the Paleozoic and at present.

Adopting the 'low' set of organic carbon fluxes (green) produces lower O_2 throughout. $\delta^{13}C$ is generally lowered consistent with a smaller organic fraction of total carbon burial, but from ~280 Ma onwards is notably below the long-term mean of +2 ‰. The lower O_2 allows plants to be more productive and amplify silicate weathering more, thus lowering CO_2 from ~380 Ma onwards. SO_4 is lowered in the early-mid Paleozoic and $\delta^{34}S$ increased. $^{87}Sr/^{86}Sr$ is increased slightly throughout.

Changing the split of P weathering (cyan) leads to higher O_2 almost all the time except ~350-310 Ma. This reflects the majority of P weathering now being linked to silicate weathering which is generally above present due to elevated degassing. Hence the biggest increases in O_2 are generally when degassing is highest in the early Paleozoic and Mesozoic. $\delta^{13}C$ is correspondingly increased at these times, improving fit to the Mesozoic data. CO_2 is increased from ~270 Ma onwards, because the higher O_2 tends to suppress vegetation and its effect on silicate weathering and this arguably improves fit to the proxy data. Effects on SO_4 and $\delta^{34}S$ are small. Changing the apportioning of P burial fluxes has tiny effects (not shown).

Relative to the new baseline (black dashed), a combined update of the fluxes (black) comprising high S fluxes, high inorganic carbon fluxes, low organic carbon fluxes, revised split of P weathering and revised split of P burial fluxes, yields increased atmospheric CO_2 in the early-mid Paleozoic and particularly the Mesozoic-Cenozoic, the latter improving fit to the proxies 230-110 Ma (but degrading it 100-60 Ma). It yields an increase in early Paleozoic O_2, improving fit to the constraints, similar values ~350-300 Ma, and somewhat higher O_2 ~250-0 Ma. SO_4 is somewhat higher throughout and $\delta^{34}S$ variations are reduced. $\delta^{13}C$ is higher in the early Paleozoic and Mesozoic improving fit to the long-term mean. $^{87}Sr/^{86}Sr$ is increased markedly throughout, considerably improving the (still poor) fit to data.

3.5. Introducing new forcing factors

We now take forward the new baseline model with this updated set of fluxes and the updated *D*, *U*, *E*, *W*, *B* and CP_{land} forcing (black dashed line), and consider the effect of additional forcing factors, with the results shown in Figure 9.

Basalt area forcing (blue), which is relatively low in the early-mid Paleozoic, tends to increase CO_2 until the East European craton event at ~380 Ma temporarily lowers it. CO_2 remains somewhat increased until the ~250 Ma Siberian traps emplacement, and then is decreased from the emplacement of the Central Atlantic Magmatic Province (CAMP) at ~200 Ma onwards, which creates greater than present volcanic rock area. The corresponding effect on $^{87}Sr/^{86}Sr$ is to increase it in the Paleozoic and decrease it in the Mesozoic-Cenozoic, which improves the overall fit to the data, including capturing the Phanerozoic minimum of $^{87}Sr/^{86}Sr$ in the Jurassic. Effects on O_2, SO_4, $\delta^{13}C$ and $\delta^{34}S$ are minimal.

Granite forcing (red), which is relatively high throughout the Paleozoic and early Mesozoic, tends to markedly decrease CO_2 until ~150 Ma, generally improving fit to proxy CO_2 except in the Triassic. $^{87}Sr/^{86}Sr$ is increased until ~100 Ma considerably improving the fit to data in the Paleozoic. O_2 is slightly lowered 400-200 Ma degrading the fit to constraints. SO_4 is somewhat lowered prior to ~150 Ma improving the fit to this proxy. Effects on $\delta^{13}C$ and $\delta^{34}S$ are small.

Paleogeography forcing (cyan) has marked effects of increasing CO_2 at two particular times of reduced runoff and dry continental interiors; in the early Paleozoic when there is a lack of proxy constraints, and in the Permian-Triassic-Jurassic (~300-150 Ma). The pronounced Triassic CO_2 peak better fits proxy data. Increased CO_2 represents a readjustment of climate to achieve the same weathering flux. Hence effects on O_2, SO_4, $\delta^{13}C$, $\delta^{34}S$ are minor, with only a slight dip in $^{87}Sr/^{86}Sr$, meaning these tracers do not provide a further test of the forcing.

Coal depositional area forcing combined with a ramping down of the CP_{land} forcing over 345-300 Ma (green) generates an increase in O_2 over 320-240 Ma with a Carboniferous-Permian O_2 peak centred on ~300 Ma that improves the fit to the charcoal-based proxy. $\delta^{13}C$ is increased 330-230 Ma reflecting increased organic carbon burial. A corresponding peak in CO_2 is generated which is above proxies. Effects on SO_4, $\delta^{13}C$ and $\delta^{34}S$ are minimal.

Including an interval of elevated selective weathering of P over 465-400 Ma (together with a combination of all the other new forcing factors; black), generates a 'hump' in atmospheric O_2 and $\delta^{13}C$, improving consistency with the earliest charcoal record ~420 Ma onwards, and producing the observed $\delta^{13}C$ +2 ‰, as well as oxygenating the ocean (Lenton et al., 2016). SO_4 is also somewhat increased and $\delta^{34}S$ somewhat decreased at this time.

The combination of all the new forcing factors (black), relative to the model without them (black dashed), yields markedly lower early Paleozoic CO_2 and higher Permian-Triassic CO_2. The overall fit to the $^{87}Sr/^{86}Sr$ record is markedly improved although it is still too low in the earliest Paleozoic and misses a pronounced dip in the Permian. Atmospheric O_2 and $\delta^{13}C$ are noticeably improved in parts of the Paleozoic.

With all the various updates to the baseline model, the sedimentary reservoirs behave somewhat differently, with slightly greater growth of the organic carbon reservoir and notably greater shrinkage of the pyrite sulphur reservoir over Phanerozoic time, leading to normalised reservoir sizes of ***g***=1.075, ***c***=0.98, ***pyr***=0.75, ***gyp***=1.25 at present. Much of the deviation from assumed present day reservoir sizes is due to the introduction of pyrite and gypsum degassing fluxes, and a Mesozoic interval of elevated sulphur degassing in which the gypsum reservoir grows at the expense of the pyrite reservoir. However, as the present day sedimentary reservoirs are not that well known and the predictions of surface redox reservoirs of oxygen and sulphate are relatively insensitive to changing the sedimentary reservoir initialisation, we conclude that this mismatch is not a major concern.

3.6. Testing hypotheses

Taking the revised baseline model subject to both the updated original forcing factors and the new forcing factors (black dashed line in Figs. 10-12) we now consider some key uncertainties regarding controls on CO_2 and alternative hypotheses for controls on O_2.

3.6.1. Controls on weathering and CO_2

We start with key controls on terrestrial and seafloor weathering and hence CO_2 (Fig. 10).

In GEOCARB III, Berner switched from the use of k_{15} = 0.15 (~7-fold amplification of weathering by plants) to k_{15} = 0.25 (4-fold amplification by vascular plants relative to moss/lichen cover) based mostly on a field study in Iceland (Moulton et al., 2000). He also explored k_{15} = 0.1 (10-fold amplification). In COPSE, k_{15} = 0.25 (blue) predictably leads to lower early Paleozoic CO_2 ~6-7 PAL (and lower temperatures ~16 °C, as opposed to ~18 °C with k_{15} = 0.15). After the rise of the first plants CO_2 drops to ~5 PAL which is just below proxies at 420 Ma. Using k_{15} = 0.1 (red) gives higher early Paleozoic CO_2 ~14-18 PAL (and higher temperatures ~20 °C). The rise of the first plants draws CO_2 down to ~7 PAL, which is consistent with Late Ordovician glaciations (Lenton et al., 2012) and whilst high at 420 Ma is within the 410-390 Ma proxy range. The CO_2 predictions for k_{15} = 0.1 are considerably lower than in GEOCARB III for the same parameter setting presumably because COPSE includes a second negative feedback on CO_2 from seafloor weathering, which plays a more significant role when abiotic weathering (k_{15}) is lower. This can help explain why decreasing k_{15} and increasing CO_2 gives slightly lower Paleozoic O_2, because now seafloor weathering makes up a larger fraction of the CO_2 removal flux but is not a source of P. It also explains why early Paleozoic $^{87}Sr/^{86}Sr$ is somewhat lowered. Conversely increasing k_{15} and lowering CO_2 gives slightly higher Paleozoic O_2, because continental weathering is now a larger fraction of the CO_2 removal flux with a correspondingly increased source of P, and $^{87}Sr/^{86}Sr$ is somewhat increased. Early Paleozoic SO_4 shows a small change in the same direction as O_2 but there is no significant effect on $\delta^{34}S$ or $\delta^{13}C$. Thus the best chance to evaluate the strength of the biotic weathering effect is from comparison to

CO_2 proxies, which are most consistent with the default ~7-fold amplification of weathering (k_{15} = 0.15).

Making weathering dependent on vegetation NPP rather than biomass (green) removes any effect of fires suppressing weathering by suppressing biomass. This leads to a somewhat slower drawdown of CO_2 with the early rise of plants (because the beneficial effect of fewer fires on vegetation now does not affect weathering). There are markedly smaller CO_2 variations after the rise of plants, and correspondingly a more stable temperature, reflecting a more effective negative feedback on CO_2 and climate when it is not affected by O_2 variations. Effects on O_2 are tiny, whereas there are small but noticeable effects on $\delta^{13}C$ because carbon isotope fractionation is assumed to be sensitive to CO_2 level. There are no significant effects on $^{87}Sr/^{86}Sr$, SO_4, or $\delta^{34}S$. Hence the best evaluation is against CO_2 proxies, which are better fitted in the latest Paleozoic, but the model predictions appear rather low in parts of the Jurassic-Cretaceous.

Giving seafloor weathering stronger temperature sensitivity (cyan) generally lowers CO_2, O_2 and $^{87}Sr/^{86}Sr$ except in the late Paleozoic. It is unclear whether overall this improves the fit to data. Removing the temperature sensitivity of seafloor weathering (magenta) markedly increases CO_2 and O_2 and somewhat increases $^{87}Sr/^{86}Sr$. This creates Permian-Triassic CO_2 levels above the proxies and increases late Cretaceous-early Ceonozoic CO_2 above proxies.

Varying climate sensitivity (Fig. 11) predominantly affects CO_2 predictions. O_2, $\delta^{13}C$ and SO_4 change in the same direction as CO_2 but by relatively small amounts. Prior to the rise of plants, temperature changes in the opposite direction to CO_2, because they are jointly determining the abiotic weathering flux (e.g., a decrease in climate sensitivity lowers the temperature requiring an increase in CO_2 and temperature to attain the same weathering flux, but because both CO_2 and temperature increase the weathering flux, the temperature does not have to increase to its original value). After the rise of plants, temperature predictions are little altered, because the biotic weathering flux is controlled by temperature and insensitive to CO_2 (as the Michaelis-Menten response of plants tends

to be saturated) hence variations in climate sensitivity alter CO_2 to achieve roughly the same temperature. Halving the climate sensitivity to 1.5°C (blue) demands much larger increases in CO_2 throughout to maintain balance in the carbon cycle, putting predicted CO_2 well above proxies most of the time, and can be ruled out on these grounds. Early Paleozoic temperature is also decreased from ~18°C to ~15°C (not shown), although early Paleozoic $^{87}Sr/^{86}Sr$ is increased, slightly improving the fit to data. A more modest decrease in climate sensitivity to 2.25°C (green) is more consistent with the CO_2 proxies, indicating that they help provide a lower bound on climate sensitivity (Royer et al., 2007). Doubling the climate sensitivity to 6°C (red) lowers CO_2 throughout, putting it below proxies in the early Devonian and mid Triassic, although the fit is improved at some other times. Early Paleozoic temperature is increased from ~18°C to ~22°C (not shown), but early Paleozoic $^{87}Sr/^{86}Sr$ is decreased, further degrading the already poor fit to data. A more modest increase in climate sensitivity to 4.5°C (cyan) is more consistent with the wider literature (IPCC, 2013) and provides a somewhat better fit to CO_2 proxies than with a 6°C climate sensitivity. Hence we consider 2.25-4.5°C as a reasonable uncertainty range on climate sensitivity.

3.6.2. Controls on O_2

Turning to controls on O_2 we first tried removing the dependence of oxidative weathering of organic carbon on O_2 as suggested by Berner (2006a). However, this causes O_2 levels to drop to zero (not shown), with the long model spin-up (and this also happens in the original model 'run 3' of Bergman et al., 2004, when using our longer spin-up). The reason is a simple lack of negative feedback on O_2, and given evidence for an O_2 sensitivity of oxidative weathering we retain it in the model.

The results of testing other hypotheses for controls on O_2 are summarised in Figure 12.

Next we tested the effects of Berner's (2006a) proposal that organic carbon burial is predominantly controlled by erosion. Forcing terrestrial-derived organic carbon (and phosphorus) burial with uplift/erosion (blue) leads to lower predicted O_2 when uplift is below present, especially in the Triassic-Jurassic, although O_2 is still sufficient to sustain combustion at this time. CO_2 is also lowered

from 330 Ma onwards degrading the fit to proxies in the Mesozoic. $\delta^{13}C$ is lowered when uplift is below present because the reduction in terrestrial-derived organic carbon burial causes a corresponding reduction in total organic carbon burial. Forcing marine organic carbon burial with uplift/erosion (red) leads to almost identical effects on O_2. Effects on CO_2 are also comparable. However, there is little effect on $\delta^{13}C$ because the reduction in O_2 levels leads to a compensatory increase in terrestrial productivity and terrestrially-derived organic carbon burial. Forcing both marine and terrestrial-derived organic carbon burial with uplift/erosion (green) (leaving only burial of terrestrial material in coal basins independent of uplift) leads to markedly lower O_2 especially in the later Triassic-Jurassic when it is insufficient to sustain combustion and therefore inconsistent with the charcoal record. CO_2 is also lowered from 330 Ma onwards, because there is less suppression of vegetation by fire and therefore faster weathering, and is well below proxies through much of the Mesozoic. $\delta^{13}C$ is markedly lowered and clearly below the proxy record in the Triassic. Given these deficiencies we rule out this model version.

Finally we considered alternative marine-based feedbacks on atmospheric oxygen. Including a direct feedback of O_2 on marine organic carbon burial (cyan) leads to smaller O_2 variations overall, including an early Paleozoic increase and slight lowering of later peaks, consistent with an additional negative feedback (some small CO_2 effects go along with this). However, early Paleozoic $\delta^{13}C$ is increased and $\delta^{34}S$ decreased away from the proxy data. Including Van Cappellen and Ingall's (1996) feedback of anoxia on $(C/P)_{organic}$ burial ratio (magenta) increases early Paleozoic O_2, but has no effect after the rise of plants because anoxia never significantly returns to the ocean. It also increases early Paleozoic $\delta^{13}C$ and decreases early Paleozoic $\delta^{34}S$ away from the proxy data. Including anoxia-sensitive Ca-P burial has almost identical effects on O_2 and the other variables as the Van Cappellen and Ingall (1996) feedback (hence is not shown).

3.7. Robust features and remaining uncertainties

We present the new baseline model run and a summary of the preceding uncertainty analysis (Section 3.6) as a grey shaded area around it in Figure 13; adding the variables of global temperature, anoxic fraction, ocean nitrate and ocean phosphate concentration, to pCO_2 (PAL) and plotting pO_2 (PAL) rather than mixing ratio (%). The greatest uncertainty for most of these variables is, appropriately, in the early Paleozoic. This summary figure and the full set of earlier model results allow us to establish which model predictions withstand testing against proxy data and are robust to current uncertainties, and which critical uncertainties remain that could be targeted by future work. We arrange this chronologically into phases in the development of the Phanerozoic Earth system.

Phase 1 is the early Paleozoic, specifically the Cambrian and the early Ordovician prior to the rise of land plants (~550-465 Ma). Atmospheric CO_2 levels at this time are particularly uncertain due to a lack of proxies and because COPSE cannot reproduce the unusually high $^{87}Sr/^{86}Sr$. This suggests that despite the assumed much greater non-volcanic silicate rock area and much smaller volcanic rock area relative to the present, we are still missing a yet more radical change in lithology (e.g. ongoing effects of the pan-African orogeny; Goddéris et al., 2017) or a marked reduction in hydrothermal input of Sr (which might imply lower degassing than assumed). Global temperature predictions from such a simple model should be viewed as 'zeroth-order' given that many climatic factors are not included. Nevertheless relatively warm predicted temperatures of 16-21°C are broadly consistent with no ice at the poles in the Cambrian-early Ordovician.

The model robustly predicts low atmospheric O_2 ~0.2 (0.1-0.4) PAL or ~5 (3-10) % mixing ratio and widespread ocean anoxia in the early Paleozoic, supported by low $\delta^{13}C$ and high $\delta^{34}S$ (as well as several independent redox proxies). In the model, the principal O_2 regulator around ~0.2 PAL is the oxygen sensitivity of oxidative weathering, as postulated for much of the Proterozoic as well as the earliest Phanerozoic (Daines et al., 2017). The upper part of the O_2 uncertainty range includes additional marine-based negative feedbacks on O_2, but we consider these O_2 values and the

corresponding feedbacks less plausible because they tend to increase predicted $\delta^{13}C$ and decrease predicted $\delta^{34}S$ away from the data. Such low O_2 ~0.2 PAL is still consistent with the estimated metabolic needs of the Cambrian fauna (Sperling et al., 2015a). The high predicted anoxic fraction should be viewed semi-quantitatively given the schematic nature of the function. Nevertheless complex models show that the deeper ocean would be mostly anoxic for O_2 ~0.2 PAL and limiting nutrient concentration near present levels, assuming a biological carbon pump (Lenton and Daines, 2017). The large increase in anoxia relative to today qualitatively alters the predicted nutrient balance of the early Paleozoic ocean, supporting a much larger increase in water-column denitrification and a corresponding increase in phosphate relative to the Redfield ratio, such that nitrogen fixation can balance denitrification. The prediction of high ocean [PO_4] is consistent with evidence from iron formations combined with the inference of high ocean [Si] (Planavsky et al., 2010). It does not, however, equate to higher new production or organic carbon burial in COPSE, because available nitrogen (the limiting nutrient) is at comparable levels to today. The early Paleozoic ocean is predicted to be 'non-Redfieldian' with N/P ~5-6 (rather than today's N/P ~14), consistent with the response of nitrogen cycling to anoxic oceans in the GENIE model (Lenton and Daines, 2017).

Phase 2 is the mid Paleozoic rise of land plants, spanning the Late Ordovician-Silurian-Devonian-early Carboniferous (~465-350 Ma). Assuming early Paleozoic CO_2 and temperature were relatively high, a two-phase drawdown of atmospheric CO_2 and temperature – in the Late Ordovician and Devonian-early Carboniferous – best fits available proxy data. The model associates the first drawdown phase with the rise of the earliest non-vascular plants and the second with the rise of rooted vascular plants (including trees). It also supports a large amplification of weathering rates by vegetation, likely greater than the factor of 4 used in GEOCARBSULF and potentially up to a factor of 10. Predicted Late Ordovician CO_2 levels are sufficiently low to explain glaciation at this time, which thanks to the unusual paleogeography could have been abruptly triggered at relatively high global temperature (Pohl et al., 2014; Pohl et al., 2016). COPSE predicts the second phase of CO_2 drawdown

associated with the rise of vascular plants 400-350 Ma caused greater global cooling (partly a simple consequence of the natural logarithmic dependence of temperature on CO_2). This produces the lowest predicted global temperatures of the Phanerozoic, consistent with the longest-lived interval of glaciations stretching to the lowest latitudes being during the Carboniferous-Permian.

A 'mid-Paleozoic oxygenation event' is robustly predicted, i.e. a major rise in atmospheric O_2 and associated oxygenation of the ocean due to the rise of land plants. This represents a change in the oxygen regulation regime, from the predominant negative feedback being on the sink of oxygen (oxidative weathering) to being on the source (organic carbon burial). This requires a substantial secular increase in organic carbon burial, which is here associated with the earliest, non-vascular land plants (Lenton et al., 2016) (unlike in the original COPSE model where it is associated with the later evolution of trees). Others argue that earliest plant productivity and/or effects on weathering could not have been large enough to affect such a change (Edwards et al., 2015; Quirk et al., 2015), but we have yet to find any other way of reproducing the secular changes observed in the multi-proxy record, including the appearance of fossil charcoal by ~420 Ma. The predicted rise of oxygen and oxygenation of the oceans continues with the rise of rooted, vascular plants, but as the oxygen regulation regime has already shifted it proves harder for them to cause changes in atmospheric O_2. The predicted dip in O_2 and reassertion of ocean anoxia at ~395 Ma is a consequence of the imposed phosphorus weathering forcing designed to reproduce a transient drop in $\delta^{13}C$ at this time, but O_2 goes too low given that there is charcoal through this interval (Lenton et al., 2016). It serves to illustrate that the Earth surface redox state could have been particularly sensitive during this oxygenation transition, although the real Earth system had anoxic events later in the Devonian (Algeo and Scheckler, 1998).

With plants established, the model Earth system thereafter is in a regime where atmospheric CO_2 tends to be regulated most strongly against decreases (i.e. regulation against a lower limit) and O_2 against increases (i.e. regulation against an upper limit). There are subsequent variations in both CO_2

and O_2 but they are smaller than the mid-Paleozoic transition, and tend to be reversible rather than one-way changes (albeit very long-lived). Consequently, we treat the rest of the Phanerozoic as 'Phase 3', but we divide it into two parts based on two modelled CO_2 and O_2 positive excursions.

Phase 3a is the late Paleozoic-early Mesozoic, spanning the Carboniferous-Permian-Triassic (~350-200 Ma) and including the finale of supercontinent (Pangea) formation. There is a broad predicted peak of CO_2 in this interval, rising through the later Carboniferous and Permian to a Triassic peak. However, predicted atmospheric CO_2 is particularly uncertain because the model cannot reproduce the marked Permian drop in $^{87}Sr/^{86}Sr$, which may indicate uncaptured changes in degassing or lithology. Paleogeography forcing (a particularly dry supercontinent interior) can help explain the Triassic peak seen in CO_2 proxies, as would a decoupling of seafloor weathering from surface temperature changes, or a reduction in climate sensitivity. Subsequently the model predicts a CO_2 minimum at ~200 Ma around the Triassic-Jurassic boundary which is not seen in proxies. The CO_2 drop is due to a mix of LIP emplacement (CAMP), a dip in reconstructed degassing, and a rapid recovery of wetter continental weathering conditions. Part of the problem with the model here is that the CAMP is assumed to weather too rapidly as there is an excessively rapid negative shift in $^{87}Sr/^{86}Sr$.

The model predicts a peak in O_2 ~1.35 (1.3-1.4) PAL or ~26.5 (25.5-27) % mixing ratio, centred on ~290 Ma and associated with the Carboniferous-Permian interval of coal deposition. This is comparable to the O_2 peak predicted in the original COPSE (Bergman et al., 2004), but below the ~35% (Berner and Canfield, 1989) or ~30% (Berner, 2006a) peak levels predicted with other models. O_2 drops to a predicted minimum ~1 (0.85-1.05) PAL or ~21 (18-22) % mixing ratio centred on ~200-190 Ma, which is associated with low organic carbon burial rates including a hiatus in coal deposition during the Triassic. This is consistent with the charcoal record which shows that O_2 was sufficient to sustain combustion at this time, and in the model this requires that no more than about half of total organic carbon burial can be controlled by erosion. The maximum and minimum in O_2 are linked to a

corresponding predicted maximum and broad minimum in $\delta^{13}C$. The predicted $\delta^{13}C$ fluctuations are comparable in size to those seen in the data compilation, but COPSE does not reproduce the timing and higher frequency of those $\delta^{13}C$ fluctuations well, hence the real O_2 record may have exhibited more fluctuations of different timing, albeit within similar bounds. A rise in SO_4 to a Permian peak is also predicted, which is due partly to rising O_2 but mostly to an assumed decline in ocean [Ca], which then reverses in the Late Permian.

Phase 3b is the mid-late Mesozoic and Cenozoic, spanning the Jurassic-Cretaceous-Paleogene-Neogene (~200-0 Ma), and including the rise of calcareous phytoplankton and the break-up of the supercontinent (Pangea) – with increasing uplift and a peak then decline in degassing. The model captures an overall peak then decline of CO_2 driven by the peak in degassing (and to some degree the rise of uplift), but it does not capture the finer scale structure suggested by the proxy compilation. The Phanerozoic minimum and then major rise in $^{87}Sr/^{86}Sr$ is reasonably well captured and attributable to both a decline in degassing causing a decline in hydrothermal Sr input (and shift from seafloor to terrestrial weathering) and a decoupling of volcanic weathering from uplift such that as uplift increases there is a marked shift from weathering of volcanic rocks to ancient cratons (Mills et al., 2014a). The broad global temperature peak in the Late Cretaceous is consistent with paleoclimate reconstructions. The subsequent Paleocene-Eocene peak in temperature is missing, because the model fails to predict a peak in CO_2 at this time, and it also fails to capture corresponding stable values of $^{87}Sr/^{86}Sr$ (followed by an accelerated rise). Together these deficiencies may indicate an unresolved Paleocene-Eocene peak in degassing and hydrothermal Sr input. The model does predict a cooling at ~35 Ma (near the Eocene-Oligocene boundary) due to LIP emplacement (the 'Afar' event) driving a CO_2 decline.

A broad Late Cretaceous (~90-70 Ma) peak of O_2 ~1.3 (1.15-1.5) PAL or ~26 (23.5-28.5) % mixing ratio is robustly predicted, albeit at lower O_2 levels than in the original model. It is driven by a peak in degassing and consistent with abundant Cretaceous charcoal. The predicted Cenozoic decline in

O_2 is robust. A corresponding predicted decline in $\delta^{13}C$ is consistent with proxies but due more to changing isotope fractionation than to a decline in organic carbon burial.

4. Conclusion: forward look

The process of revising the COPSE model and comparing its predictions to proxy data reveals a mixed picture with regard to constraining the forcing factors and mechanisms at play in controlling Phanerozoic CO_2 and O_2 variations. Trying to reproduce the long timescale structure of $^{87}Sr/^{86}Sr$ does help constrain key processes of seafloor weathering and the decoupling of volcanic weathering from uplift that control both CO_2 and O_2 levels. Trying to reproduce the $\delta^{13}C$ record helps constrain past O_2 variations. However, predicting $\delta^{34}S$ offers little constraint on O_2 or even SO_4, and whilst predicting SO_4 offers some weak constraint on O_2 it is more sensitive to (prescribed) ocean [Ca]. Hence in future there is a need to explore a wider range of proxy data targets to see if they can help constrain model mechanisms and forcing factors. This in turn may invite a more spatially-resolved modelling approach for those proxies (e.g. of ocean redox state) that are clearly influenced by both local and global processes and which hence it is difficult to treat in a globally-averaged way.

Clearly a simplified box model such as COPSE is not expected to capture all features of the proxy record. More spatially elaborate models are already being used to examine past changes in weathering (Donnadieu et al., 2006; Goddéris et al., 2014) and in ocean composition (Lenton and Daines, 2017). In principle a simple model can be calibrated on the results of more realistic complex models, as is done e.g. for the global temperature function from GEOCARBSULF used here. Equally new forcing factors can be introduced to represent things not resolved by a simple model, for example the paleogeography forcing developed for GEOCARBSULF and applied here. However adding such forcing factors detracts from the transparency of a simplified approach and it runs the risk of over-fitting it to available data. If one can almost as easily run a more realistic, spatially-

resolved model then that may be a better way to go. Indeed we are developing a framework whereby more elaborate box models can be coupled together and applied to deep time questions.

We have also begun to extend the application of COPSE further back in time to simulate changes in the Proterozoic Earth system (Daines et al., 2017; Mills et al., 2014b). Further work is needed to capture Precambrian forcing, including a more generic approach to the effects of the super-continent cycle on degassing, uplift and LIPs, and the effects of the Earth's decaying internal heat source on degassing. Equally the nature of redox and nutrient cycling in a more anoxic ocean needs elaboration. In principle the model could be extended even further back in time through the Great Oxidation, but this would require some representation of the contribution of methane (and potentially other greenhouse gases) to global temperature.

The results of the present study suggest that there was a major, potentially two-phase, drawdown of atmospheric CO_2 with the rise of land plants and associated cooling in the Late Ordovician and Devonian-early Carboniferous. Thereafter atmospheric CO_2 was well regulated, particularly against decreases, but there were peaks in the Triassic and mid-Cretaceous. Not all of the structure in the CO_2 proxy record is captured, which given its strong dependence on forcing factors suggests that reconstructions of degassing, uplift and changing lithology could be significantly improved.

A mid-Paleozoic oxygenation event is robustly predicted, i.e. a major rise in atmospheric O_2 and associated oxygenation of the ocean due to the rise of land plants. Atmospheric O_2 is effectively regulated thereafter with remaining fluctuations being a Carboniferous-Permian O_2 peak (~26%) linked to burial of terrestrial organic matter in coal swamps, a Triassic-Jurassic O_2 minimum (~21%) linked to low uplift, a Cretaceous O_2 peak (~26%) linked to high overall degassing and weathering fluxes, and a Cenozoic O_2 decline. Two of these robust features are qualitatively at odds with other models. First, COPSE predicts much lower O_2 in the early Paleozoic than GEOCARBSULF or MAGic, consistent with marine redox proxies (Lenton et al., 2016; Sperling et al., 2015b), whilst still being consistent with the metabolic O_2 requirements of early animals (Sperling et al., 2015a). Second,

COPSE predicts a Mesozoic peak then Cenozoic decline of O_2 rather than a monotonic Mesozoic-Cenozoic rise of O_2 as seen in some versions of GEOCARBSULF (Berner et al., 2007; Falkowski et al., 2005). The latter prediction is made by inverting the $\delta^{13}C$ record, but it has been shown that this technique can also produce high Mesozoic O_2 followed by a Cenozoic O_2 decline (Mills et al., 2016), consistent with COPSE.

Acknowledgements

We thank Josh Williams for assistance with the basalt area forcing, Noam Bergman for developing the original COPSE model, Andy Watson for input to COPSE over the years, the late Bob Berner for pioneering the field of Phanerozoic biogeochemical modelling, and Dana Royer and an anonymous referee for constructive reviews.

The revised COPSE model code, written in Matlab and under Github version control, is available at https://github.com/sjdaines/COPSE/releases. The code is also available from the lead author on request.

Funding: This work was supported by the Natural Environment Research Council [grant numbers NE/P013651/1, NE/N018508/1] (to T.M.L. and S.J.D.); a Royal Society Wolfson Research Merit Award (to T.M.L.); and a University of Leeds academic fellowship (to B.J.W.M.).

Figures and captions

(a)

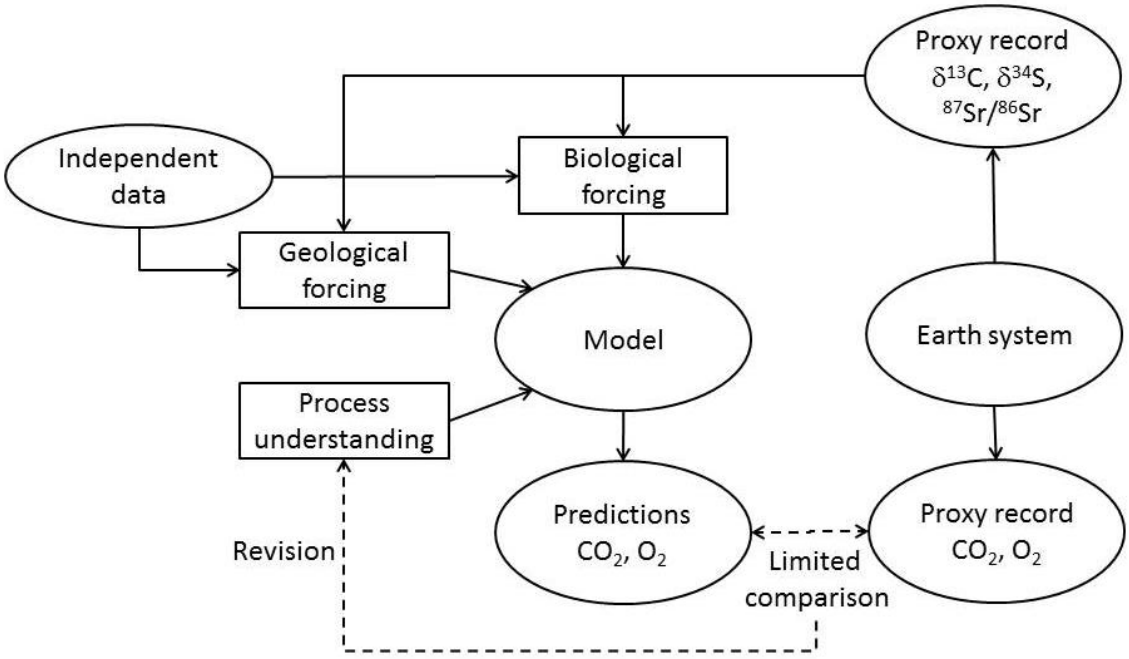

(b)

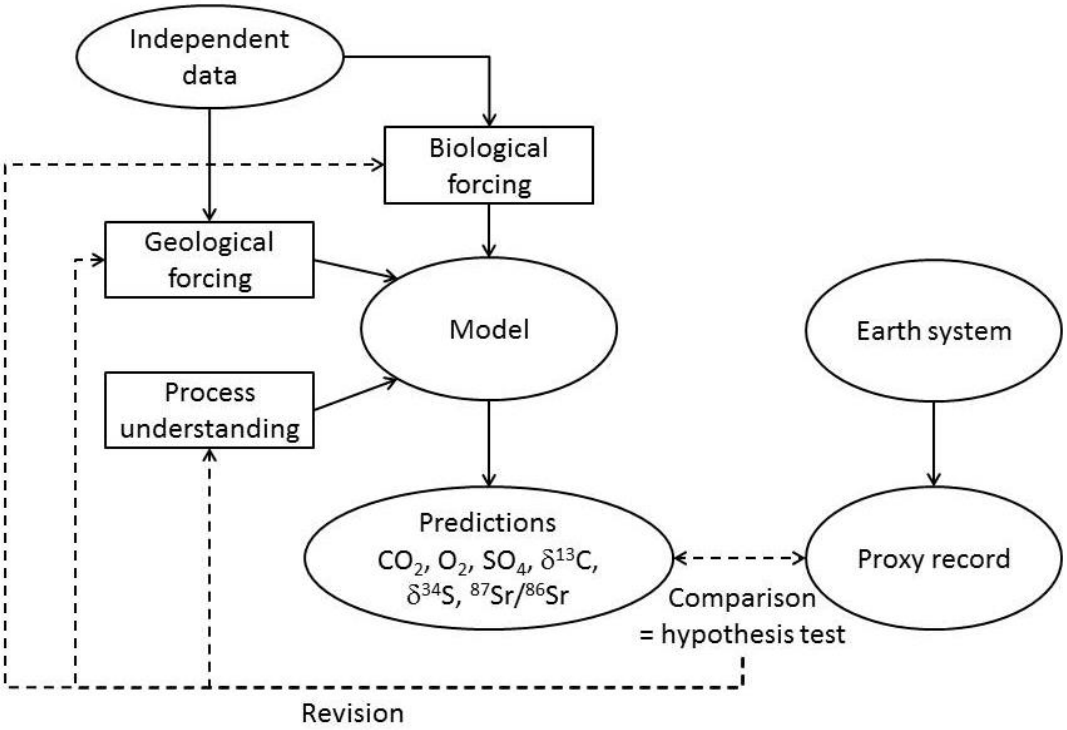

Figure 1. Different approaches to modelling Phanerozoic biogeochemical cycling: (a) inverse modelling approach (b) forwards modelling approach (pursued herein).

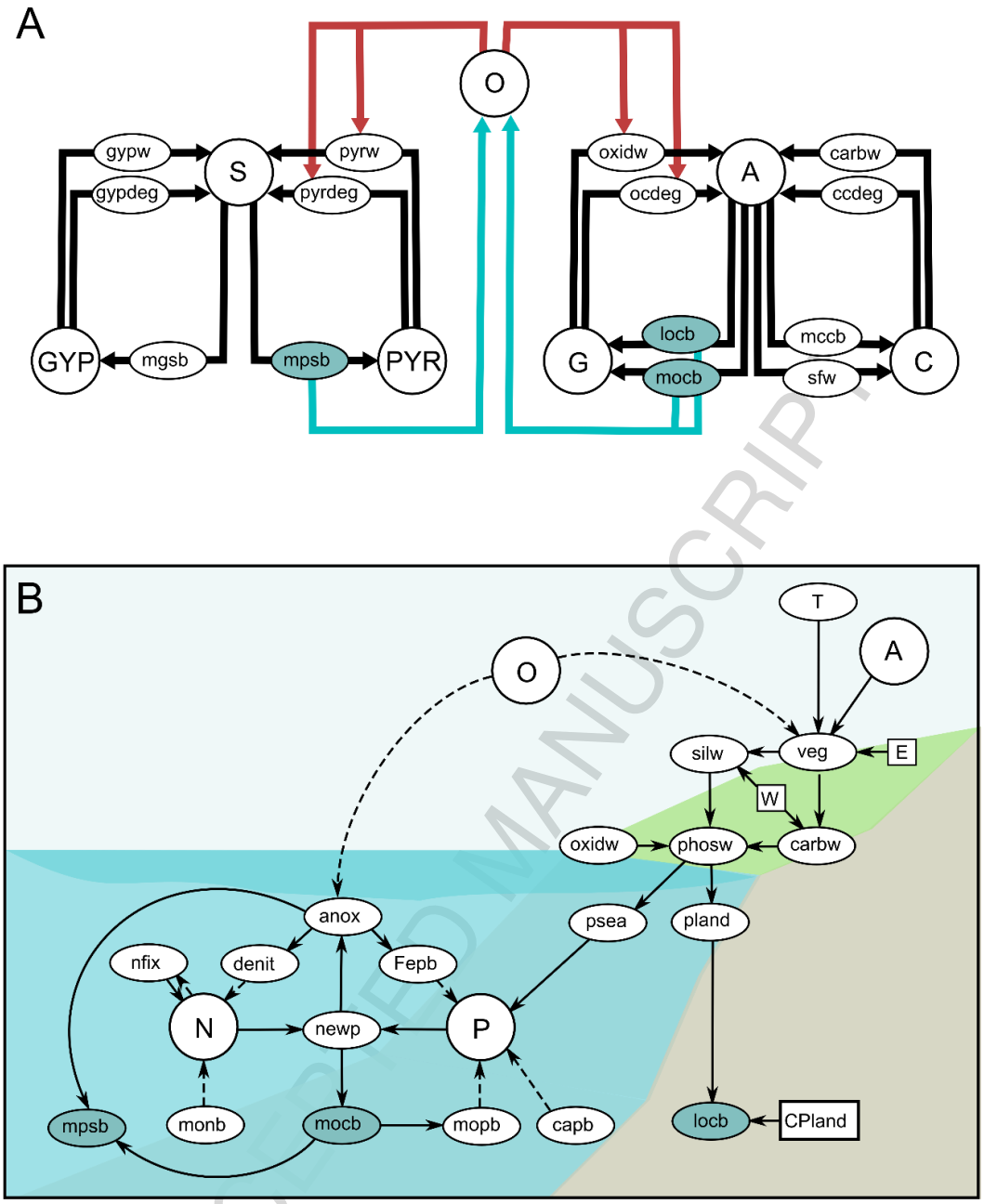

Figure 2. COPSE model schematic: (A) Carbon, Sulphur and Oxygen cycle fluxes. Here arrows show mass fluxes, blue arrows show oxygen sources and red arrows show oxygen sinks. (B) Dynamic nutrient and biosphere system. Here arrows show positive/direct (solid) or negative/inverse (dashed) relationships between model parameters. All terms are defined in Tables 1 and 2 and described in the text. In both diagrams blue ovals show burial fluxes of organic carbon and pyrite sulphur, which are the long term sources of free oxygen.

[Print version should be in colour.]

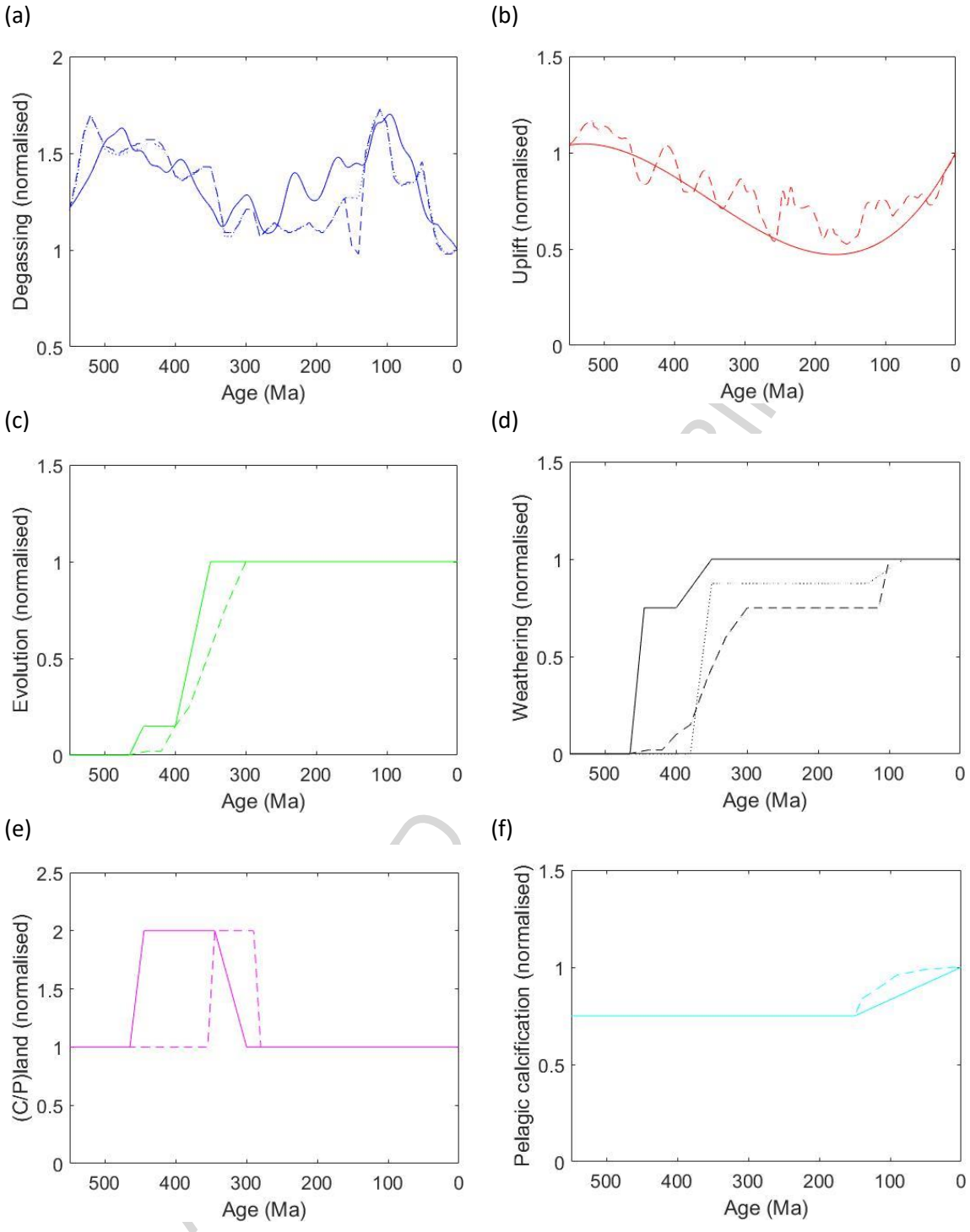

Figure 3. Updating the original forcing factors: (a) degassing, *D* (blue), (b) uplift, *U* (red), (c) plant evolution, *E* (green), (d) plant effects on weathering, *W* (black), (e) plant stoichiometry, CP_{land} (magenta), (f) pelagic calcification, *B* (cyan). Original COPSE (dashed), revised COPSE (solid), GEOCARBSULF (dotted).

[Print version should be in colour.]

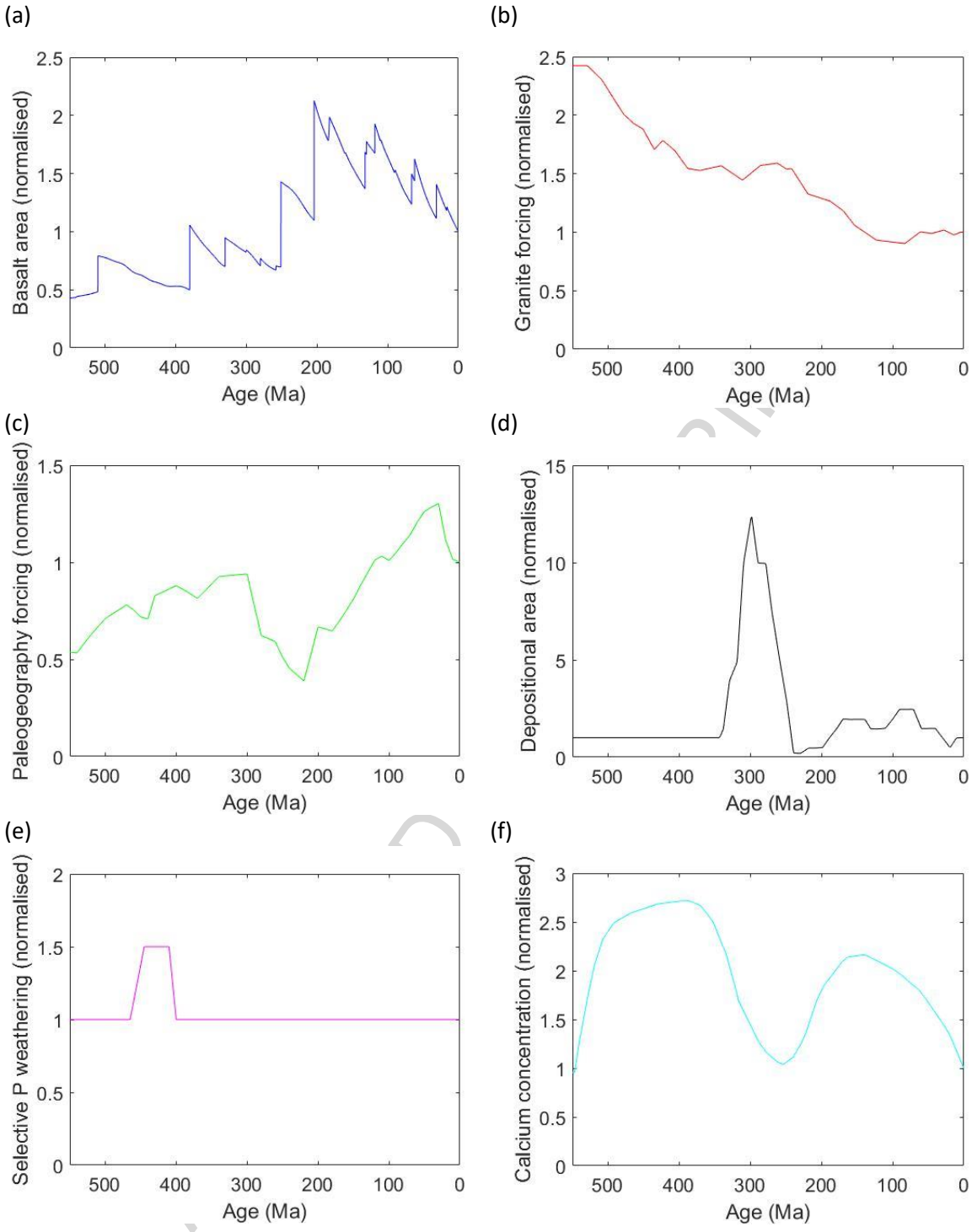

Figure 4. Additional forcing factors: (a) 'basalt' (volcanic silicate rock) area, a_{bas} (blue), (b) 'granite' (non-volcanic silicate rock) kinetically-weighted area, a_{gran} (red), (c) paleogeography forcing of runoff, *PG* (green), (d) coal basins depositional area, b_{coal} (black) , (e) selective weathering of phosphorus, *F* (magenta), (f) calcium concentration, c_{cal} (cyan).

[Print version should be in colour.]

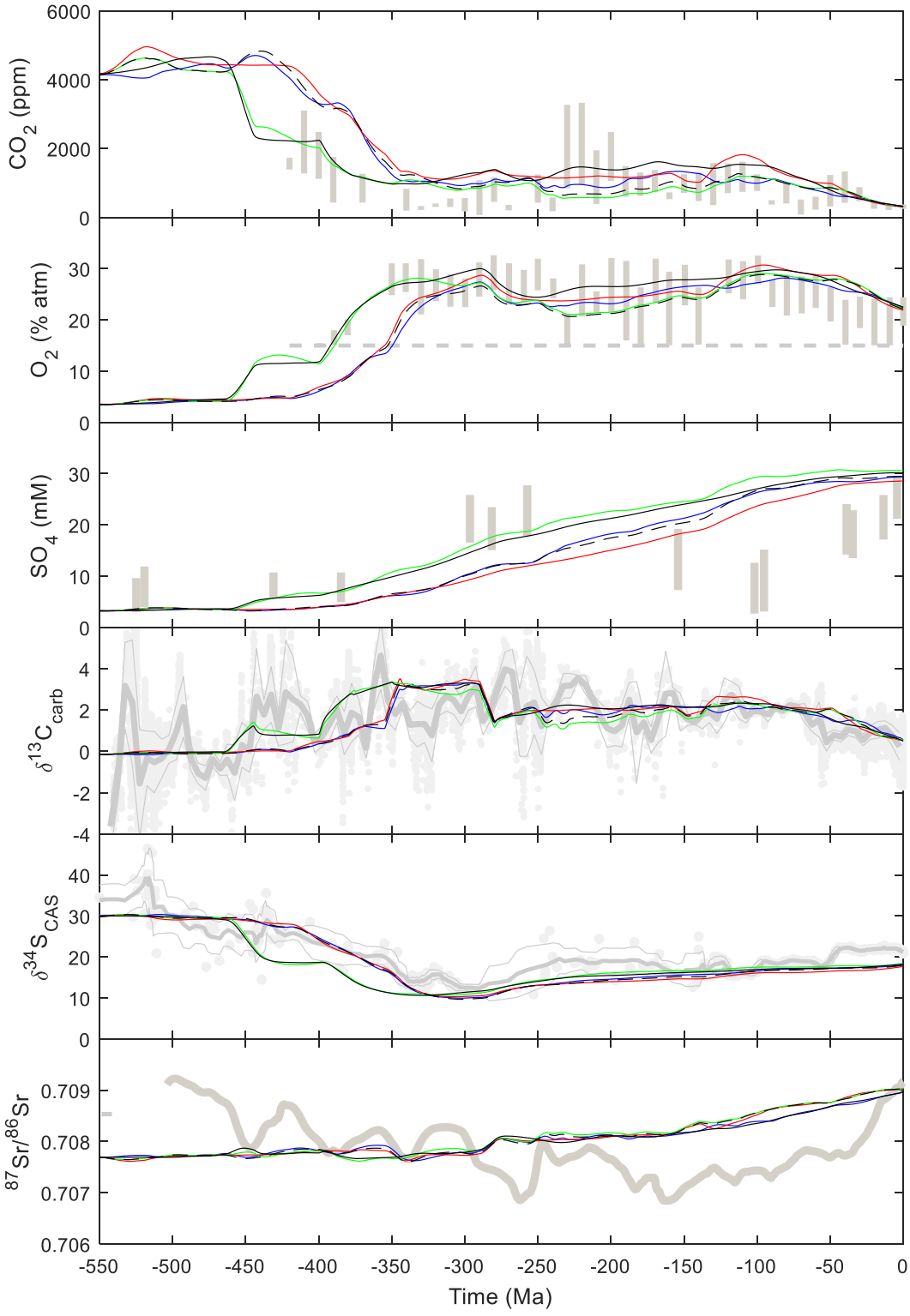

Figure 5: Effect of updating the original forcing factors on predictions of CO_2, O_2, SO_4, $\delta^{13}C$, $\delta^{34}S$, $^{87}Sr/^{86}Sr$. Original model (black dashed) with updates to forcing factors: *D* and *B* (blue), *U* (red), *E*, *W* and CP_{land} (green), and all combined (black). Predictions are compared to proxy data in grey (detailed in Table 6); vertical bars for CO_2, O_2, SO_4 are binned data with uncertainty ranges, grey dashed line for O_2 is lower limit consistent with charcoal evidence of combustion, dots for $\delta^{13}C_{carb}$ and $\delta^{34}S_{CAS}$ are original data, with running mean (bold line) +/- 1 s.d. (thin lines). *[Print version should be in colour.]*

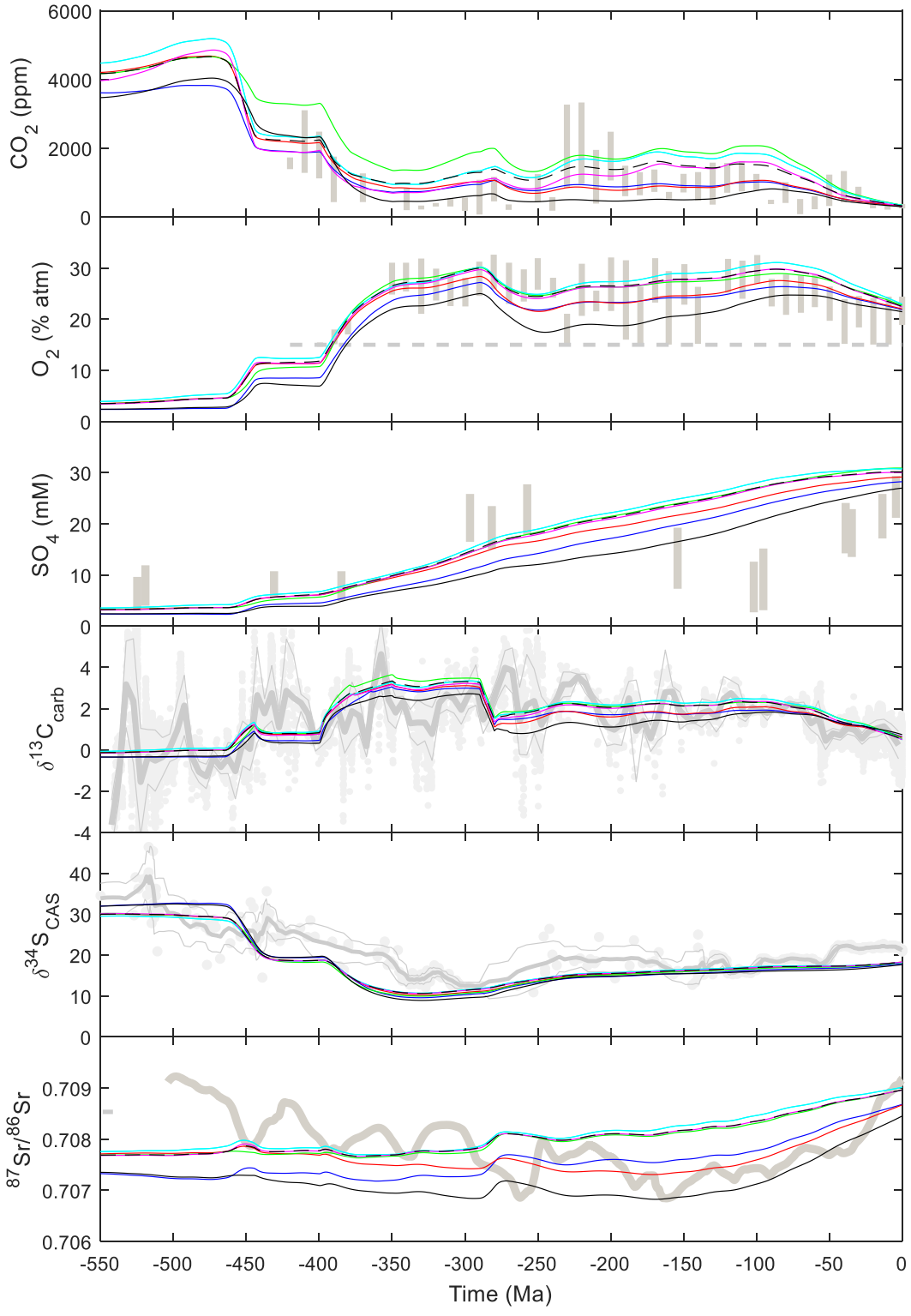

Figure 6: Effects of updating weathering controls on predictions of CO_2, O_2, SO_4, $\delta^{13}C$, $\delta^{34}S$, $^{87}Sr/^{86}Sr$. Starting from the original model with updated forcing of *D*, *U*, *E*, *W*, *B*, CP_{land} (black dashed), with individual additions of: seafloor weathering (blue), making basalt weathering independent of uplift (red), distinguishing different activation energies for basalt and granite weathering (cyan), new vegetation dependence of weathering (green), new temperature function (magenta), and combining all these changes (black). *[Print version should be in colour.]*

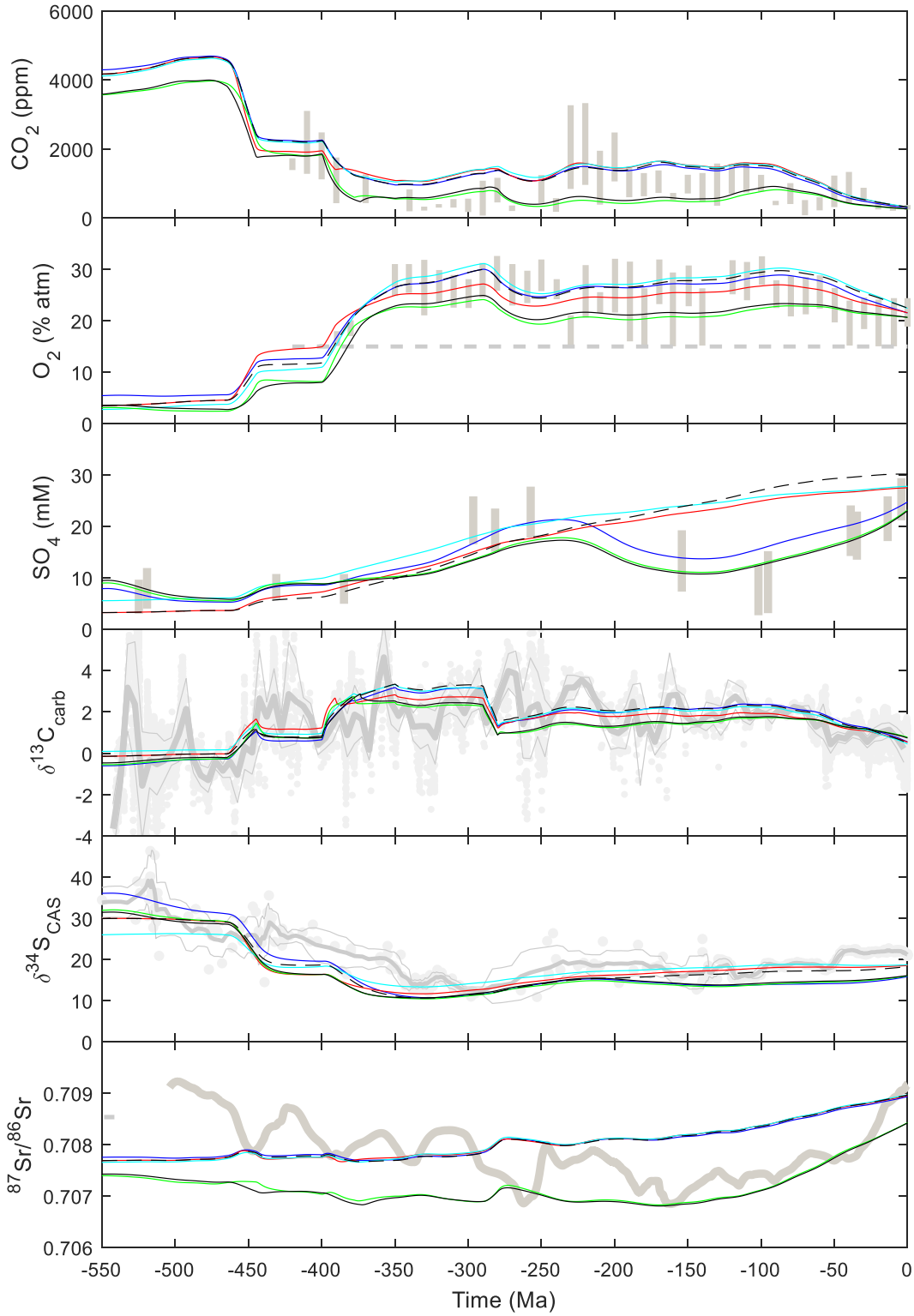

Figure 7: Effects of updating redox controls and combining changes to the baseline model on predictions of CO_2, O_2, SO_4, $\delta^{13}C$, $\delta^{34}S$, $^{87}Sr/^{86}Sr$. Starting from the original model with updated forcing of *D*, *U*, *E*, *W*, *B*, CP_{land} (black dashed), with individual additions of: replacing the interactive Ca cycle with prescribed [Ca], c_{cal} (blue), new fire feedback on vegetation (red), removing the O_2 dependence of pyrite weathering (cyan), combining all these changes with weathering function updates (green), additionally including all other changes to the baseline model (black). *[Print version should be in colour.]*

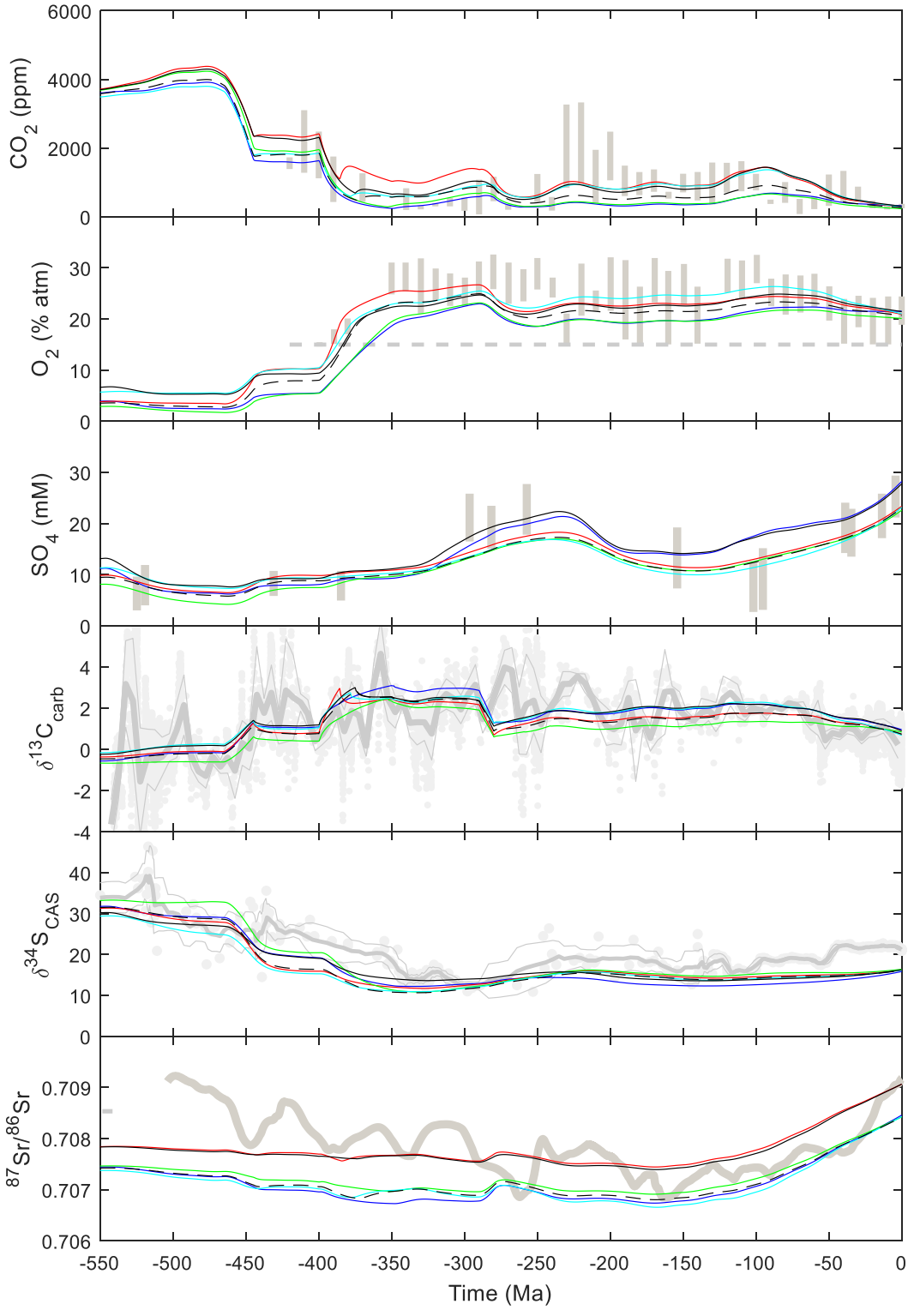

Figure 8: Effects of updating the baseline fluxes on predictions of CO_2, O_2, SO_4, $\delta^{13}C$, $\delta^{34}S$, $^{87}Sr/^{86}Sr$. Starting from the new baseline model with updated forcing of *D*, *U*, *E*, *W*, *B*, CP_{land} (black dashed), with individual variants from it: high S fluxes (blue), high C inorganic fluxes (red), low C organic fluxes (green), revised split of P weathering (cyan), and combination of all these flux updates with revised split of P burial fluxes (black). *[Print version should be in colour.]*

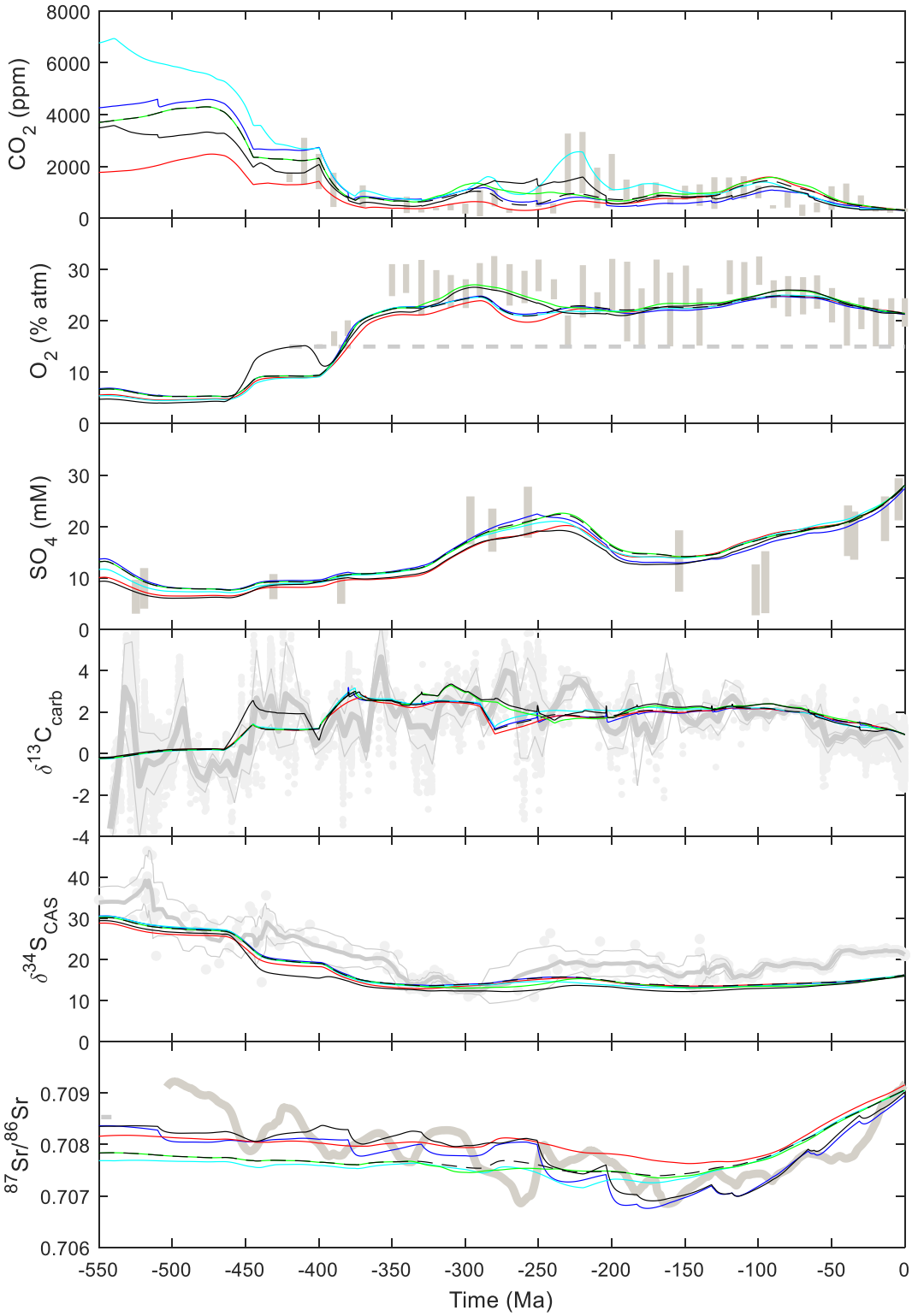

Figure 9: Effects of new forcing factors on predictions of CO_2, O_2, SO_4, $\delta^{13}C$, $\delta^{34}S$, $^{87}Sr/^{86}Sr$. Starting from the new baseline model with updated forcing of *D*, *U*, *E*, *W*, *B*, CP_{land} and updated fluxes (black dashed), with individual forcing factors: basalt area, a_{bas} (blue), granite area, a_{gran} (red), paleogeography, *PG* (cyan), coal basin depositional area, b_{coal}, with adjustment of CP_{land} (green), all of the preceding combined with selective weathering of phosphorus, *F* (black). *[Print version should be in colour.]*

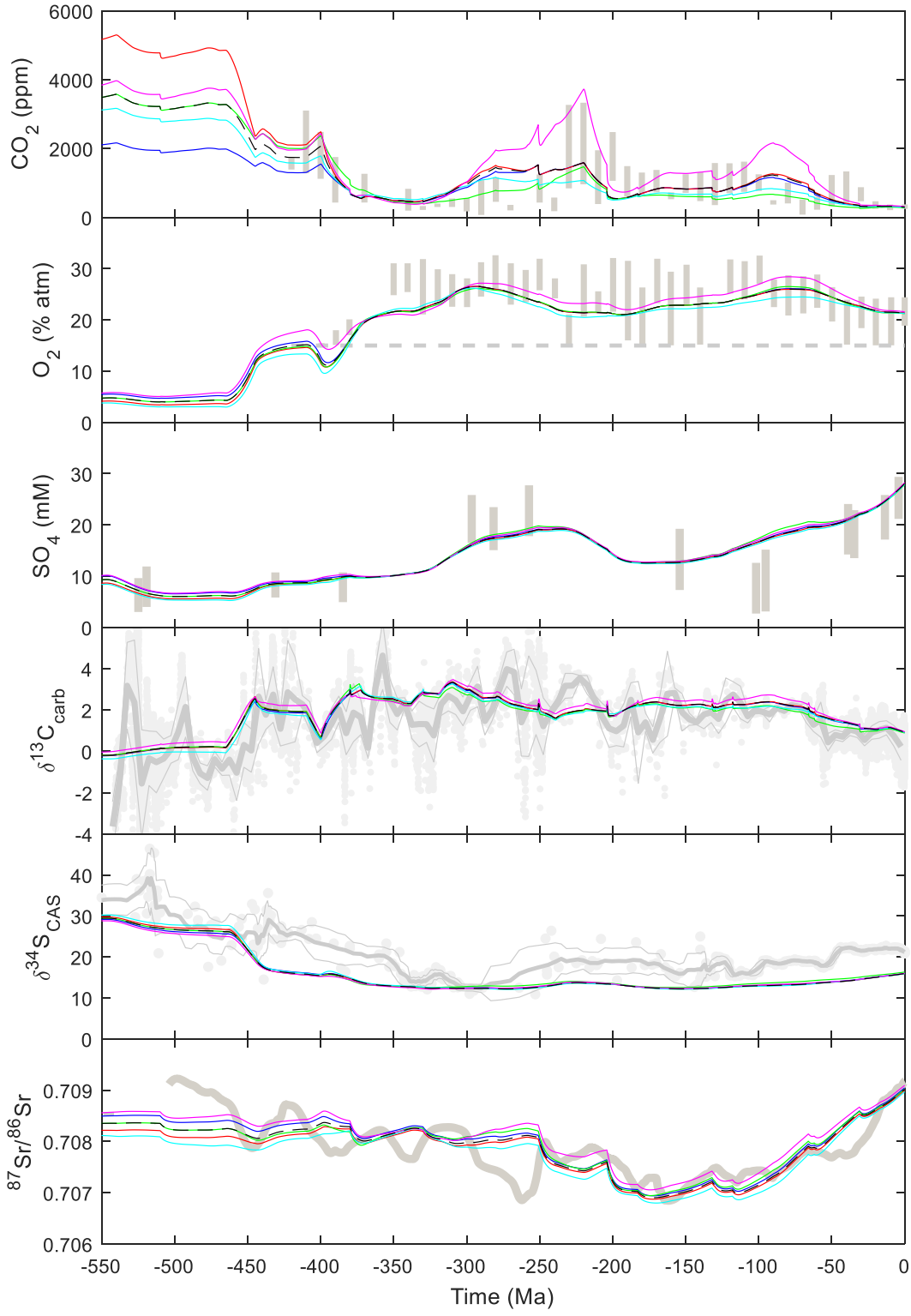

Figure 10: Testing hypotheses for controls on weathering. Starting from the new baseline model with updated original forcing factors, updated fluxes, and new forcing factors (black dashed), with: 4-fold amplification of weathering by plants (k_{15} = 0.25) (blue), 10-fold amplification of weathering by plants (k_{15} = 0.1) (red), weathering dependent on vegetation NPP (rather than biomass) (green), stronger temperature sensitivity of seafloor weathering (cyan), no temperature sensitivity of seafloor weathering (magenta). *[Print version should be in colour.]*

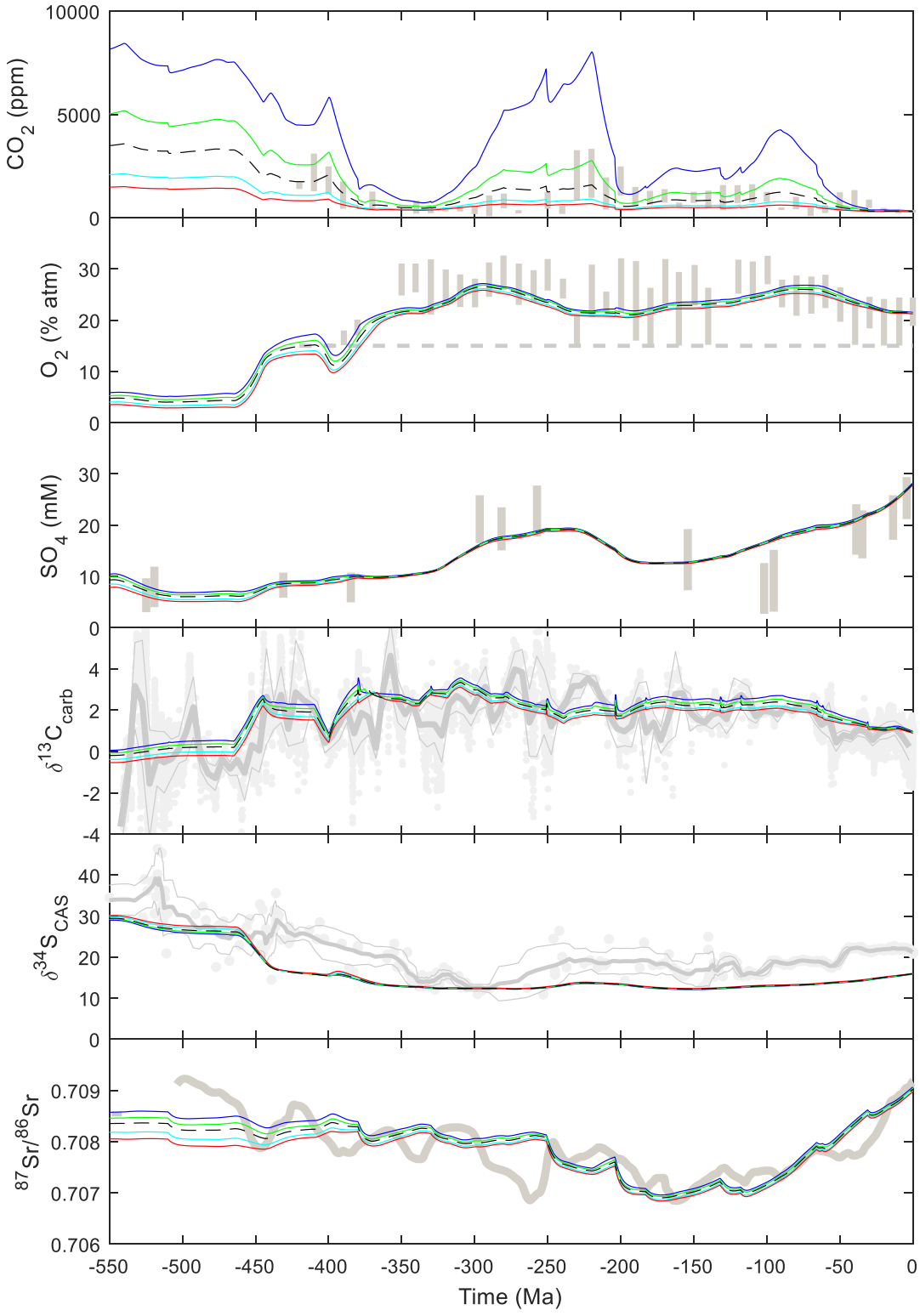

Figure 11. The effect of varying climate sensitivity. Starting from the new baseline model with updated original forcing factors, updated fluxes, and new forcing factors, and varying the climate sensitivity from the default 3°C (black dashed) to: 1.5°C (blue), 2.25°C (green), 4.5°C (cyan), 6°C (red). *[Print version should be in colour.]*

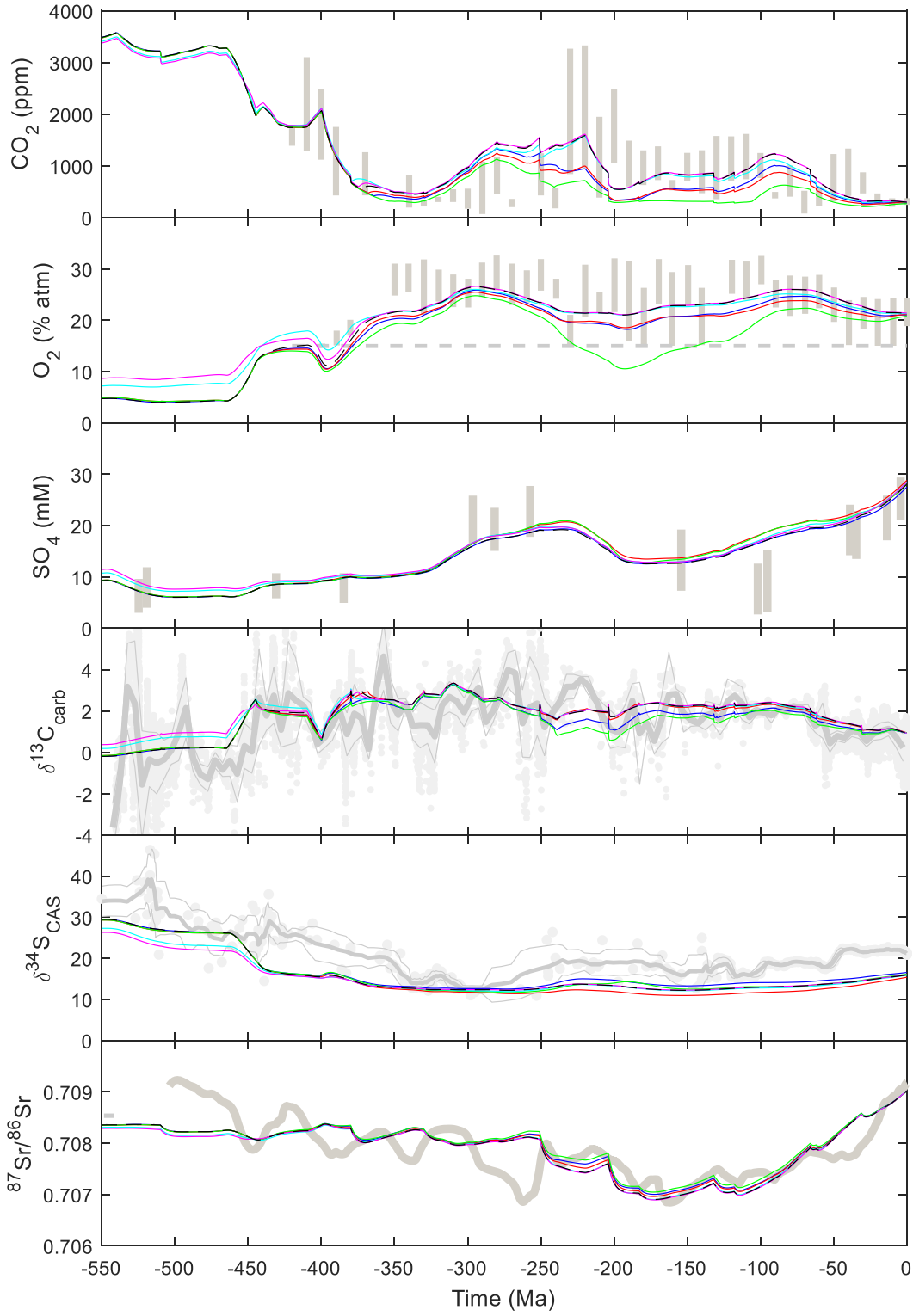

Figure 12: Testing hypotheses for controls on O_2. Starting from the new baseline model with updated original forcing factors, updated fluxes, and new forcing factors (black dashed), with: land-derived organic carbon burial dependent on uplift (blue), marine organic carbon burial dependent on uplift (red), land-derived and marine organic carbon burial dependent on uplift (green), marine organic carbon burial dependent on O_2 (cyan), marine $(C/P)_{organic}$ increasing with anoxia (magenta). *[Print version should be in colour.]*

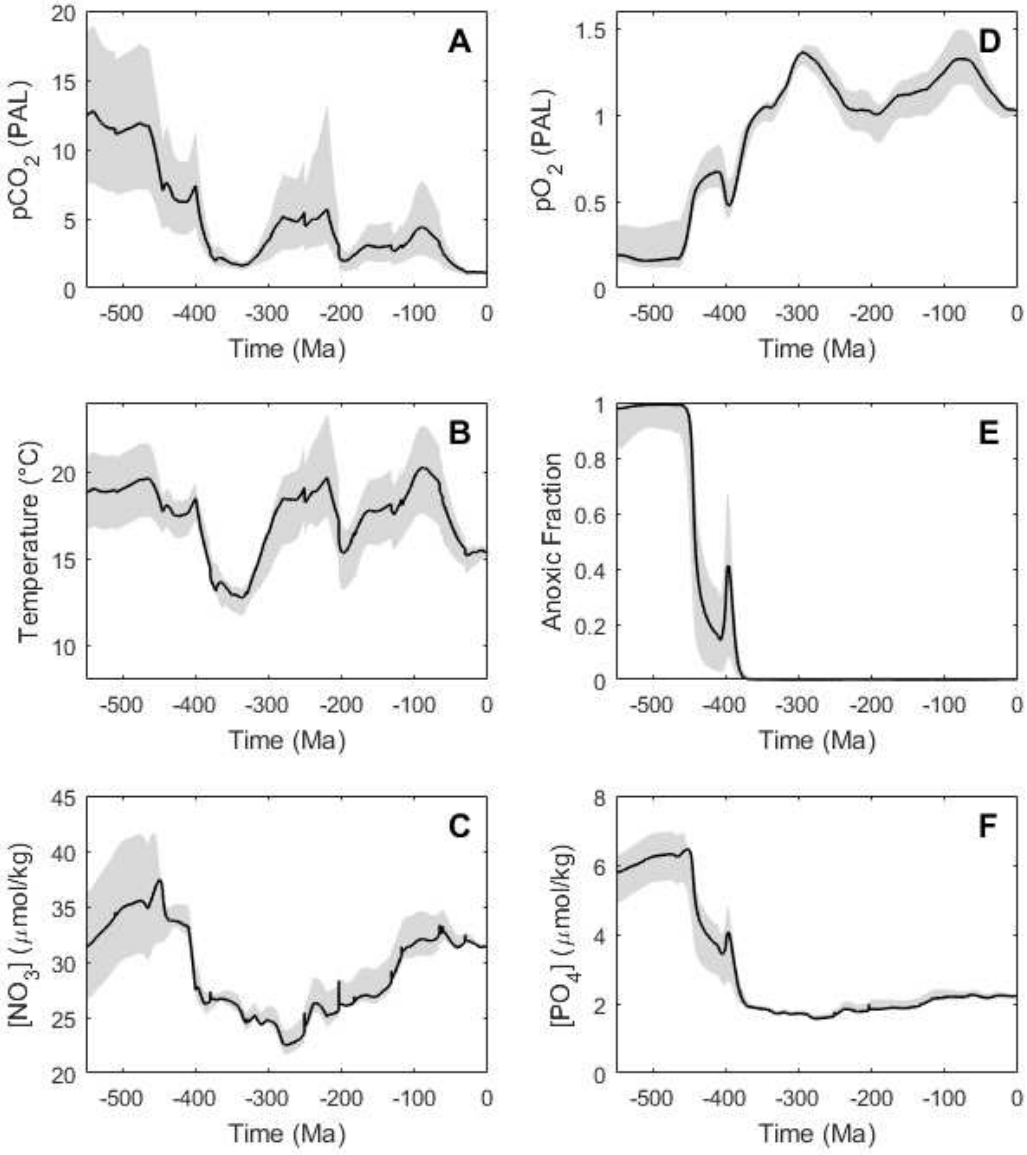

Figure 13. New best guess model and uncertainty range from testing alternative hypotheses. The uncertainty range (in grey) spans all of the hypothesis tests in Section 3.6 and Figures 10-12, with the exception of climate sensitivities of 1.5°C and 6°C, and the combined uplift forcing of marine and terrestrial organic carbon burial – because we consider these cases falsified by that analysis: (A) atmospheric pCO_2, (B) global temperature, (C) ocean nitrate concentration, (D) atmospheric pO_2, (E) anoxic fraction of the ocean, (F) ocean phosphate concentration.

Tables

Table 1. Core COPSE model reservoirs and differential equations.

Reservoir	Label	Differential equation	Initial size (mol)
Ocean (reactive) nitrogen	***N***	$\frac{d\boldsymbol{N}}{dt} = nfix - denit - monb$	4.35×10^{16}
Ocean (phosphate) phosphorus	***P***	$\frac{d\boldsymbol{P}}{dt} = psea - mopb - fepb - capb$	3.1×10^{15}
Atmosphere-ocean O_2	***O***	$\frac{d\boldsymbol{O}}{dt} = locb + mocb - oxidw - ocdeg + 2 \cdot mpsb - 2 \cdot pyrw - 2 \cdot pyrdeg$	3.7×10^{19}
Atmosphere-ocean CO_2	***A***	$\frac{d\boldsymbol{A}}{dt} = oxidw + ocdeg + carbw + ccdeg - locb - mocb - mccb - sfw$	3.193×10^{18}
Sedimentary organic (reduced) carbon	***G***	$\frac{d\boldsymbol{G}}{dt} = locb + mocb - oxidw - ocdeg$	1.25×10^{21}
Sedimentary carbonate (oxidised) carbon	***C***	$\frac{d\boldsymbol{C}}{dt} = mccb + sfw - carbw - ccdeg$	5.0×10^{21}
Ocean (sulphate) sulphur	***S***	$\frac{d\boldsymbol{S}}{dt} = gypw + pyrw + gypdeg + pyrdeg - mgsb - mpsb$	4.0×10^{19}
Sedimentary pyrite (reduced) sulphur	***PYR***	$\frac{d\boldsymbol{PYR}}{dt} = mpsb - pyrw - pyrdeg$	1.8×10^{20}
Sedimentary gypsum (oxidised) sulphur	***GYP***	$\frac{d\boldsymbol{GYP}}{dt} = mgsb - gypw - gypdeg$	2.0×10^{20}

Table 2. Core COPSE model fluxes and baseline values. ('Original' = Bergman et al., 2004, 'G^3' = Mills et al., 2014a, 'New' = new baseline arrived at here.)

Process	Label	Constant	Original	G^3	lowS	highS	lowC_{in}	highC_{in}	lowC_{org}	highC_{org}	New	Notes
Nitrogen cycle			**10^{12} molN yr^{-1}**									
Nitrogen fixation	*nfix*	k_3	8.72						(8.67)		8.67	
Denitrification	*denit*	$2k_4$	8.6								8.6	
Marine organic N burial	*monb*	k_2/CN_{sea}	0.12						(0.07)		0.07	CN_{sea}=37.5
Phosphorus cycle			**10^{9} molP yr^{-1}**									
Reactive P weathering	*phosw*	k_{10}	43.5						(33.5)		42.5	
Terrestrial organic P burial	*pland*	$k_{11}k_{10}$	4.5						(2.5)		2.5	CP_{land}=1000
Reactive P to ocean	*psea*	$(1-k_{11})k_{10}$	39						(31)		40	
Marine organic P burial	*mopb*	k_2/CP_{sea}	18						(10)		10	CP_{sea}=250
Iron-sorbed (Fe-P) burial	*fepb*	k_6	6								10	
Ca-bound (Ca-P) burial	*capb*	k_7	15								20	
Carbon cycle (inorganic)			**10^{12} molC yr^{-1}**									
Carbonate C degassing	*ccdeg*	k_{12}	6.65	6.65			6.65	15			15	
Carbonate weathering	*carbw*	k_{14}	13.35	13.35			13.35	8			8	
Silicate weathering	*silw*	k_{silw}	6.65	4.9			4.9	12			12	
Granite weathering	*granw*	k_{granw}		3.185			3.185	9			9	
Basalt weathering	*basw*	k_{basw}		1.715			1.715	3			3	
Seafloor weathering	*sfw*	k_{sfw}	0	1.75			1.75	3			3	
Carbonate burial	*mccb*	$k_{14}+k_{silw}$	20	18.25			18.25	20			20	
Carbon cycle (organic)			**10^{12} molC yr^{-1}**									
Organic C degassing	*ocdeg*	k_{13}	1.25						1.25	1.25	1.25	
Oxidative C weathering	*oxidw*	k_{17}	7.75						3.75	7.75	3.75	
Marine organic C burial	*mocb*	k_2	4.5						2.5	4.5	2.5	
Terrestrial organic C burial	*locb*	k_5	4.5						2.5	4.5	2.5	
Sulphur cycle			**10^{12} molS yr^{-1}**									
Gypsum degassing	*gypdeg*	k_{gypdeg}	0		0	0.5					0.5	
Pyrite degassing	*pyrdeg*	k_{pyrdeg}	0		0	0.25					0.25	
Gypsum weathering	*gypw*	k_{22}	1.0		1.0	2.0					2.0	
Pyrite weathering	*pyrw*	k_{21}	0.53		0.53	0.45					0.45	
Gypsum burial	*mgsb*	k_{mgsb}	1.0		1.0	2.5					2.5	
Pyrite burial	*mpsb*	k_{mpsb}	0.53		0.53	0.7					0.7	

Table 3. Model forcing factors. (All normalised to 1 at present with the exception of insolation.)

Forcing	Description	Basis	Source(s)
Original model forcing factors			
I	Insolation (solar luminosity)	Stellar physics	(Caldeira and Kasting, 1992)
D	Metamorphic and volcanic degassing	Inversion of sea-level curve	(Mills et al., 2017)
U	Tectonic uplift	Sediment accumulation rates	(Berner, 2006b; Ronov, 1993)
E	Plant evolution and land colonisation	Fossil record and model estimates of global net primary productivity	(Lenton et al., 2016), updated here
W	Plant enhancement of weathering	Experimental and field study results	(Lenton et al., 2012), updated here
CP_{land}	C/P burial ratio of terrestrial plant material	Attempt to capture Paleozoic coal deposition	(Lenton et al., 2016), updated here
B	Apportioning of carbonate burial between shallow and deep seas	Fossil record of evolution of planktonic calicifiers	(Berner, 1994)
Additional forcing factors included herein			
a_{bas}	Exposed area of volcanic silicate rocks	Reconstructed area of large igneous provinces (LIPs) and volcanic islands	(Ernst, 2014; Mills et al., 2014a)
a_{gran}	Kinetically-weighted area of non-volcanic silicate rocks	Reconstructed lithology of shield, shale, coal, evaporite	(Bluth and Kump, 1991)
PG	Paleogeography effect on runoff/weathering	Climate model simulations	(Royer et al., 2014)
b_{coal}	Depositional area of coal basins	Coal abundance data	(Bartdorff et al., 2008)
F	Selective biotic weathering of P relative to host rocks	Experimental results	(Lenton et al., 2012, 2016)
c_{cal}	Ocean calcium concentration	Best fit to fluid inclusion data	(Horita et al., 2002)
Further forcing factors experimented with but not included here			
D_{LIP}	Degassing associated with LIP emplacement	Volume of emplaced LIPs	(Ernst, 2014; Mills et al., 2014a)
a_{carb}	Exposed carbonate area	Reconstructed lithology	(Bluth and Kump, 1991)
a_{shale}	Exposed shale area	Reconstructed lithology	(Bluth and Kump, 1991)
a_{org}	Exposed organic (shale + coal) area	Reconstructed lithology	(Bluth and Kump, 1991)
a_{evap}	Exposed evaporite area	Reconstructed lithology	(Bluth and Kump, 1991)
b_{evap}	Depositional area of evaporites	Reconstructed lithology	(Bluth and Kump, 1991)

Table 4. Changes to the baseline COPSE model functional forms

Functional form used in the new baseline model	Original functional form
$CO_2 = \boldsymbol{a}^2$	$CO_2 = \boldsymbol{a}$
$\Delta T = k_c \cdot \ln CO_2 - k_l \cdot t/570$	Complex function from Caldeira and Kasting (1992)
$ignit = min(max(48 \cdot mO_2 - 9.08, 0), 5)$	$ignit = max(586.2 \cdot mO_2 - 122.102, 0)$
$gypdeg = k_{gypdeg} \cdot D \cdot \boldsymbol{gyp}$	-
$pyrdeg = k_{pyrdeg} \cdot D \cdot \boldsymbol{pyr}$	-
$sfw = k_{sfw} \cdot D \cdot e^{k_T^{sfw} \Delta T}$	-
$f_{biota} = \left[(1 - \min(V \cdot W, 1)) \cdot k_{15} \cdot {CO_2}^{0.5} + V \cdot W\right]$	$f_{biota} = \left[{CO_2}^{0.5} \cdot (1 - \min(V \cdot W, 1)) + \min(V \cdot W, 1) \cdot \left(\frac{2\boldsymbol{a}}{1+\boldsymbol{a}}\right)^{0.4}\right] \cdot [k_{15} + (1 - k_{15}) \cdot V \cdot W]$
$granw = k_{granw} \cdot U \cdot PG \cdot a_{gran} \cdot f_{Tgran} \cdot f_{runoff} \cdot f_{biota}$	-
$basw = k_{basw} \cdot PG \cdot a_{bas} \cdot f_{Tbas} \cdot f_{runoff} \cdot f_{biota}$	-
$silw = granw + basw$	$silw = k_{12} \cdot U \cdot f_T \cdot f_{runoff} \cdot f_{biota}$
$carbw = k_{14} \cdot \boldsymbol{C} \cdot U \cdot PG \cdot g_{runoff} \cdot f_{biota}$	$carbw = k_{14} \cdot U \cdot g_{runoff} \cdot f_{biota}$
$gypw = k_{22} \cdot \boldsymbol{gyp} \cdot U \cdot PG \cdot g_{runoff} \cdot f_{biota}$	$gypw = k_{22} \cdot \boldsymbol{gyp} \cdot U \cdot g_{runoff} \cdot f_{biota}$
$pyrw = k_{21} \cdot U \cdot \boldsymbol{pyr}$	$pyrw = k_{21} \cdot U \cdot \boldsymbol{pyr} \cdot \boldsymbol{o}^{0.5}$
$phosw = k_{10} \cdot F \cdot \left(k_{Psilw} \cdot \frac{silw}{k_{silw}} + k_{Pcarbw} \cdot \frac{carbw}{k_{14}} + k_{Poxidw} \cdot \frac{oxidw}{k_{17}}\right)$	$phosw = k_{10} \cdot \left(k_{Psilw} \cdot \frac{silw}{k_{12}} + k_{Pcarbw} \cdot \frac{carbw}{k_{14}} + k_{Poxidw} \cdot \frac{oxidw}{k_{17}}\right)$
$pland = k_{11} \cdot V \cdot phosw \cdot \left(k_{aq} + \left(1 - k_{aq}\right) \cdot b_{coal}\right)$	$pland = k_{11} \cdot V \cdot phosw$
$anox = \frac{1}{1 + e^{-k_{anox}(k_u \cdot newp\prime - \boldsymbol{o})}}$	$anox = max\left(1 - k_1 \cdot \frac{\boldsymbol{o}}{newp\prime}, 0\right)$
$denit = k_4 \left(1 + \frac{anox}{1 - k_1}\right) \cdot \boldsymbol{n}$	$denit = k_4 \left(1 + \frac{anox}{1 - k_1}\right)$
$fepb = \frac{k_6}{k_1} \cdot (1 - anox) \cdot \boldsymbol{p}$	$fepb = \frac{k_6}{k_1} \cdot (1 - anox)$
$mgsb = k_{mgsb} \cdot \boldsymbol{s} \cdot c_{cal}$	$mgsb = k_{mgsb} \cdot \boldsymbol{s} \cdot \boldsymbol{cal}$

Table 5. Changes to the COPSE model non-flux parameters explored herein. (Flux parameters are in Table 2. References and justification for chosen values are given in the text.)

Label	Meaning	Original model	New default value	Options explored
k_1	Present oxic fraction	0.86	0.997527	-
k_{15}	Pre-plant weathering	0.15	0.15	0.1, 0.25
k_{fire}	Fire frequency control	100	3	-
k_c	Climate sensitivity control	N/A	4.328°C	2.164°C, 3.246°C, 6.492°C, 8.656°C
k_l	Luminosity sensitivity control	N/A	7.4°C	-
k_T^{sfw}	Temperature sensitivity of seafloor weathering	N/A	0.0608	0.1332
k_T^{gran}	Temperature sensitivity of granite weathering	0.09	0.0724	-
k_T^{bas}	Temperature sensitivity of basalt weathering	0.09	0.0608	-
k_{Psilw}	Silicates fraction of P weathering	2/12	0.8	-
k_{Pcarbw}	Carbonates fraction of P weathering	5/12	0.14	-
k_{Poxidw}	Oxidative fraction of P weathering	5/12	0.06	-
k_{aq}	Terrestrial organic matter burial fraction in aquatic settings	N/A	0.8	-
k_u	Nutrient utilisation efficiency	N/A	0.5	-
k_{anox}	Sharpness of oxic-anoxic transition	N/A	12	-

Table 6. Proxy data targets to which the model predictions are compared.

Variable	Proxy source(s)	Data aggregation	Data sources
CO_2	Stomatal index, phytoplankton alkenones, liverwort $\delta^{13}C$, paleosol $\delta^{13}C$, boron $\delta^{11}B$, nahcolite	10 Myr bins, +/-1 s.d.	(Royer, 2014)
O_2	Charcoal content of coals, scaled between assumed limits of 15% and 25-35%	10 Myr bins, uncertainty range from uncertain upper limit	(Glasspool and Scott, 2010) lower limit extended to 420 Ma based on (Lenton et al., 2016)
SO_4	Fluid inclusion data only	-	(Algeo et al., 2015; Brennan et al., 2004; Horita et al., 2002; Lowenstein et al., 2005)
$\delta^{13}C$	Carbonates from a range of organisms and depths	5 Myr bins, mean +/-1 s.d.	(Saltzman and Thomas, 2012)
$\delta^{34}S$	Carbonate associated sulphate (CAS)	9 point moving mean +/-1 s.d.	(Algeo et al., 2015; Kampschulte and Strauss, 2004; Paytan et al., 1998)
$^{87}Sr/^{86}Sr$	Conodont apatite	LOWESS V5, plus one bin for data 543-548 Ma	(McArthur et al., 2012), plus 543-548 Ma data from (Cox et al., 2016)

Appendix A: Strontium cycle and its isotopes

A strontium cycle and its isotopes are implemented following Francois and Walker (1992) and Vollstaedt et al. (2014) with some improvements to the formulation described in Mills et al. (2014a). Ocean (*OSr*) and sedimentary carbonate (*SSr*) reservoirs of strontium are considered. The strontium reservoir calculations are summarised in Table A.1, with the fluxes defined and present day baseline values given in Table A.2, and other constants defined in Table A.3. Fluxes of strontium are tied, where possible, to existing model variables via first-order scaling relationships.

The ocean reservoir of strontium (*OSr*) has inputs from the mantle, weathering of old igneous rocks (granites), new igneous rocks (basalts), and sedimentary carbonates, and outputs from incorporation of strontium in (carbonate) sediments and seafloor weathering. Input of strontium to the ocean from the mantle (Sr_{mantle}) is assumed to be proportional to degassing (D):

$$Sr_{mantle} = k_{Srmantle} \cdot D \tag{A.1}$$

Inputs of strontium to the ocean from weathering of basalts (Sr_{basw}) and granites (Sr_{granw}) follows the same apportioning as the corresponding carbon fluxes:

$$Sr_{basw} = k_{Srbasw} \cdot \frac{basw}{k_{basw}} \tag{A.2}$$

$$Sr_{granw} = k_{Srgranw} \cdot \frac{granw}{k_{granw}} \tag{A.3}$$

Input of strontium from carbonate sediments (Sr_{sedw}) is assumed to scale with carbonate weathering and with the concentration of strontium in the sedimentary carbonate reservoir (the latter differs from Mills et al., 2014a):

$$Sr_{sedw} = k_{Srsedw} \cdot \frac{carbw}{k_{carbw}} \cdot \frac{SSr}{SSr_0} \tag{A.4}$$

Removal of strontium through burial in (carbonate) sediments is assumed proportional to the rate of carbonate sediment deposition and the concentration of strontium in the ocean:

$$Sr_{sedb} = k_{Srsedb} \cdot \frac{mccb}{k_{mccb}} \cdot \frac{OSr}{OSr_0} \quad \text{(A.5)}$$

The rate of strontium removal in seafloor weathering is assumed to depend on the seafloor weathering rate and the strontium concentration in the ocean (the latter differs from Mills et al., 2014a):

$$Sr_{sfw} = k_{Srsfw} \cdot \frac{sfw}{k_{sfw}} \cdot \frac{OSr}{OSr_0} \quad \text{(A.6)}$$

The relative proportions of the burial and seafloor weathering removal fluxes of strontium are assumed to follow the same proportions as the corresponding fluxes in the carbon system, with the total flux dictated by assuming present day steady state for oceanic Sr concentration.

The sedimentary reservoir of strontium (*SSr*) has an input from carbonate burial (Sr_{sedb}), and outputs from carbonate weathering (Sr_{sedw}) and metamorphic conversion to crustal rocks (Sr_{metam}). The output from sediment metamorphism is assumed to be proportional to degassing (*D*) and the concentration of strontium in the sedimentary carbonate reservoir (the latter differs from Mills et al., 2014a):

$$Sr_{metam} = k_{Srmetam} \cdot D \cdot \frac{SSr}{SSr_0} \quad \text{(A.7)}$$

Although there is no fractionation of Sr isotopes associated with the input and output fluxes to the ocean, decay of ^{87}Rb to ^{87}Sr influences the ^{87}Sr/^{86}Sr ratio over long timescales (and is responsible for the differing ^{87}Sr/^{86}Sr values between different rock types). The decay process is represented explicitly in the model:

$$^{87}Sr/^{86}Sr_{granite} = {}^{87}Sr/^{86}Sr_0 + {}^{87}Rb/^{86}Sr_{granite}\left(1 - e^{-\lambda t}\right) \quad \text{(A.8)}$$

$$^{87}Sr/^{86}Sr_{basalt} = {}^{87}Sr/^{86}Sr_0 + {}^{87}Rb/^{86}Sr_{basalt}\left(1 - e^{-\lambda t}\right) \quad \text{(A.9)}$$

$$^{87}Sr/^{86}Sr_{mantle} = {}^{87}Sr/^{86}Sr_0 + {}^{87}Rb/^{86}Sr_{mantle}\left(1 - e^{-\lambda t}\right) \quad \text{(A.10)}$$

Where time (t) is in years from Earth formation (taken to be 4.5 billion years ago). For each rock type, the present day rubidium-strontium ratio is then calculated (Table A.3) such that the observed present day $^{87}Sr/^{86}Sr$ ratio is achieved for each rock type after 4.5 billion years:

$$^{87}Rb/^{86}Sr = \frac{\left(^{87}Sr/^{86}Sr_{present} - ^{87}Sr/^{86}Sr_0\right)}{\left(1-e^{-\lambda \cdot 4.5\times10^9}\right)} \quad \text{(A.11)}$$

The isotopic composition of the ocean and the sediments are calculated by first creating reservoirs consisting of Sr concentrations multiplied by their isotopic ratios, where δSr_X denotes the $^{87}Sr/^{86}Sr$ ratio of reservoir *X*:

$$\frac{d(OSr\cdot\delta Sr_{ocean})}{dt} = Sr_{granw}\cdot\delta Sr_{granite} + Sr_{basw}\cdot\delta Sr_{basalt} + Sr_{sedw}\cdot\delta Sr_{sediment} + Sr_{mantle}\cdot \delta Sr_{mantle} - Sr_{sedb}\cdot\delta Sr_{ocean} - Sr_{sfw}\cdot\delta Sr_{ocean} \quad \text{(A.12)}$$

$$\frac{d(SSr\cdot\delta Sr_{sediment})}{dt} = Sr_{sedb}\cdot\delta Sr_{ocean} - Sr_{sedw}\cdot\delta Sr_{sediment} - Sr_{metam}\cdot\delta Sr_{sediment} + SSr\cdot\lambda\cdot\left(^{87}Rb/^{86}Sr_{carbonate}\right)\cdot e^{\lambda(4.5\times10^9-t)} \quad \text{(A.13)}$$

The carbonate sediment isotopic reservoir evolution includes a term to account for rubidium decay within the sedimentary reservoir. The present-day rubidium-strontium ratio of sediments $^{87}Rb/^{86}Sr_{carbonate}$, (Table A.3), is calculated to achieve the average crustal $^{87}Sr/^{86}Sr$ of 0.73 (Veizer and Mackenzie, 2003) .

The ocean and sediment $^{87}Sr/^{86}Sr$ ratios are calculated by dividing the new reservoirs by the known concentration or total:

$$\delta Sr_{ocean} = \frac{OSr\cdot\delta Sr_{ocean}}{OSr} \quad \text{(A.14)}$$

$$\delta Sr_{sediment} = \frac{SSr\cdot\delta Sr_{sediment}}{SSr} \quad \text{(A.15)}$$

Present day fluxes are taken from Francois and Walker (1992) with differences being the split of basalt and granite weathering and the split of seafloor weathering and sediment burial. The present

day fluxes are such that although the ocean reservoir is in steady state, the sedimentary pool of strontium is out of steady state and growing. However, over Phanerozoic time the generally greater than present degassing tends to generate shrinkage of the sedimentary reservoir. This shrinkage is buffered considerably by the assumed dependence of metamorphic conversion on the sedimentary strontium reservoir size. Nevertheless the sedimentary reservoir needs to be initialised larger than present (typically 6×10^{18} mol) at 600 Ma to approach the present day value.

The choice of present day values for $^{87}Sr/^{86}Sr$ of mantle, basalt and granite together with the corresponding input fluxes determine the present day 'attractor' value (a) for the composition of the ocean and sediments, following:

$$a = \left(\frac{k_{Srsilw}}{k_{Srmantle}+k_{Srsilw}}\right) \cdot \left(k_{basfrac} \cdot \delta Sr_{basalt} + \left(1 - k_{basfrac}\right) \cdot \delta Sr_{granite}\right) + \left(\frac{k_{Srmantle}}{k_{Srmantle}+k_{Srsilw}}\right) \cdot \delta Sr_{mantle} \quad \text{(A.16)}$$

Using $k_{basfrac}$=0.25 and the other values from (Francois and Walker, 1992), including $\delta Sr_{granite}$=0.718, gives a=0.7105, whereas the ocean is at ~0.709 and sedimentary carbonates at ~0.708, suggesting some internal inconsistency in that set up. Previously we used $\delta Sr_{granite}$=0.715 (Mills et al., 2014a), which gives a=0.7091, consistent with the present ocean state, and we adopt that value here.

In our previous work (Mills et al., 2014a) sedimentary carbonate was initialised at $\delta Sr_{sediment}$ = 0.714 in order to recover present day values, but this is hard to justify given that Phanerozoic carbonates have ranged over 0.7065-0.709 and the Neoproterozoic saw a major rise from ~0.706 to ~0.709 (Halverson et al., 2007). The use of a high initial sedimentary $^{87}Sr/^{86}Sr$ tends to drag up the initial ocean $^{87}Sr/^{86}Sr$, but without evidence for such high values here instead we initialise with $\delta Sr_{sediment}$ = 0.708, which is roughly the Phanerozoic average and a reasonable value for the late Neoproterozoic.

Table A.1. Strontium reservoirs and differential equations.

Reservoir	Label	Differential equation	Present size (mol)
Ocean Sr	OSr	$\frac{dOSr}{dt} = Sr_{granw} + Sr_{basw} + Sr_{sedw} + Sr_{mantle} - Sr_{sedb} - Sr_{sfw}$	1.2×10^{17}
Sed. Sr	SSr	$\frac{dSSr}{dt} = Sr_{sedb} - Sr_{sedw} - Sr_{metam}$	5×10^{18}

Table A.2. Strontium fluxes and baseline (present day) values.

Process	Label	Constant	Baseline flux (molSr yr^{-1})	Source/Notes
(Silicate weathering)		k_{Srsilw}	13×10^{9}	(Francois and Walker, 1992)
Basalt weathering	Sr_{basw}	$k_{basfrac} \cdot k_{Srsilw}$		split follows carbon cycle
Granite weathering	Sr_{granw}	$(1-k_{basfrac}) \cdot k_{Srsilw}$		split follows carbon cycle
Sediment weathering	Sr_{sedw}	k_{Srsedw}	17×10^{9}	(Francois and Walker, 1992)
Mantle input	Sr_{mantle}	$k_{Srmantle}$	7.3×10^{9}	(Francois and Walker, 1992)
Seafloor weathering	Sr_{sfw}	k_{Srsfw}		split follows carbon cycle
Sediment burial	Sr_{sedb}	k_{Srsedb}		split follows carbon cycle
Sediment metamorphism	Sr_{metam}	$k_{Srmetam}$	13×10^{9}	(Francois and Walker, 1992)

Table A.3. Other constants in the strontium cycle.

Constant	Label	Value	Source/Notes
^{87}Rb decay rate	λ	1.4×10^{-11} yr^{-1}	(Francois and Walker, 1992)
Original value	$^{87}Sr/^{86}Sr_0$	0.69898	at formation of the Earth
^{87}Sr/^{86}Sr basalt	δSr_{basalt}	0.705	(Francois and Walker, 1992)
^{87}Sr/^{86}Sr granite	$\delta Sr_{granite}$	0.715	reproduces present ocean composition
^{87}Sr/^{86}Sr mantle	δSr_{mantle}	0.703	(Francois and Walker, 1992)
^{87}Rb/^{86}Sr mantle	$^{87}Rb/^{86}Sr_{mantle}$	0.066	for correct present day ^{87}Sr/^{86}Sr
^{87}Rb/^{86}Sr basalt	$^{87}Rb/^{86}Sr_{basalt}$	0.1	for correct present day ^{87}Sr/^{86}Sr
^{87}Rb/^{86}Sr granite	$^{87}Rb/^{86}Sr_{granite}$	0.26	for correct present day ^{87}Sr/^{86}Sr
^{87}Rb/^{86}Sr sediments	$^{87}Rb/^{86}Sr_{carbonate}$	0.5	for correct present day ^{87}Sr/^{86}Sr assuming crustal average ^{87}Sr/^{86}Sr of 0.73

References

Algeo, T.J., Luo, G.M., Song, H.Y., Lyons, T.W. and Canfield, D.E., 2015. Reconstruction of secular variation in seawater sulfate concentrations. Biogeosciences, 12(7): 2131-2151.

Algeo, T.J. and Scheckler, S.E., 1998. Terrestrial-marine teleconnections in the Devonian: links between the evolution of land plants, weathering processes, and marine anoxic events. Philosophical Transactions of the Royal Society of London, Series B, 353(1365): 113-130.

Allegre, C.J., Louvat, P., Gaillardet, J., Meynadier, L., Rad, S. and Capmas, F., 2010. The fundamental role of island arc weathering in the oceanic Sr isotope budget. Earth and Planetary Science Letters, 292(1-2): 51-56.

Alt, J.C. and Teagle, D.A.H., 1999. The uptake of carbon during alteration of ocean crust. Geochimica et Cosmochimica Acta, 63(10): 1527-1535.

Amiotte-Suchet, P., Probst, J.-L. and Ludwig, W., 2003. Worldwide distribution of continental rock lithology: Implications for the atmospheric/soil CO2 uptake by continental weathering and alkalinity river transport to the oceans. Global Biogeochemical Cycles, 17(2): 1038.

Andrews, M.Y., Ague, J.J. and Berner, R.A., 2008. Weathering of soil minerals by angiosperm and gymnosperm trees. Mineralogical Magazine, 72(1): 11-14.

Arvidson, R.S., Guidry, M.W. and Mackenzie, F.T., 2011. Dolomite Controls on Phanerozoic Seawater Chemistry. Aquatic Geochemistry, 17(4): 735-747.

Arvidson, R.S., Mackenzie, F.T. and Berner, R.A., 2014. The Sensitivity of the Phanerozoic Inorganic Carbon System to the Onset of Pelagic Sedimentation. Aquatic Geochemistry, 20(2): 343-362.

Arvidson, R.S., Mackenzie, F.T. and Guidry, M., 2006. MAGic: A Phanerozoic Model for the Geochemical Cycling of Major Rock-Forming Components. American Journal of Science, 306(3): 135-190.

Arvidson, R.S., Mackenzie, F.T. and Guidry, M.W., 2013. Geologic history of seawater: A MAGic approach to carbon chemistry and ocean ventilation. Chemical Geology, 362: 287-304.

Bartdorff, O., Wallmann, K., Latif, M. and Semenov, V., 2008. Phanerozoic evolution of atmospheric methane. Global Biogeochemical Cycles, 22(1): GB1008.

Belcher, C.M. and McElwain, J.C., 2008. Limits for Combustion in Low O2 Redefine Paleoatmospheric Predictions for the Mesozoic. Science, 321(5893): 1197-1200.

Belcher, C.M., Yearsley, J.M., Hadden, R.M., McElwain, J.C. and Rein, G., 2010. Baseline intrinsic flammability of Earth's ecosystems estimated from paleoatmospheric oxygen over the past 350 million years. Proceedings of the National Academy of Sciences, 107(52): 22448-22453.

Bergman, N.M., Lenton, T.M. and Watson, A.J., 2004. COPSE: a new model of biogeochemical cycling over Phanerozoic time. Am. J. Sci., 304: 397-437.

Berner, R.A., 1987. Models for carbon and sulfur cycles and atmospheric oxygen: Application to Paleozoic geologic history. American Journal of Science, 287: 177-196.

Berner, R.A., 1989. Biogeochemical cycles of carbon and sulfur and their effect on atmospheric oxygen over Phanerozoic time. Global and Planetary Change, 75: 97-122.

Berner, R.A., 1991. A model for atmospheric CO2 over Phanerozoic time. American Journal of Science, 291: 339-376.

Berner, R.A., 1994. Geocarb II: A revised model of atmospheric CO2 over Phanerozoic time. American Journal of Science, 294: 56-91.

Berner, R.A., 2006a. GEOCARBSULF: A combined model for Phanerozoic atmospheric O2 and CO2. Geochimica et Cosmochimica Acta, 70(23): 5653-5664.

Berner, R.A., 2006b. Inclusion of the Weathering of Volcanic Rocks in the GEOCARBSULF Model. American Journal of Science, 306(5): 295-302.

Berner, R.A., 2009. Phanerozoic atmospheric oxygen: New results using the GEOCARBSULF model. Am J Sci, 309(7): 603-606.

Berner, R.A. and Canfield, D.E., 1989. A new model for atmospheric oxygen over Phanerozoic time. American Journal of Science, 289: 333-361.

Berner, R.A. and Kothavala, Z., 2001. Geocarb III: A revised model of atmospheric CO2 over Phanerozoic time. American Journal of Science, 301: 182-204.

Berner, R.A., Lasaga, A.C. and Garrels, R.M., 1983. The carbonate-silicate geochemical cycle and its effect on atmospheric carbon dioxide over the past 100 million years. American Journal of Science, 283: 641-683.

Berner, R.A., Petsch, S.T., Lake, J.A., Beerling, D.J., Popp, B.N., Lane, R.S., Laws, E.A., Westley, M.B., Cassar, N., Woodward, F.I. and Quick, W.P., 2000. Isotope Fractionation and Atmospheric Oxygen: Implications for Phanerozoic O2 Evolution. Science, 287: 1630-1633.

Berner, R.A., VandenBrooks, J.M. and Ward, P.D., 2007. Oxygen and Evolution. Science, 316(5824): 557-558.

Betts, J.N. and Holland, H.D., 1991. The oxygen content of ocean bottom waters, the burial efficiency of organic carbon, and the regulation of atmospheric oxygen. Palaeogeography, Palaeoclimatology, Palaeoecology (Global and Planetary Change Section), 97: 5-18.

Blair, N.E. and Aller, R.C., 2012. The Fate of Terrestrial Organic Carbon in the Marine Environment. Annual Review of Marine Science, 4(1): 401-423.

Bluth, G.J.S. and Kump, L.R., 1991. Phanerozoic paleogeology. American Journal of Science, 291(3): 284-308.

Bond, W.J., Woodward, F.I. and Midgley, G.F., 2005. The global distribution of ecosystems in a world without fire. New Phytologist, 165: 525-538.

Brennan, S.T., Lowenstein, T.K. and Horita, J., 2004. Seawater chemistry and the advent of biocalcification. Geology, 32(6): 473-476.

Burdige, D.J., 2005. Burial of terrestrial organic matter in marine sediments: A re-assessment. Global Biogeochemical Cycles, 19(4): GB4011.

Caldeira, K. and Kasting, J.F., 1992. The life span of the biosphere revisited. Nature, 360: 721-723.

Canfield, D.E., 1998. A new model for Proterozoic ocean chemistry. Nature, 396: 450-453.

Canfield, D.E., 2013. Sulfur isotopes in coal constrain the evolution of the Phanerozoic sulfur cycle. Proceedings of the National Academy of Sciences, 110(21): 8443-8446.

Caves, J.K., Jost, A.B., Lau, K.V. and Maher, K., 2016. Cenozoic carbon cycle imbalances and a variable weathering feedback. Earth and Planetary Science Letters, 450: 152-163.

Cohen, K.M., Finney, S.C., Gibbard, P.L. and Fan, J.-X., 2013; updated. The ICS International Chronostratigraphic Chart. Episodes, 36: 199-204.

Compton, J., Mallinson, D., Glenn, C.R., Filippelli, G., Follmi, K., Shields, G. and Zanin, Y., 2000. Variations in the global phosphorus cycle. In: C.R. Glenn, L. Prevot-Lucas and J. Lucas (Editors), Marine Authigenesis: From Global to Microbial, SEPM Special Publication No. 66. SEPM (Society for Sedimentary Geology), pp. 21-33.

Coogan, L.A. and Dosso, S.E., 2015. Alteration of ocean crust provides a strong temperature dependent feedback on the geological carbon cycle and is a primary driver of the Sr-isotopic composition of seawater. Earth and Planetary Science Letters, 415: 38-46.

Cox, G.M., Halverson, G.P., Stevenson, R.K., Vokaty, M., Poirier, A., Kunzmann, M., Li, Z.-X., Denyszyn, S.W., Strauss, J.V. and Macdonald, F.A., 2016. Continental flood basalt weathering as a trigger for Neoproterozoic Snowball Earth. Earth and Planetary Science Letters, 446: 89-99.

Daines, S.J., Mills, B. and Lenton, T.M., 2017. Atmospheric oxygen regulation at low Proterozoic levels by incomplete oxidative weathering of sedimentary organic carbon. Nature Communications, 8: 14379.

Dessert, C., Dupré, B., Gaillardet, J., François, L.M. and Allègre, C.J., 2003. Basalt weathering laws and the impact of basalt weathering on the global carbon cycle. Chemical Geology, 202(3-4): 257-273.

Donnadieu, Y., Goddéris, Y., Pierrehumbert, R., Dromart, G., Fluteau, F. and Jacob, R., 2006. A GEOCLIM simulation of climatic and biogeochemical consequences of Pangea breakup. Geochemistry, Geophysics, Geosystems, 7(11): Q11019.

Edwards, D., Cherns, L. and Raven, J.A., 2015. Could land-based early photosynthesizing ecosystems have bioengineered the planet in mid-Palaeozoic times? Palaeontology, 58(5): 803-837.

Engebretson, D.C., Kelley, K.P., Cashman, H.J. and Richards, M.A., 1992. 180 Million Years of Subduction. GSA Today, 2(5): 93-100.

Ernst, R.E., 2014. Large Igneous Provinces. Cambridge University Press, Cambridge, UK.

Falkowski, P.G., Katz, M.E., Milligan, A.J., Fennel, K., Cramer, B.S., Aubry, M.P., Berner, R.A., Novacek, M.J. and Zapol, W.M., 2005. The Rise of Oxygen over the Past 205 Million Years and the Evolution of Large Placental Mammals. Science, 309: 2202-2204.

Francois, L.M. and Walker, J.C.G., 1992. Modelling the Phanerozoic carbon cycle and climate: Constraints from the $^{87}Sr/^{86}Sr$ isotopic ratio of seawater. American Journal of Science, 292: 81-135.

Gaffin, S., 1987. Ridge volume dependence on seafloor generation rate and inversion using long term sealevel change. American Journal of Science, 287(6): 596-611.

Gaillardet, J., Dupré, B., Louvat, P. and Allègre, C.J., 1999. Global silicate weathering and CO2 consumption rates deduced from the chemistry of large rivers. Chemical Geology, 159(1–4): 3-30.

Galy, V., Peucker-Ehrenbrink, B. and Eglinton, T., 2015. Global carbon export from the terrestrial biosphere controlled by erosion. Nature, 521(7551): 204-207.

Garrels, R.M. and Lerman, A., 1981. Phanerozoic cycles of sedimentary carbon and sulfur. Proceedings of the National Academy of Sciences USA, 78(8): 4652-4656.

Garrels, R.M. and Lerman, A., 1984. Coupling of the sedimentary sulfur and carbon cycles; an improved model. American Journal of Science, 284(9): 989-1007.

Gillis, K.M. and Coogan, L.A., 2011. Secular variation in carbon uptake into the ocean crust. Earth and Planetary Science Letters, 302(3–4): 385-392.

Glasspool, I.J., Edwards, D. and Axe, L., 2004. Charcoal in the Silurian as evidence for the earliest wildfire. Geology, 32(5): 381-383.

Glasspool, I.J. and Scott, A.C., 2010. Phanerozoic concentrations of atmospheric oxygen reconstructed from sedimentary charcoal. Nature Geosci, 3(9): 627-630.

Goddéris, Y., Donnadieu, Y., Le Hir, G., Lefebvre, V. and Nardin, E., 2014. The role of palaeogeography in the Phanerozoic history of atmospheric CO2 and climate. Earth-Science Reviews, 128: 122-138.

Goddéris, Y., Le Hir, G., Macouin, M., Donnadieu, Y., Hubert-Théou, L., Dera, G., Aretz, M., Fluteau, F., Li, Z.X. and Halverson, G.P., 2017. Paleogeographic forcing of the strontium isotopic cycle in the Neoproterozoic. Gondwana Research, 42: 151-162.

Graham, J.B., Dudley, R., Aguilar, N.M. and Gans, C., 1995. Implications of the late Palaeozoic oxygen pulse for physiology and evolution. Nature, 375: 117-120.

Graham, J.B., Jew, C.J. and Wegner, N.C., 2016. Modeling Variable Phanerozoic Oxygen Effects on Physiology and Evolution. In: R.C. Roach, P.H. Hackett and P.D. Wagner (Editors), Hypoxia: Translation in Progress. Springer US, Boston, MA, pp. 409-426.

Guidry, M.W., Arvidson, R.S. and Mackenzie, F.T., 2007. Biological and Geochemical Forcings to Phanerozoic Change in Seawater, Atmosphere and Carbonate Precipitate Composition. In: P.G. Falkowski and A.H. Knoll (Editors), Evolution of Primary Producers in the Sea. Academic Press, pp. 377-403.

Halevy, I., Peters, S.E. and Fischer, W.W., 2012. Sulfate Burial Constraints on the Phanerozoic Sulfur Cycle. Science, 337(6092): 331-334.

Halverson, G.P., Dudás, F.Ö., Maloof, A.C. and Bowring, S.A., 2007. Evolution of the 87Sr/86Sr composition of Neoproterozoic seawater. Palaeogeography, Palaeoclimatology, Palaeoecology, 256(3): 103-129.

Haq, B.U., 2014. Cretaceous eustasy revisited. Global and Planetary Change, 113: 44-58.

Haq, B.U. and Al-Qahtani, A.M., 2005. Phanerozoic cycles of sea-level change on the Arabian Platform. Geoarabia, 10: 127-160.

Haq, B.U. and Schutter, S.R., 2008. A Chronology of Paleozoic Sea-Level Changes. Science, 322(5898): 64-68.

Hartmann, J., Jansen, N., Dürr, H.H., Kempe, S. and Köhler, P., 2009. Global CO2-consumption by chemical weathering: What is the contribution of highly active weathering regions? Global and Planetary Change, 69(4): 185-194.

Hartmann, J., Moosdorf, N., Lauerwald, R., Hinderer, M. and West, A.J., 2014. Global chemical weathering and associated P-release — The role of lithology, temperature and soil properties. Chemical Geology, 363: 145-163.

Hedges, J.I. and Keil, R.G., 1995. Sedimentary organic matter preservation: an assessment and speculative synthesis. Marine Chemistry, 49: 81-115.

Helly, J.J. and Levin, L.A., 2004. Global distribution of naturally occurring marine hypoxia on continental margins. Deep Sea Research Part I: Oceanographic Research Papers, 51(9): 1159-1168.

Holland, H.D., 1978. The Chemistry of the Atmosphere and Oceans. John Wiley.

Horita, J., Zimmermann, H. and Holland, H.D., 2002. Chemical evolution of seawater during the Phanerozoic: Implications from the record of marine evaporites. Geochimica et Cosmochimica Acta, 66(21): 3733-3756.

Horton, F., 2015. Did phosphorus derived from the weathering of large igneous provinces fertilize the Neoproterozoic ocean? Geochemistry, Geophysics, Geosystems, 16(6): 1723-1738.

IPCC (Editor), 2013. Climate Change 2013: The Physical Science Basis. Contribution of Working Group I to the Fifth Assessment Report of the Intergovernmental Panel on Climate Change. Cambridge University Press, Cambridge, United Kingdom and New York, NY, USA, 1535 pp.

Johnson, J.E., Gerpheide, A., Lamb, M.P. and Fischer, W.W., 2014. O2 constraints from Paleoproterozoic detrital pyrite and uraninite. Geological Society of America Bulletin, 126(5-6): 813-830.

Kampschulte, A. and Strauss, H., 2004. The sulfur isotopic evolution of Phanerozoic seawater based on the analysis of structurally substituted sulfate in carbonates. Chemical Geology, 204(3–4): 255-286.

Kennedy, K.L., Gibling, M.R., Eble, C.F., Gastaldo, R.A., Gensel, P.G., Werner-Zwanziger, U. and Wilson, R.A., 2013. Lower Devonian coaly shales of northern New Brunswick, Canada: plant accumulations in the early stages of Terrestrial colonization. Journal of Sedimentary Research, 83(12): 1202-1215.

Kolowith, L.C. and Berner, R.A., 2002. Weathering of phosphorus in black shales. Global Biogeochemical Cycles, 16(4): 1140.

Kump, L.R., 1988. Terrestrial feedback in atmospheric oxygen regulation by fire and phosphorus. Nature, 335: 152-154.

Kump, L.R. and Arthur, M.A., 1999. Interpreting carbon-isotope excursions: carbonates and organic matter. Chemical Geology, 161: 181-198.

Lasaga, A.C., 1989. A new approach to isotope modeling of the variation of atmospheric oxygen through the Phanerozoic. American Journal of Science, 289: 411-435.

Lee, C.-T.A., Shen, B., Slotnick, B.S., Liao, K., Dickens, G.R., Yokoyama, Y., Lenardic, A., Dasgupta, R., Jellinek, M., Lackey, J.S., Schneider, T. and Tice, M.M., 2013. Continental arc–island arc fluctuations, growth of crustal carbonates, and long-term climate change. Geosphere, 9(1): 21-36.

Lenton, T.M., 2013. Fire Feedbacks on Atmospheric Oxygen. In: C.M. Belcher (Editor), Fire Phenomena and the Earth System: An Interdisciplinary Guide to Fire Science. Wiley-Blackwell, pp. 289-308.

Lenton, T.M., Boyle, R.A., Poulton, S.W., Shields, G.A. and Butterfield, N.J., 2014. Co-evolution of eukaryotes and ocean oxygenation in the Neoproterozoic era. Nature Geoscience, 7(4): 257-265.

Lenton, T.M., Crouch, M., Johnson, M., Pires, N. and Dolan, L., 2012. First plants cooled the Ordovician. Nature Geoscience, 5(2): 86-89.

Lenton, T.M., Dahl, T.W., Daines, S.J., Mills, B.J.W., Ozaki, K., Saltzman, M.R. and Porada, P., 2016. Earliest land plants created modern levels of atmospheric oxygen. Proceedings of the National Academy of Sciences, 113(35): 9704-9709.

Lenton, T.M. and Daines, S.J., 2017. Biogeochemical Transformations in the History of the Ocean. Annual Review of Marine Science, 9(1): 31-58.

Lenton, T.M. and Watson, A.J., 2000a. Redfield revisited: 1. Regulation of nitrate, phosphate and oxygen in the ocean. Global Biogeochemical Cycles, 14(1): 225-248.

Lenton, T.M. and Watson, A.J., 2000b. Redfield revisited: 2. What regulates the oxygen content of the atmosphere? Global Biogeochemical Cycles, 14(1): 249-268.

Lenton, T.M. and Watson, A.J., 2011. Revolutions that made the Earth. Oxford University Press, Oxford.

Li, G. and Elderfield, H., 2013. Evolution of carbon cycle over the past 100 million years. Geochimica et Cosmochimica Acta, 103(0): 11-25.

Lowenstein, T.K., Timofeeff, M.N., Kovalevych, V.M. and Horita, J., 2005. The major-ion composition of Permian seawater. Geochimica et Cosmochimica Acta, 69(7): 1701-1719.

Matthews, K.J., Maloney, K.T., Zahirovic, S., Williams, S.E., Seton, M. and Müller, R.D., 2016. Global plate boundary evolution and kinematics since the late Paleozoic. Global and Planetary Change, 146: 226-250.

McArthur, J.M., Howarth, R.J. and Shields, G.A., 2012. Chapter 7 - Strontium Isotope Stratigraphy, The Geologic Time Scale. Elsevier, Boston, pp. 127-144.

McKenzie, N.R., Horton, B.K., Loomis, S.E., Stockli, D.F., Planavsky, N.J. and Lee, C.-T.A., 2016. Continental arc volcanism as the principal driver of icehouse-greenhouse variability. Science, 352(6284): 444-447.

Mills, B., Daines, S.J. and Lenton, T.M., 2014a. Changing tectonic controls on the long-term carbon cycle from Mesozoic to present. Geochem. Geophys. Geosyst., 15: 4866-4884.

Mills, B., Lenton, T.M. and Watson, A.J., 2014b. Proterozoic oxygen rise linked to shifting balance between seafloor and terrestrial weathering. PNAS, 111(25): 9073-9078.

Mills, B., Watson, A.J., Goldblatt, C., Boyle, R. and Lenton, T.M., 2011. Timing of Neoproterozoic glaciations linked to transport-limited global weathering. Nature Geoscience, 4: 861-864.

Mills, B.J.W., Belcher, C.M., Lenton, T.M. and Newton, R.J., 2016. A modeling case for high atmospheric oxygen concentrations during the Mesozoic and Cenozoic. Geology, 44(12): 1023-1026.

Mills, B.J.W., Scotese, C.R., Walding, N.G., Shields-Zhou, G.A. and Lenton, T.M., 2017. Elevated CO_2 degassing rates prevented the return of Snowball Earth during the Phanerozoic. Nature Communications, 8: 1110.

Monteiro, F.M., Pancost, R.D., Ridgwell, A. and Donnadieu, Y., 2012. Nutrients as the dominant control on the spread of anoxia and euxinia across the Cenomanian-Turonian oceanic anoxic event (OAE2): Model-data comparison. Paleoceanography, 27(4): PA4209.

Moon, S., Chamberlain, C.P. and Hilley, G.E., 2014. New estimates of silicate weathering rates and their uncertainties in global rivers. Geochimica et Cosmochimica Acta, 134: 257-274.

Moulton, K.L., West, J. and Berner, R.A., 2000. Solute flux and mineral mass balance approaches to the quantification of plant effects on silicate weathering. American Journal of Science, 300(7): 539-570.

Munhoven, G., 2002. Glacial–interglacial changes of continental weathering: estimates of the related CO2 and HCO3− flux variations and their uncertainties. Global and Planetary Change, 33(1–2): 155-176.

Nelsen, M.P., DiMichele, W.A., Peters, S.E. and Boyce, C.K., 2016. Delayed fungal evolution did not cause the Paleozoic peak in coal production. Proceedings of the National Academy of Sciences, 113(9): 2442-2447.

Ozaki, K. and Tajika, E., 2013. Biogeochemical effects of atmospheric oxygen concentration, phosphorus weathering, and sea-level stand on oceanic redox chemistry: Implications for greenhouse climates. Earth and Planetary Science Letters, 373: 129-139.

Ozaki, K., Tajima, S. and Tajika, E., 2011. Conditions required for oceanic anoxia/euxinia: Constraints from a one-dimensional ocean biogeochemical cycle model. Earth and Planetary Science Letters, 304(1-2): 270-279.

Paytan, A., Kastner, M., Campbell, D. and Thiemens, M.H., 1998. Sulfur Isotopic Composition of Cenozoic Seawater Sulfate. Science, 282(5393): 1459-1462.

Planavsky, N.J., Rouxel, O.J., Bekker, A., Lalonde, S.V., Konhauser, K.O., Reinhard, C.T. and Lyons, T.W., 2010. The evolution of the marine phosphate reservoir. Nature, 467(7319): 1088-1090.

Pohl, A., Donnadieu, Y., Le Hir, G., Buoncristiani, J.F. and Vennin, E., 2014. Effect of the Ordovician paleogeography on the (in)stability of the climate. Clim. Past, 10(6): 2053-2066.

Pohl, A., Donnadieu, Y., Le Hir, G., Ladant, J.-B., Dumas, C., Alvarez-Solas, J. and Vandenbroucke, T.R.A., 2016. Glacial onset predated Late Ordovician climate cooling. Paleoceanography, 31(6): 800-821.

Porada, P., Lenton, T.M., Pohl, A., Weber, B., Mander, L., Donnadieu, Y., Beer, C., Poschl, U. and Kleidon, A., 2016. High potential for weathering and climate effects of non-vascular vegetation in the Late Ordovician. Nature Communications, 7: 12113.

Quirk, J., Leake, J.R., Johnson, D.A., Taylor, L.L., Saccone, L. and Beerling, D.J., 2015. Constraining the role of early land plants in Palaeozoic weathering and global cooling. Proceedings of the Royal Society of London B: Biological Sciences, 282(1813).

Regnier, P., Friedlingstein, P., Ciais, P., Mackenzie, F.T., Gruber, N., Janssens, I.A., Laruelle, G.G., Lauerwald, R., Luyssaert, S., Andersson, A.J., Arndt, S., Arnosti, C., Borges, A.V., Dale, A.W., Gallego-Sala, A., Goddéris, Y., Goossens, N., Hartmann, J., Heinze, C., Ilyina, T., Joos, F., LaRowe, D.E., Leifeld, J., Meysman, F.J.R., Munhoven, G., Raymond, P.A., Spahni, R.,

Suntharalingam, P. and Thullner, M., 2013. Anthropogenic perturbation of the carbon fluxes from land to ocean. Nature Geosci, 6(8): 597-607.

Ronov, A.B., 1993. Stratisfera-Ili Osadochnaya Obolochka Zemli (Kolichestvennoe Issledovanie). Nauka, Moskva.

Royer, D.L., 2014. Atmospheric CO2 and O2 During the Phanerozoic: Tools, Patterns, and Impacts. In: H.D. Holland and K.K. Turekian (Editors), Treatise on Geochemistry (Second Edition). Elsevier, Oxford, pp. 251-267.

Royer, D.L., Berner, R.A. and Park, J., 2007. Climate sensitivity constrained by CO2 concentrations over the past 420[thinsp]million years. Nature, 446(7135): 530-532.

Royer, D.L., Donnadieu, Y., Park, J., Kowalczyk, J. and Goddéris, Y., 2014. Error analysis of CO2 and O2 estimates from the long-term geochemical model GEOCARBSULF. American Journal of Science, 314(9): 1259-1283.

Saltzman, M.R. and Thomas, E., 2012. Chapter 11 - Carbon Isotope Stratigraphy. In: F.M. Gradstein, J.G.O.D. Schmitz and G.M. Ogg (Editors), The Geologic Time Scale. Elsevier, Boston, pp. 207-232.

Schaller, M.F., Wright, J.D. and Kent, D.V., 2011. Atmospheric Pco2 Perturbations Associated with the Central Atlantic Magmatic Province. Science, 331(6023): 1404-1409.

Scott, A.C. and Glaspool, I.J., 2006. The diversification of Paleozoic fire systems and fluctuations in atmospheric oxygen concentration. Proceedings of the National Academy of Sciences of the United States of America, 103(29): 10861-10865.

Shampine, L.F. and Reichelt, M.W., 1997. The MATLAB ODE Suite. SIAM Journal on Scientific Computing, 18(1): 1-22.

Sleep, N.H., 2005. Dioxygen over geological time. In: A. Sigel, H. Sigel and R.K.O. Sigel (Editors), Metal Ions in Biological Systems, Volume 43 - Biogeochemical Cycles of Elements. Taylor & Francis, Boca Raton, FL, pp. 49-73.

Slomp, C.P. and Van Cappellen, P., 2007. The global marine phosphorus cycle: sensitivity to oceanic circulation. Biogeosciences, 4(2): 155-171.

Sperling, E.A., Knoll, A.H. and Girguis, P.R., 2015a. The Ecological Physiology of Earth's Second Oxygen Revolution. Annual Review of Earth and Planetary Sciences, 46: 215-235.

Sperling, E.A., Wolock, C.J., Morgan, A.S., Gill, B.C., Kunzmann, M., Halverson, G.P., Macdonald, F.A., Knoll, A.H. and Johnston, D.T., 2015b. Statistical analysis of iron geochemical data suggests limited late Proterozoic oxygenation. Nature, 523(7561): 451-454.

Staudigel, H., Hart, S.R., Schmincke, H.-U. and Smith, B.M., 1989. Cretaceous ocean crust at DSDP Sites 417 and 418: Carbon uptake from weathering versus loss by magmatic outgassing. Geochimica et Cosmochimica Acta, 53(11): 3091-3094.

Torres, M.A., West, A.J. and Li, G., 2014. Sulphide oxidation and carbonate dissolution as a source of CO2 over geological timescales. Nature, 507(7492): 346-349.

Tostevin, R., Turchyn, A.V., Farquhar, J., Johnston, D.T., Eldridge, D.L., Bishop, J.K.B. and McIlvin, M., 2014. Multiple sulfur isotope constraints on the modern sulfur cycle. Earth and Planetary Science Letters, 396: 14-21.

Van Cappellen, P. and Ingall, E.D., 1994. Benthic phosphorus regeneration, net primary production, and ocean anoxia: A model of the coupled marine biogeochemical cycles of carbon and phosphorus. Paleoceanography, 9: 677-692.

Van Cappellen, P. and Ingall, E.D., 1996. Redox stabilisation of the Atmosphere and Oceans by Phosphorus-Limited Marine Productivity. Science, 271: 493-496.

Van Der Meer, D.G., Zeebe, R.E., van Hinsbergen, D.J.J., Sluijs, A., Spakman, W. and Torsvik, T.H., 2014. Plate tectonic controls on atmospheric CO2 levels since the Triassic. Proceedings of the National Academy of Sciences, 111(12): 4380-4385.

Veizer, J. and Mackenzie, F.T., 2003. Evolution of Sedimentary Rocks, Treatise on Geochemistry: Sediments, Diagenesis and Sedimentary Rocks. Elsevier, pp. 369-407.

Vollstaedt, H., Eisenhauer, A., Wallmann, K., Böhm, F., Fietzke, J., Liebetrau, V., Krabbenhöft, A., Farkaš, J., Tomašových, A., Raddatz, J. and Veizer, J., 2014. The Phanerozoic δ88/86Sr record of seawater: New constraints on past changes in oceanic carbonate fluxes. Geochimica et Cosmochimica Acta, 128: 249-265.

Walker, J.C.G., Hays, P.B. and Kasting, J.F., 1981. A negative feedback mechanism for the long-term stabilisation of Earth's surface temperature. Journal of Geophysical Research, 86(C10): 9776-9782.

Willenbring, J.K. and von Blanckenburg, F., 2010. Long-term stability of global erosion rates and weathering during late-Cenozoic cooling. Nature, 465(7295): 211-214.

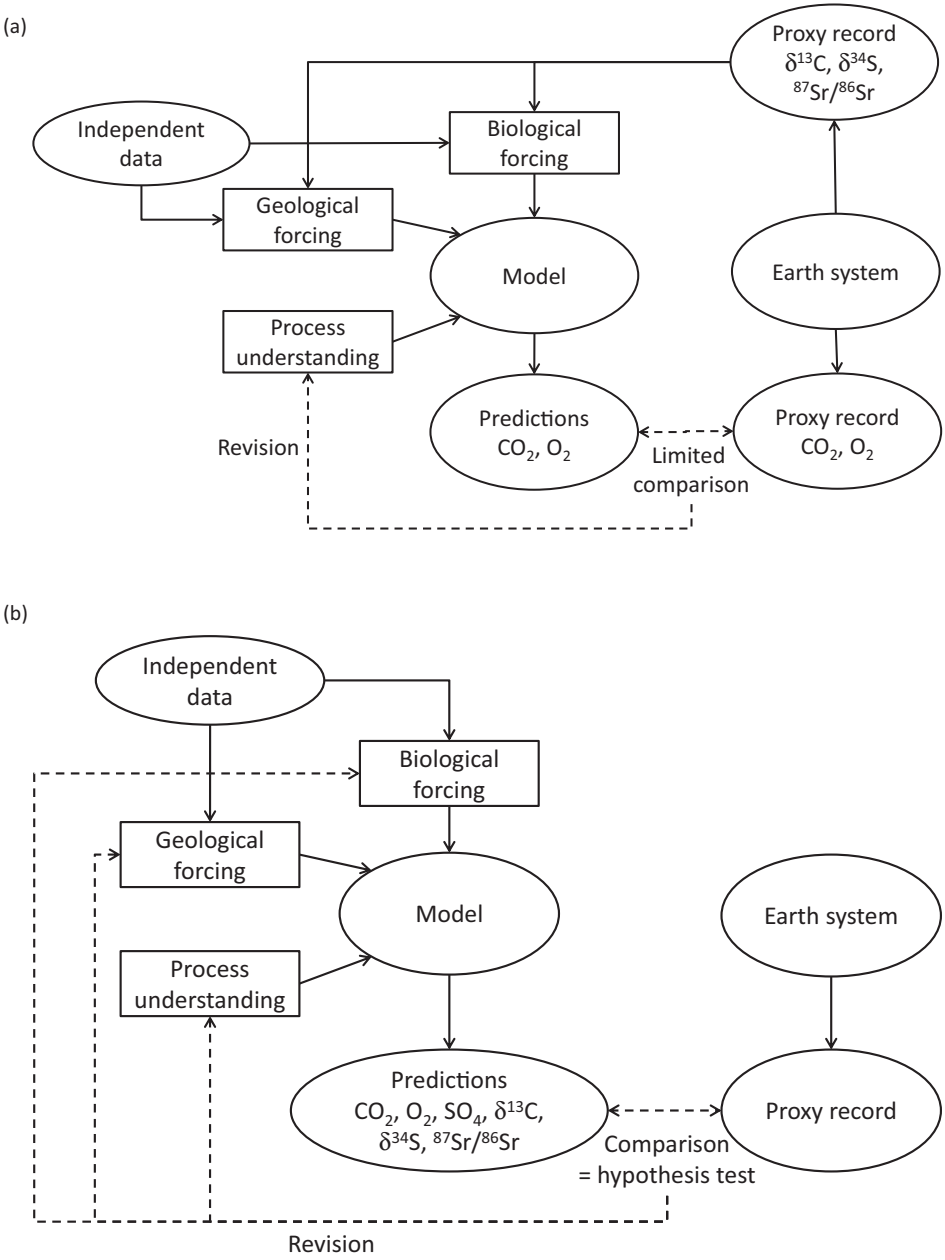
(a)
Proxy record
δ13C, δ34S,
87Sr/86Sr
Independent data
Biological forcing
Geological forcing
Model
Earth system
Process understanding
Predictions
CO2, O2
Proxy record
CO2, O2
Revision
Limited comparison
(b)
Independent data
Biological forcing
Geological forcing
Model
Earth system
Process understanding
Predictions
CO2, O2, SO4, δ13C,
δ34S, 87Sr/86Sr
Proxy record
Comparison
= hypothesis test
Revision

Figure 1

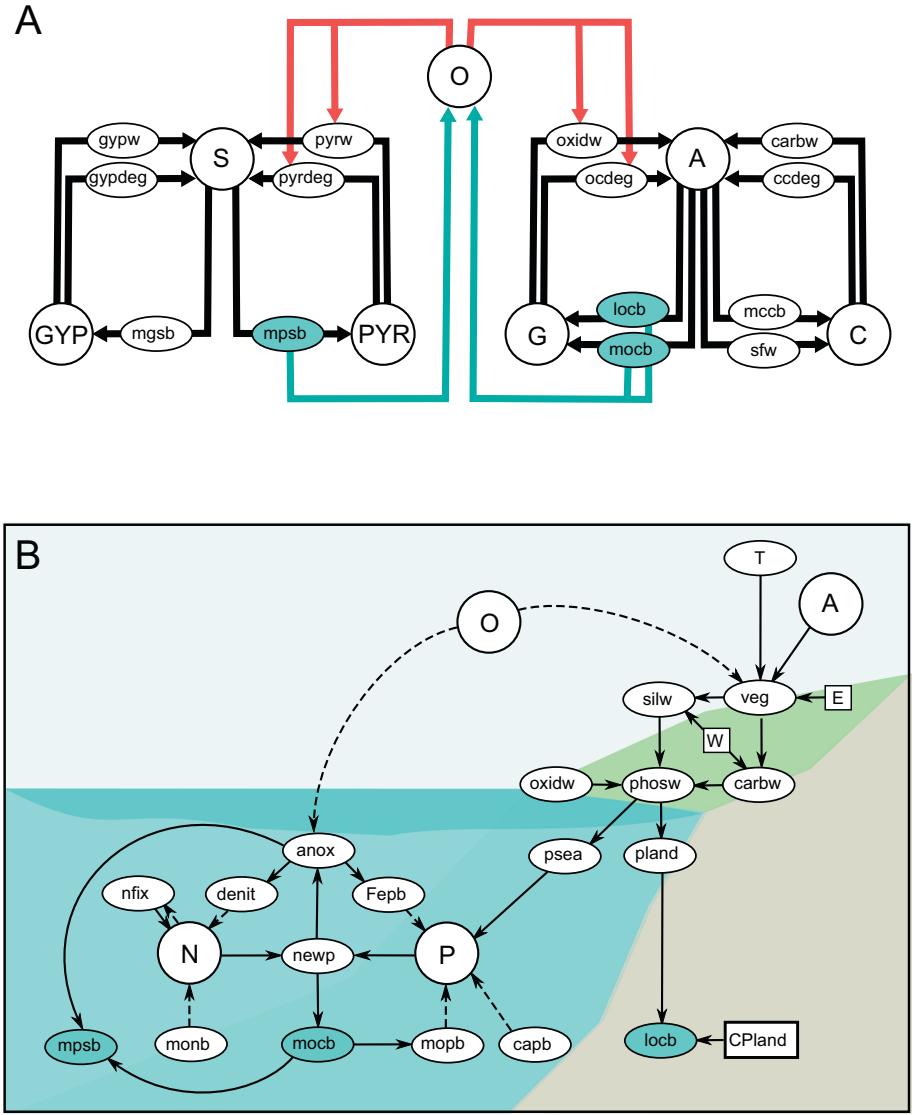
A
O
S
gypw
gypdeg
pyrw
pyrdeg
GYP
mgsb
mpsb
PYR
A
oxidw
ocdeg
carbw
ccdeg
G
locb
mocb
mccb
sfw
C
B
T
A
O
silw
veg
E
W
oxidw
phosw
carbw
anox
psea
pland
nfix
denit
Fepb
N
newp
P
mpsb
monb
mocb
mopb
capb
locb
CPland

Figure 2

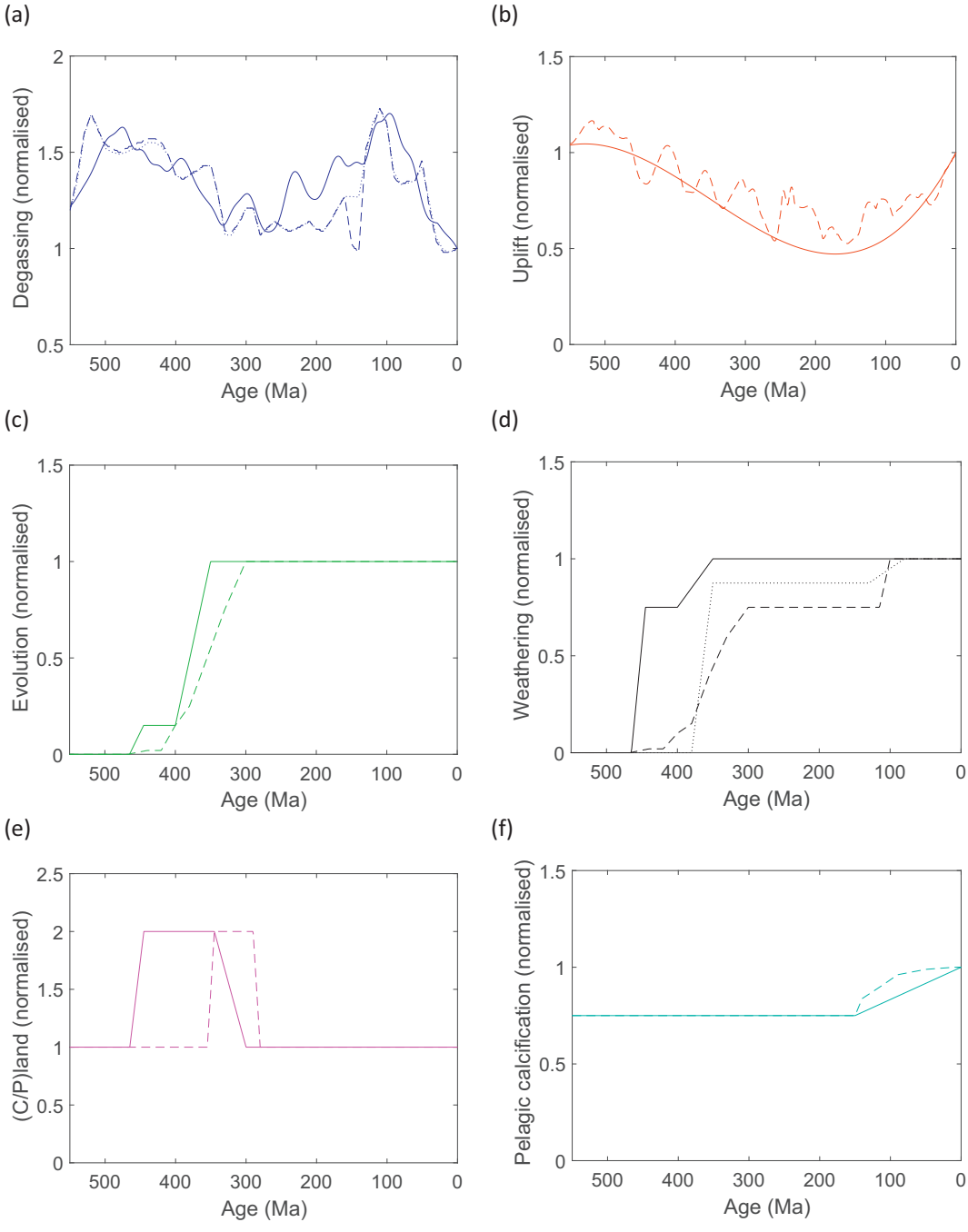
(a)
Degassing (normalised)
2
1.5
1
0.5
500
400
300
200
100
0
Age (Ma)
(b)
Uplift (normalised)
1.5
1
0.5
0
500
400
300
200
100
0
Age (Ma)
(c)
Evolution (normalised)
1.5
1
0.5
0
500
400
300
200
100
0
Age (Ma)
(d)
Weathering (normalised)
1.5
1
0.5
0
500
400
300
200
100
0
Age (Ma)
(e)
(C/P)land (normalised)
2.5
2
1.5
1
0.5
0
500
400
300
200
100
0
Age (Ma)
(f)
Pelagic calcification (normalised)
1.5
1
0.5
0
500
400
300
200
100
0
Age (Ma)

Figure 3

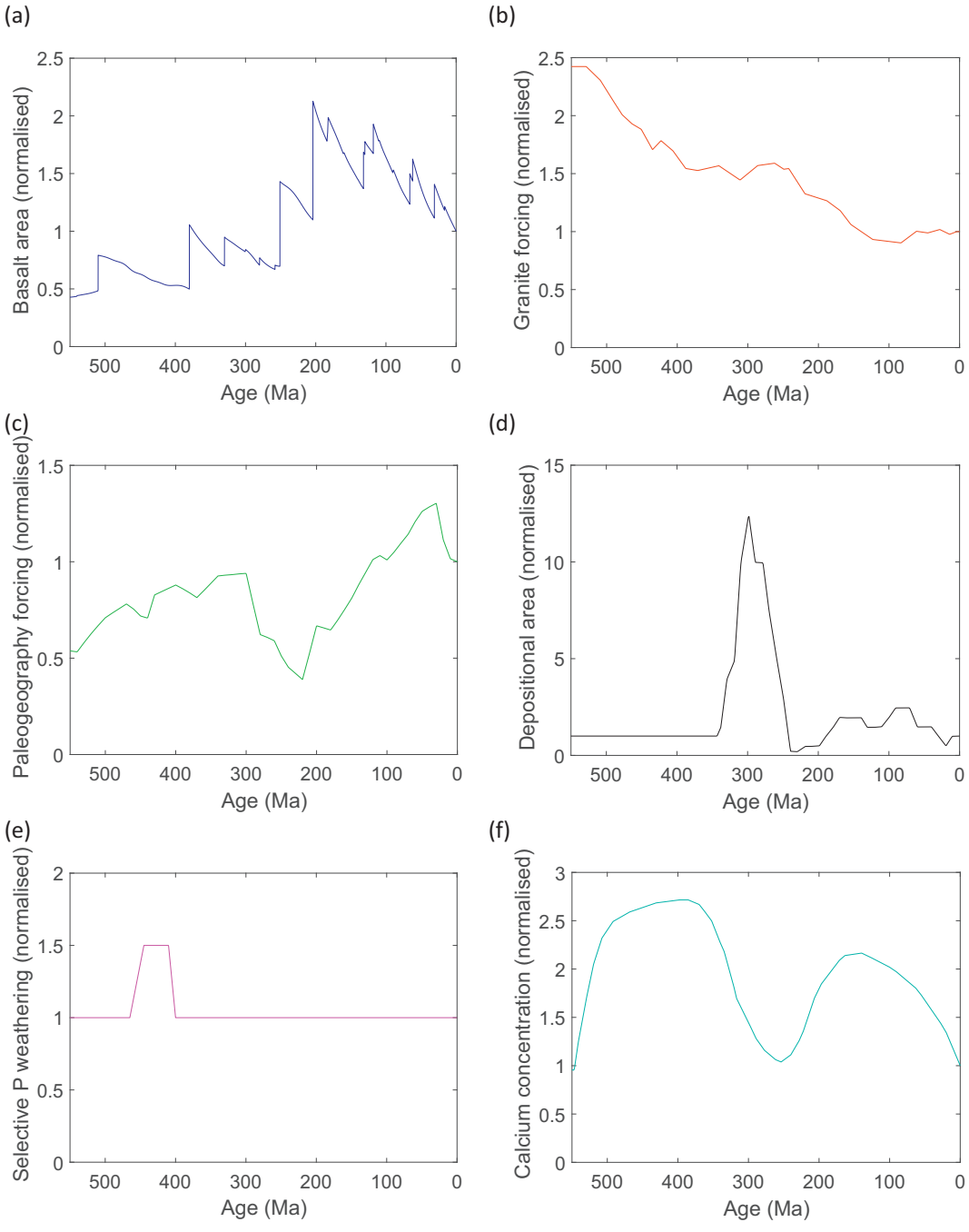
(a)
Basalt area (normalised)
Age (Ma)
(b)
Granite forcing (normalised)
Age (Ma)
(c)
Paleogeography forcing (normalised)
Age (Ma)
(d)
Depositional area (normalised)
Age (Ma)
(e)
Selective P weathering (normalised)
Age (Ma)
(f)
Calcium concentration (normalised)
Age (Ma)

Figure 4

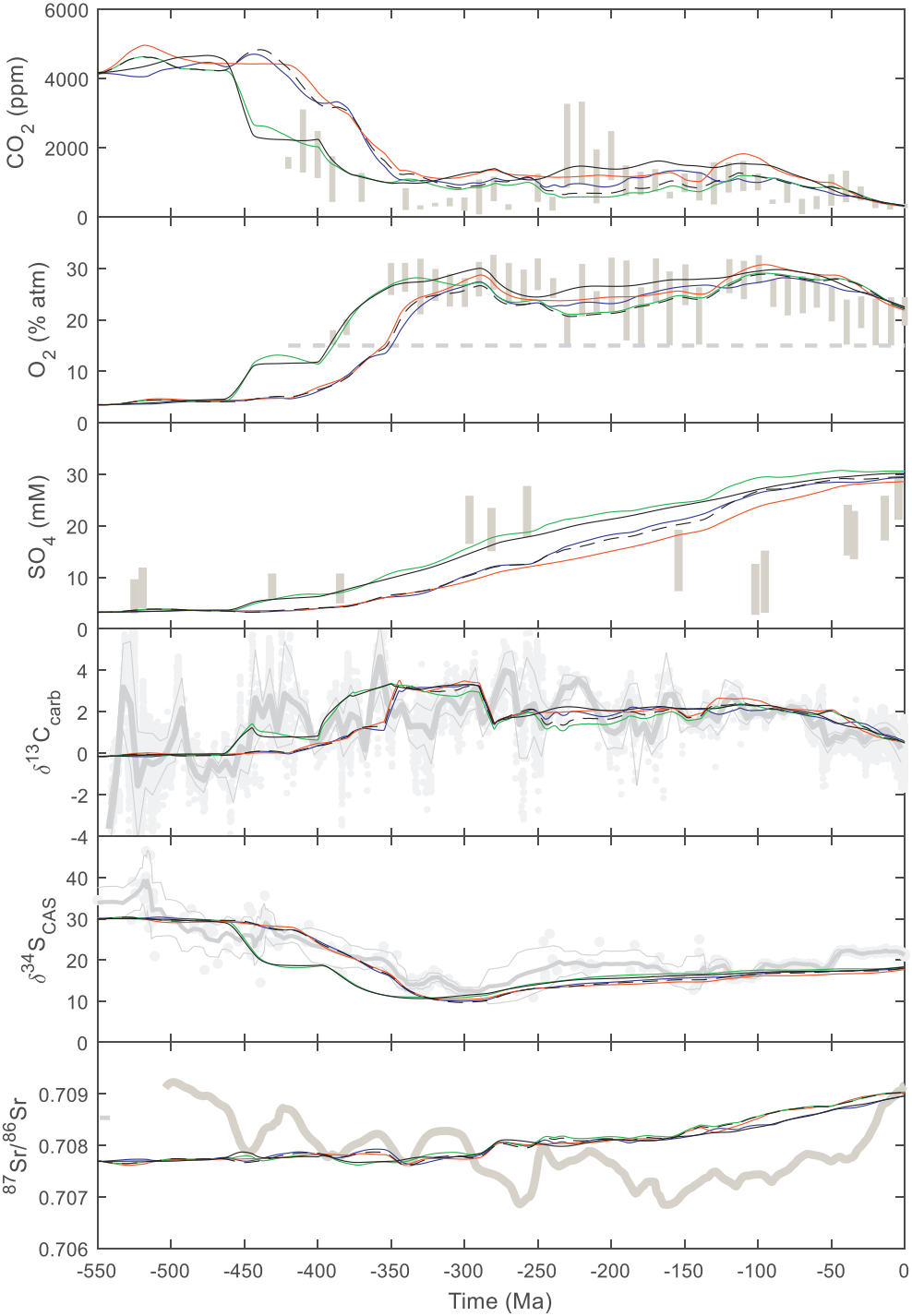
CO2 (ppm)
6000
4000
2000
0
O2 (% atm)
30
20
10
0
SO4 (mM)
30
20
10
0
δ13Ccarb
4
2
0
-2
-4
δ34SCAS
40
30
20
10
0
87Sr/86Sr
0.709
0.708
0.707
0.706
-550
-500
-450
-400
-350
-300
-250
-200
-150
-100
-50
0
Time (Ma)

Figure 5

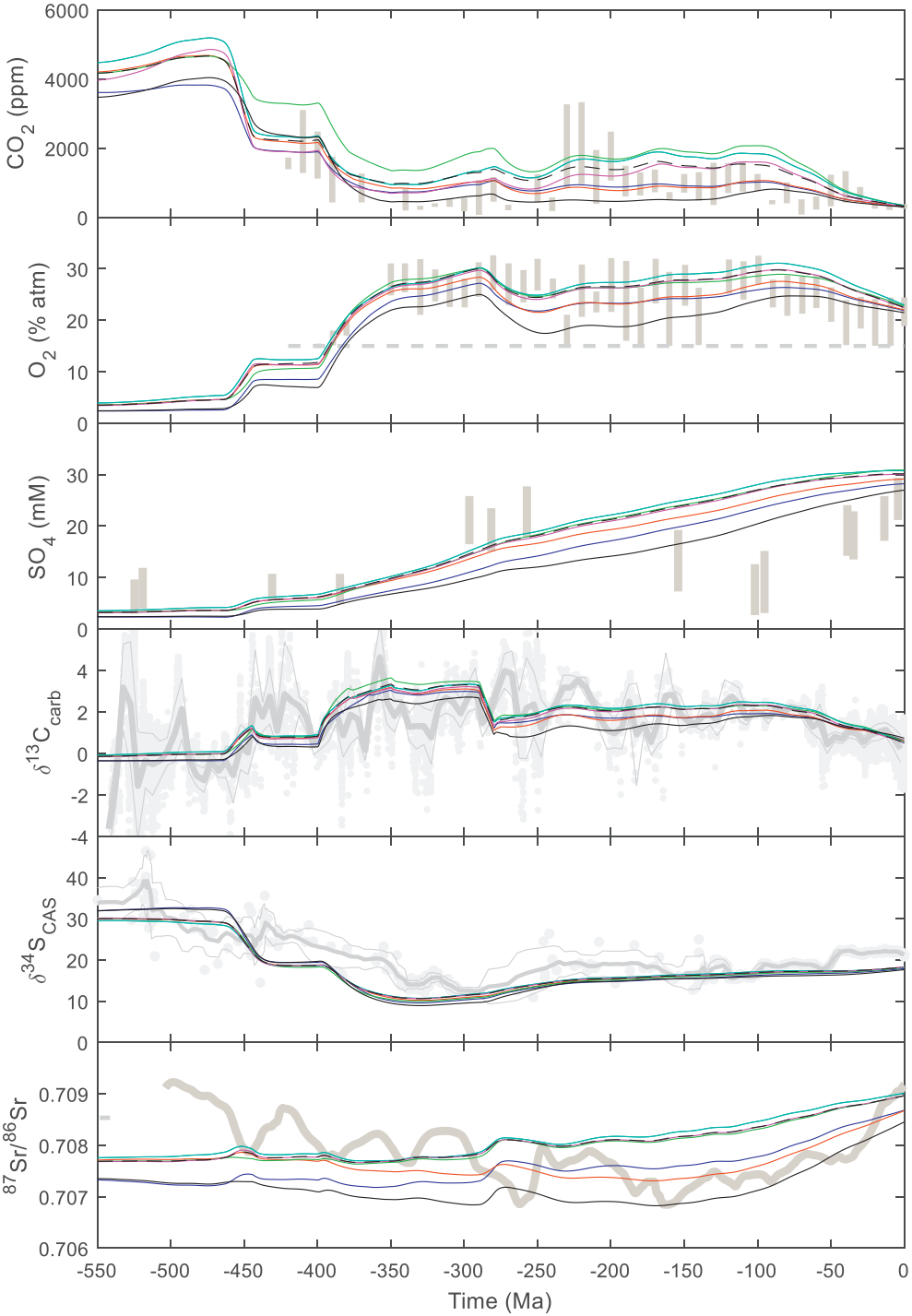
CO2 (ppm)
6000
4000
2000
0
O2 (% atm)
30
20
10
0
SO4 (mM)
30
20
10
0
δ13Ccarb
4
2
0
-2
-4
δ34SCAS
40
30
20
10
0
87Sr/86Sr
0.709
0.708
0.707
0.706
-550
-500
-450
-400
-350
-300
-250
-200
-150
-100
-50
0
Time (Ma)

Figure 6

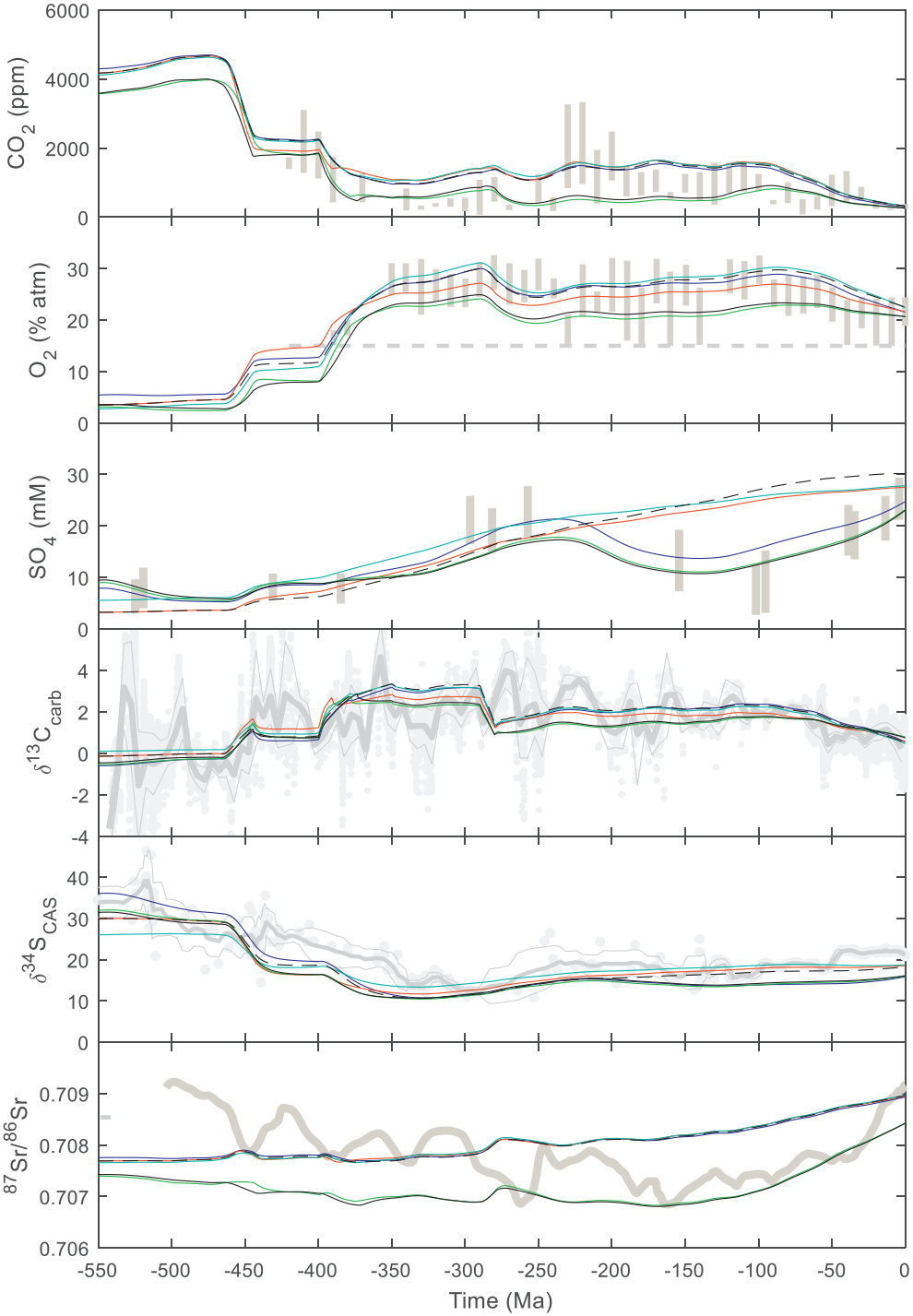
CO2 (ppm)
6000
4000
2000
0
O2 (% atm)
30
20
10
0
SO4 (mM)
30
20
10
0
δ13Ccarb
4
2
0
-2
-4
δ34SCAS
40
30
20
10
0
87Sr/86Sr
0.709
0.708
0.707
0.706
-550
-500
-450
-400
-350
-300
-250
-200
-150
-100
-50
0
Time (Ma)

Figure 7

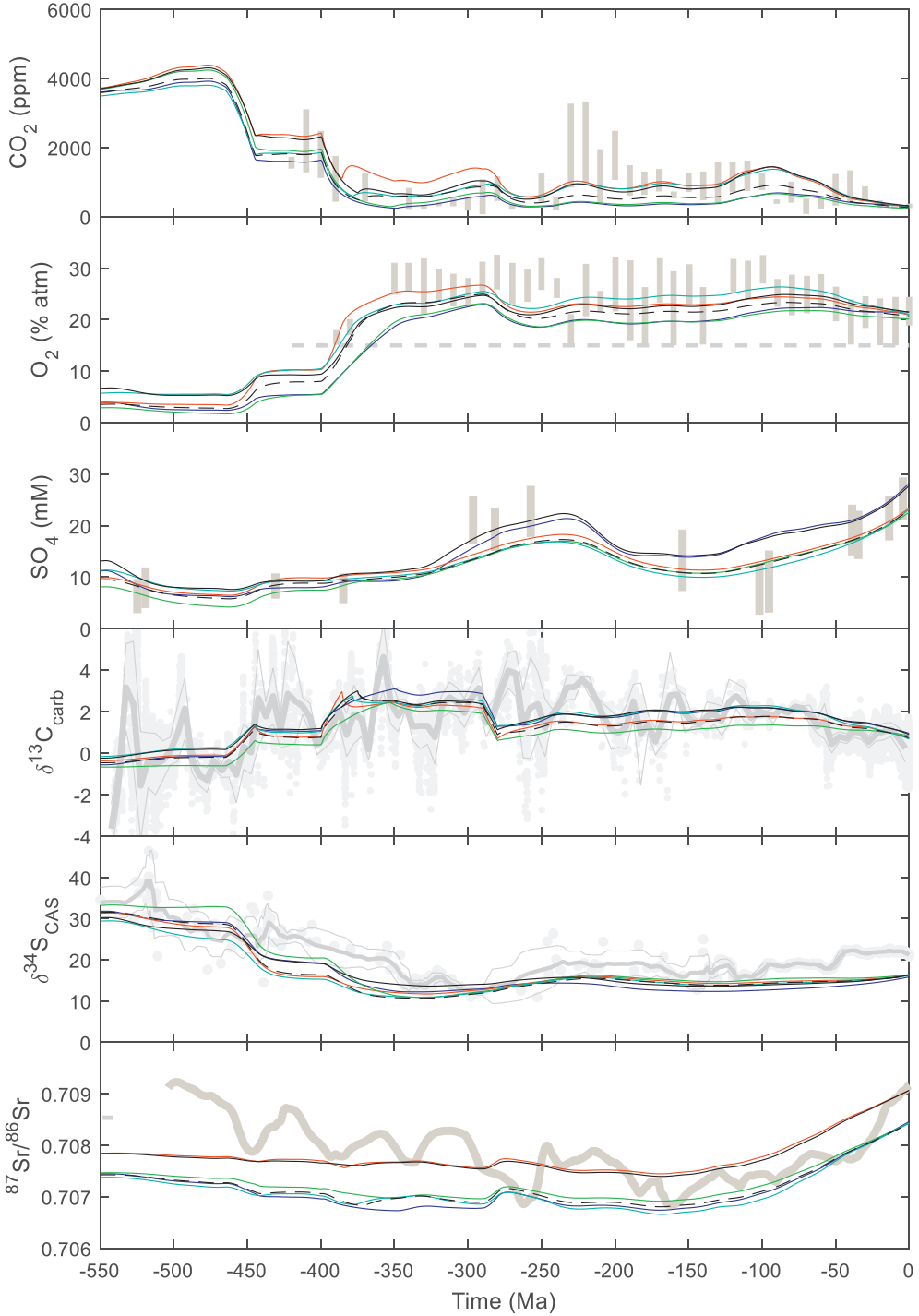
CO2 (ppm)
6000
4000
2000
0
O2 (% atm)
30
20
10
0
SO4 (mM)
30
20
10
0
δ13Ccarb
4
2
0
-2
-4
δ34SCAS
40
30
20
10
0
87Sr/86Sr
0.709
0.708
0.707
0.706
-550
-500
-450
-400
-350
-300
-250
-200
-150
-100
-50
0
Time (Ma)

Figure 8

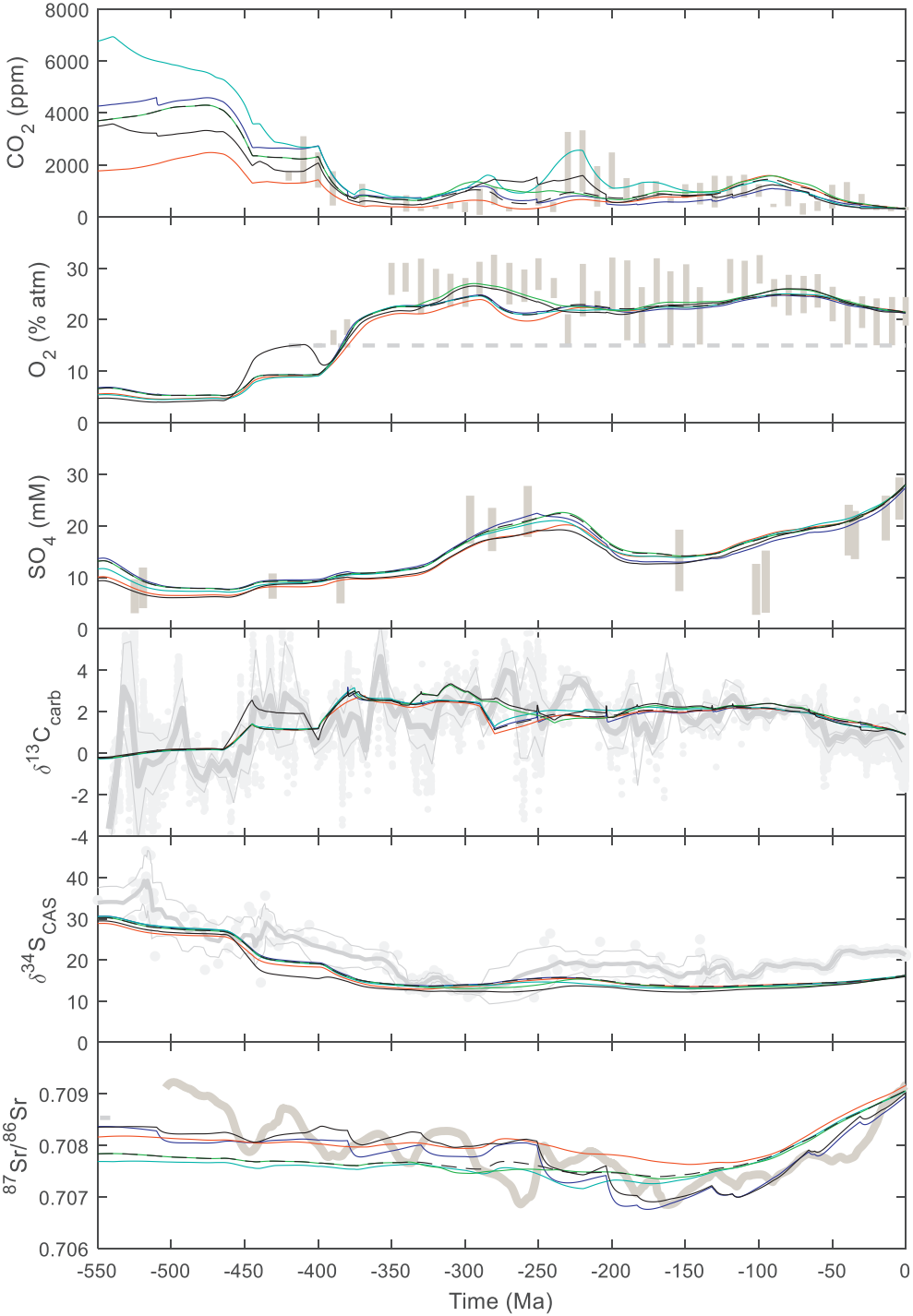
CO2 (ppm)
8000
6000
4000
2000
0
O2 (% atm)
30
20
10
0
SO4 (mM)
30
20
10
0
δ13Ccarb
4
2
0
-2
-4
δ34SCAS
40
30
20
10
0
87Sr/86Sr
0.709
0.708
0.707
0.706
-550
-500
-450
-400
-350
-300
-250
-200
-150
-100
-50
0
Time (Ma)

Figure 9

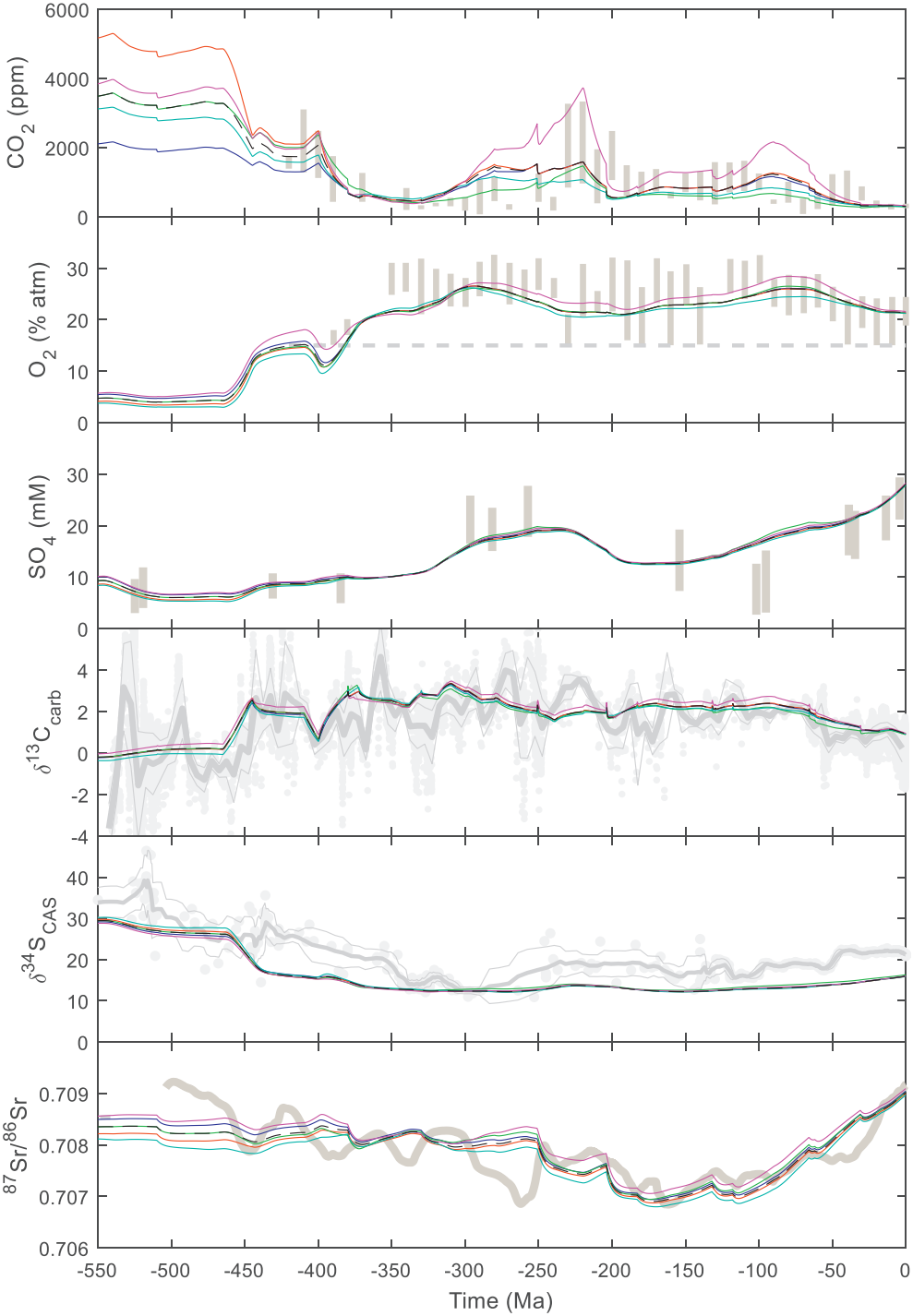
CO2 (ppm)
6000
4000
2000
0
O2 (% atm)
30
20
10
0
SO4 (mM)
30
20
10
0
δ13Ccarb
4
2
0
-2
-4
δ34SCAS
40
30
20
10
0
87Sr/86Sr
0.709
0.708
0.707
0.706
-550
-500
-450
-400
-350
-300
-250
-200
-150
-100
-50
0
Time (Ma)

Figure 10

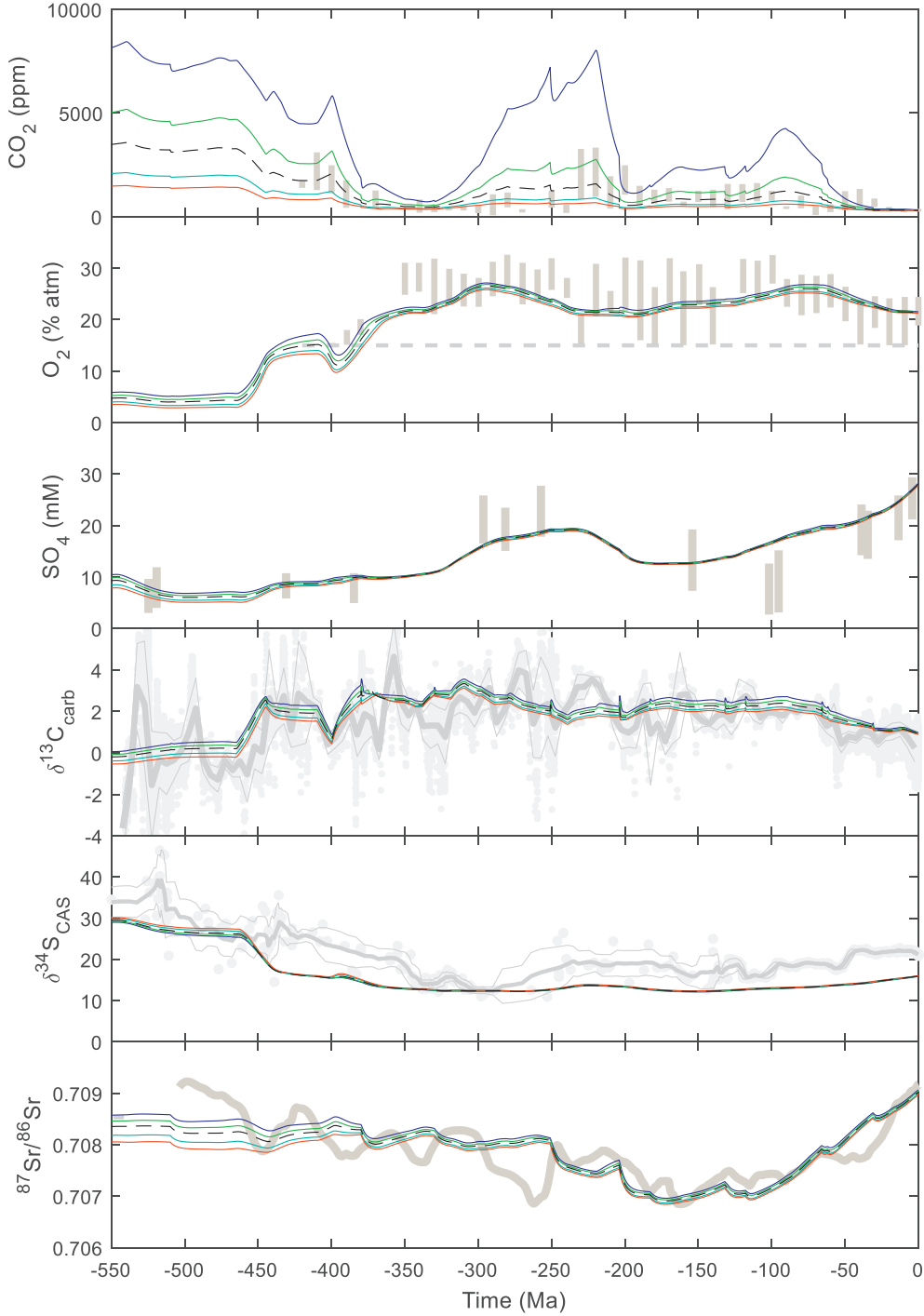
CO2 (ppm)
10000
5000
0
O2 (% atm)
30
20
10
0
SO4 (mM)
30
20
10
0
δ13Ccarb
4
2
0
-2
-4
δ34SCAS
40
30
20
10
0
87Sr/86Sr
0.709
0.708
0.707
0.706
-550
-500
-450
-400
-350
-300
-250
-200
-150
-100
-50
0
Time (Ma)

Figure 11

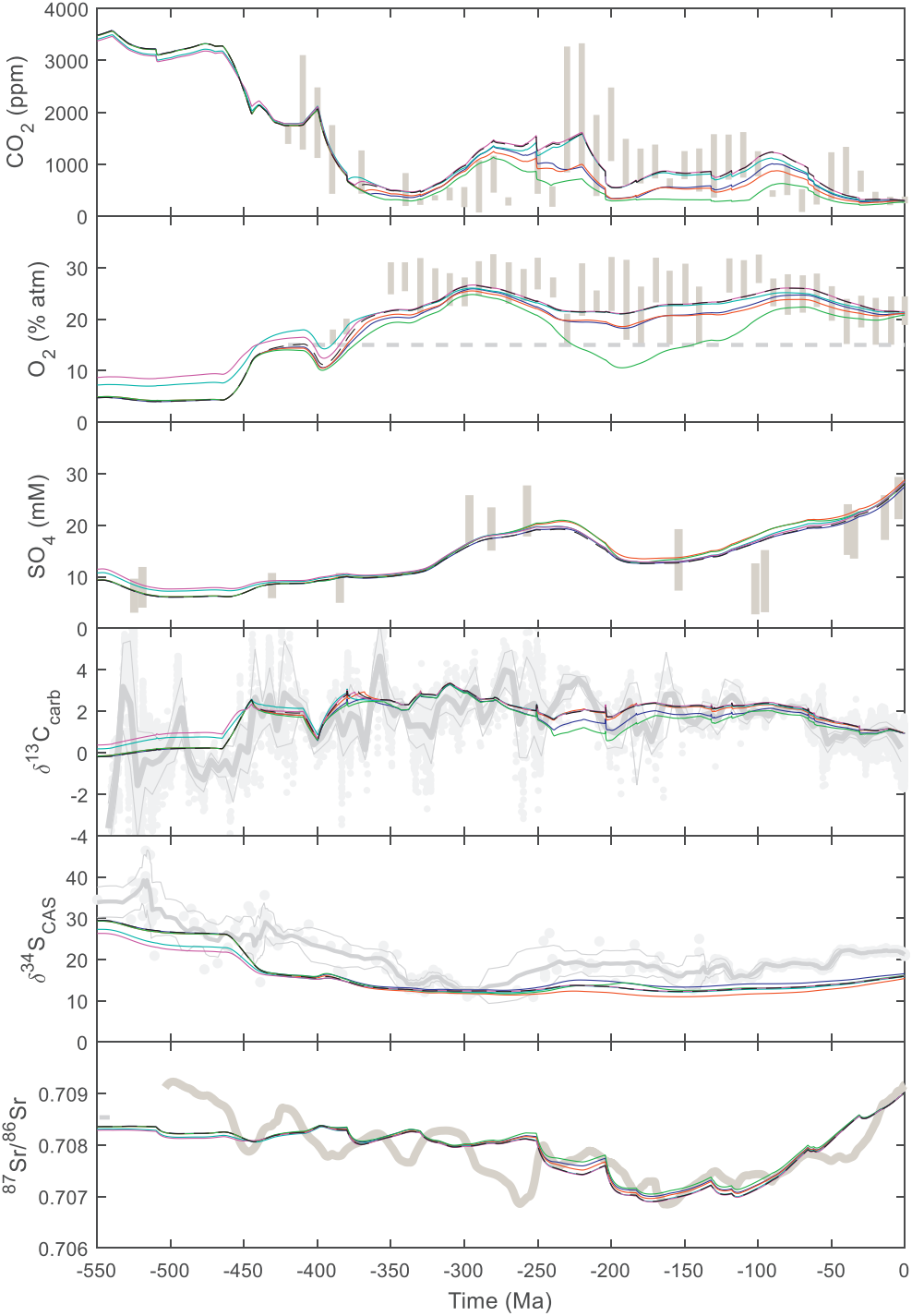
CO2 (ppm)
4000
3000
2000
1000
0
O2 (% atm)
30
20
10
0
SO4 (mM)
30
20
10
0
δ13Ccarb
4
2
0
-2
-4
δ34SCAS
40
30
20
10
0
87Sr/86Sr
0.709
0.708
0.707
0.706
-550
-500
-450
-400
-350
-300
-250
-200
-150
-100
-50
0
Time (Ma)

Figure 12

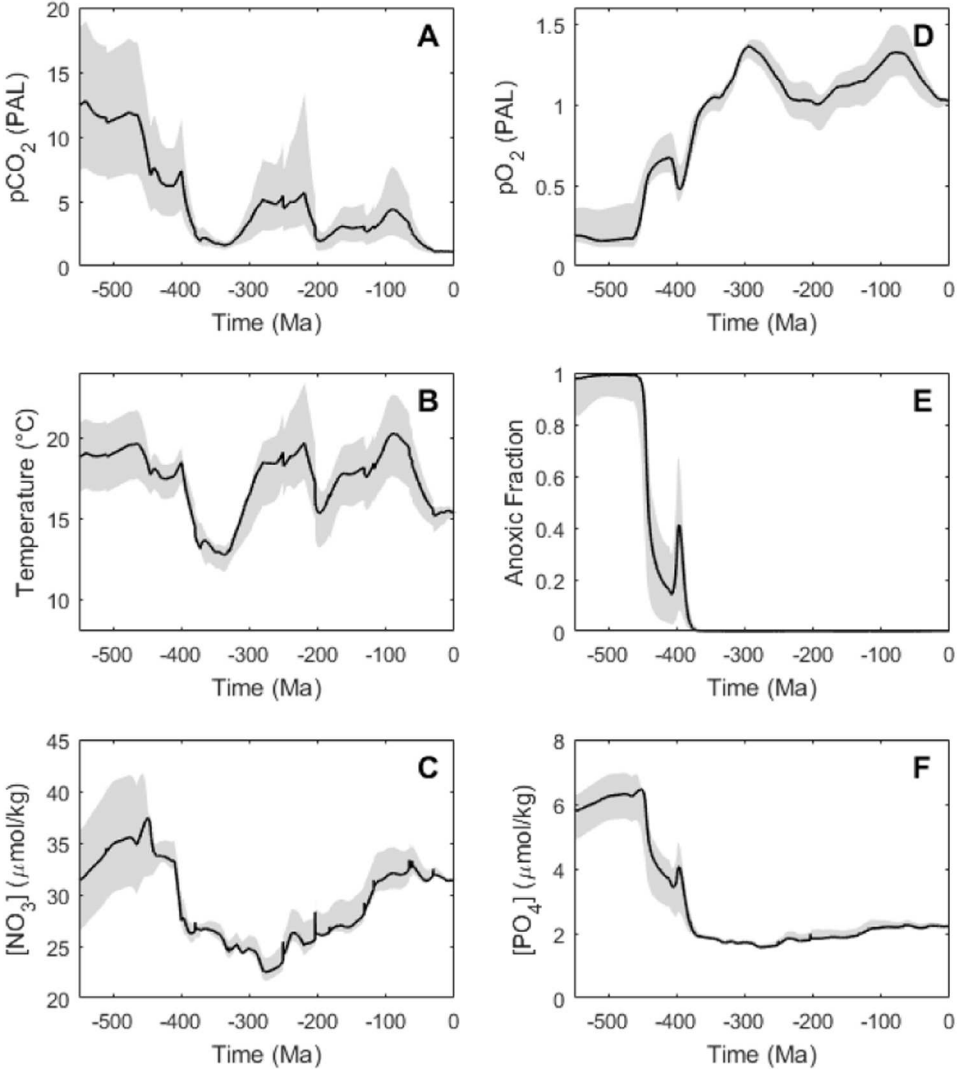
A
pCO2 (PAL)
Time (Ma)
D
pO2 (PAL)
Time (Ma)
B
Temperature (°C)
Time (Ma)
E
Anoxic Fraction
Time (Ma)
C
[NO3] (μmol/kg)
Time (Ma)
F
[PO4] (μmol/kg)
Time (Ma)

Figure 13